

School of Science and Engineering
Department of Imaging & Applied Physics
Curtin Institute of Radio Astronomy
International Centre for Radio Astronomy Research

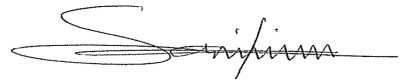
Studies of the Crab Giant Pulses with the Murchison
Widefield Array

Samuel Iyen Jeffrey Oronsaye

This thesis is presented for the Degree of
Master of Philosophy
of
Curtin University

July 2016

To the best of my knowledge and belief this thesis contains no material previously published by any other person except where due acknowledgement has been made. This thesis contains no material which has been accepted for the award of any other degree or diploma in any university.

A handwritten signature in black ink, appearing to read 'S. Oronsaye', with a horizontal line extending to the right.

.....
Samuel I. J. Oronsaye

12 July 2016

*“So then it is not of him that willeth,
nor of him that runneth,
but of God that showeth mercy”*

Romans 9:16

Acknowledgements

I am grateful to God for granting me admission into this noble University. I would like to thank my supervisors Professor Steven Tingay, Drs. Stephen Ord, Ramesh Bhat and Steven Tremblay for their guidance, valuable ideas and contributions towards the completion of this thesis; and for granting me the opportunity to work with them at Curtin University and ICRAR. I am grateful to Curtin University for continuous and consistent funding through Curtin International Postgraduate Research Scholarship. To all members of ICRAR and CAASTRO, I appreciate you all for your support, it is a great pleasure knowing and working with you guys.

I acknowledge Curtin Institute of Radio Astronomy (CIRA) for providing good working environment during my study. I would like to appreciate the pulsar group in CIRA. The discussions we had were useful to the completion of this thesis. I would like to thank Haydon Knight for countless discussions and valuable ideas. I am thankful to CIRA staff, whom I had the opportunity of having both formal and informal discussions with. In particular, Drs. Randall Wayth, Cathryn Trott, Natasha Hurley, James Miller-Jones, Paul Hancock, Cormac Reynolds, Wiebke Ebeling, Roberto Soria, Peter Curran and John Morgan; it is a pleasure knowing you guys. I thank the CIRA administrative staff both past and present, in particular, Angela Dunleavy, Tina Sallis, Tanya Jones, Rachel Kennedy and Roselina Stone for their excellent administrative support.

This thesis would not be possible without the support and assistance of the MWA community, in particular, the builders of the MWA telescope. I appreciate you all for working behind the scene and making this thesis a reality. I appreciate the effort of our collaborators at Parkes. I also made use Curtin University Parallel Processor for Astronomy (CUPPA) located at Curtin University. This study was also supported by iVEC through the use of advanced computing resources located at iVEC@Curtin.

To all my fellow postgraduate students, both past and present including

Thomas Russell, Arora Singh Balwinder, Chittawan Choeyesakul, Hongquan Su, Vlad Tudor, Ryan Urquhart, HaiHua Qiao, Rakesh Nath, Divya Palaniswamy and Dr. Hayden Rampadarath, thanks for making the place lively and easing the stress of this program. I appreciate the support of my friends and for showing understanding over my seclusion for the past few years.

To Mary, the love of my life, thanks for being so supportive and having to put up with my grumpy attitudes, especially after Friday meetings at the University. I am really grateful for your patience. To our cute baby, Jesse, thanks for your patience and for understanding my busy schedule as a result of this marathon study. I would like to express my heartfelt gratitude to my parents and siblings, Dr. Austin and family, the Mowete's family, and the Uwumagbe's family for their love, patience and understanding.

May the good lord reward you all.

Abstract

This thesis is a study of giant pulses from the Crab pulsar. The Crab pulsar is a relatively young pulsar known for its giant pulse emission. Giant pulses are short duration radio bursts consisting of complex superpositions of nanosecond- and microsecond-scale impulses. The short duration of these giant pulses imply broadband emission and very high brightness temperatures. We have investigated the broad band nature of the Crab giant pulses with the Murchison Widefield Array and the Parkes radio telescope, as well as their spectral behaviour at low radio frequencies.

The first part of this thesis focuses on simultaneous observations of the Crab pulsar's giant pulses with the MWA operating at a centre frequency of 193 MHz with 15 MHz bandwidth and the Parkes radio telescope operating at center frequency of 1382 MHz with 340 MHz bandwidth. We detected 55 giant pulses at the MWA and 2075 at the Parkes radio telescope. We estimated a power-law index of $\beta = -3.35 \pm 0.35$ and $\beta = -2.85 \pm 0.05$ for the fluence distribution of the giant pulses observed at the MWA and Parkes respectively.

A search for coincident pulses was performed on the giant pulses detected at the MWA and the Parkes radio telescope. We detected 51% of the MWA giant pulses at Parkes, with spectral indices (α) in the range of $-3.6 > \alpha > -4.9$. We performed a Monte Carlo analysis to investigate the less than 100% correlation observed between the MWA and Parkes observations. The analysis supports the conjecture that the giant pulse emission in the Crab is intrinsically broadband, a reduced correlation is seen due to the relative sensitivities of the two instruments and the width of the spectral index distribution. Our results are consistent with the hypothesis that the spectral index of giant pulses is drawn from normal distribution of standard deviation 0.6, but with a mean that displays an evolution with frequency from -3.0 at 1382 MHz, to -2.85 at 192 MHz.

Finally, we simultaneously observed the Crab pulsar at three frequency bands within the full bandwidth of the MWA, centred at 120, 165, and 210 MHz. We

detected two pulses simultaneously in all the three frequency bands, while eight pulses were observed simultaneously at 165 and 210 MHz bands, with spectral indices in the range of $-1.27 \pm 0.14 > \alpha > +1.34 \pm 0.24$. The observed spectral indices are significantly shallower than the results obtained from MWA and Parkes simultaneous observations, and suggest an evidence of a possible turnover in giant pulse spectra at low frequencies.

Contents

Acknowledgements	vii
Abstract	ix
List of Figures	xv
1 Introduction	1
1.1 Motivation	1
1.2 Scope of the Thesis	2
1.2.1 Giant Pulses from the Crab Pulsar	3
1.3 Thesis Outline	6
1.4 Statement of Originality	6
2 Background Theory and Instrumentation	7
2.1 Literature Review of Pulsars	7
2.1.1 Introduction	7
2.1.2 The Pulsar Magnetosphere	8
2.1.3 Classification of Pulsars	10
2.1.3.1 Rotation Powered Pulsars	10
2.1.3.2 Magnetic Powered Pulsars	11
2.1.3.3 Accretion Powered Pulsars	12
2.1.4 The Internal Structure of a Neutron Star	13
2.1.5 Pulsar Dynamics	15
2.1.6 Propagation Effects of Radio Pulses	17
2.1.6.1 Dispersion	17

2.1.6.2	Scintillation	19
2.1.6.3	Multipath Scattering	20
2.1.6.4	Radio Frequency Interference	20
2.2	Instrumentation	21
2.2.1	Basic Characteristics of Radio Telescopes	21
2.2.1.1	Antennas	21
2.2.1.2	Receivers	24
2.2.1.3	Backends	24
2.2.2	Telescopes used in this Thesis	25
2.2.2.1	The Murchison Widefield Array	25
2.2.2.2	The Parkes Radio Telescope	28
2.2.3	Considerations in single pulse studies	29
3	Simultaneous Observations of Giant Pulses from the Crab Pulsar, with the MWA and the Parkes Radio Telescope	33
3.1	Introduction	33
3.2	Observations	35
3.2.1	Parkes Observations	35
3.2.2	MWA Observations	35
3.3	Data Analysis and Results	36
3.3.1	Parkes Data Analysis	36
3.3.2	MWA Data Analysis	38
3.3.2.1	Incoherent Beamforming and De-dispersion	38
3.3.2.2	Measuring the Properties of Giant Pulses	38
3.3.3	The Giant Pulse Fluence Distribution	40
3.3.4	Pulse Shape and Scattering	42
3.3.5	Coincidences in the MWA and Parkes Giant Pulse Arrival Times	43
3.3.6	Spectral Indices of Coincident Giant Pulses	45
3.4	Discussion	45
3.4.1	The Fluence Distribution	45
3.4.1.1	Comparison with the Literature	45

3.4.1.2	Effects of Scintillation	47
3.4.2	Correlated Detections and Intrinsic Giant Pulse Spectral Index Distribution	47
3.4.2.1	Fine Tuning the Analysis	50
3.4.3	Propagation Effects within the Nebula	53
3.5	Conclusion	54
4	Multifrequency Study of Crab Giant Pulses with the MWA	57
4.1	Introduction	57
4.2	Observation	58
4.3	Data Processing and Analysis	59
4.4	Giant Pulse Spectral Indices	61
4.5	Summary and Conclusion	64
5	Conclusions and Future Work	67
5.1	Conclusions	67
5.2	Future Work	69
	Bibliography	71
	Publications	91

List of Figures

1.1	The average emission profiles of the Crab pulsar from radio to γ -ray, showing the mainpulse (left peak) and the interpulse (right peak) phase of the pulsar rotation. Source: Moffett and Hankins (1996)	4
2.1	$P - \dot{P}$ diagram showing the distribution of the known pulsar population, consisting of radio pulsars, “radio-quiet” pulsars, soft-gamma repeaters and anomalous X-ray pulsars. The binary systems are circled, and pulsar-supernova remnant associations are shown by the stars. The diagonal lines show loci of constant dipole magnetic field and spin-down age. Also indicated here are the “Vela-like” and “Crab-like” (the subject of this thesis) pulsars.	8
2.2	Illustration of essential features of a pulsar magnetosphere where the rotation and magnetic axis are misaligned. The electromagnetic radiation is governed by high-energy particles that are constrained to move along the open field lines over the magnetic poles. The pulses are often highly polarised, and integrated pulse profiles are formed by summing many successive pulses and polarised components appropriately (Lorimer and Kramer, 2004).	10
2.3	A neutron star accreting from a companion star that has reached its Roche lobe. Matter is transferred from the companion star onto the neutron star to form an accretion disc around the star. Angular momentum from the companion star is also transferred to the neutron star during this process, thereby increasing the rotation rate of the neutron star. The resulting pulsars are usually millisecond pulsars in this case (credit: ESA space images).	12

2.4	A schematic section of the internal structure of a typical pulsar of mass $1.4 M_{\odot}$ and radius 10 km. The rigid crust and the superfluid core are believed to be responsible for rotational irregularities (glitches and timing noise) observed in some pulsars. (Source: www.mssl.ucl.ac.uk/www_astro/lecturenotes/hea/pulsars/sld021.htm)	14
2.5	Dispersion of pulsar J1644-4559. The observing bandwidth was channelised into 96 frequency bands, 3 MHz wide each, centred at 1380 MHz. As can be seen from the figure, the signal at high frequency arrives before the signal at lower frequency (Source: Lyne and Graham-Smith, 2005). The lower panel shows the de-dispersed signal.	18
2.6	Dynamic spectrum of the radio signal from PSR J0437-4715 observed with the MWA at a centre frequency of 192.6 MHz, with a bandwidth of 15.36 MHz. The variation in intensity is a result of interstellar scintillation . The signal is a function of frequency and time. (Source: Bhat et al., 2014)	19
2.7	A typical normalised power pattern of an antenna in rectangular coordinates, with horizontal axis showing angle from the aperture axis in radians. The aperture axis is an axis perpendicular to the aperture plane.	23
2.8	A photograph of the MWA antenna tiles, with analog beamformer seen as a box on each of the tiles. Each tile (a 4 x 4 dipole array mounted on a 5 x 5 m wire mesh) is laid directly on the ground, with 16 dipoles clipped onto the mesh (credit: Chris Thorne). . .	26
2.9	MWA signal path for pulsar observations.	27
2.10	Pictorial representation of the MWA main beams. (a) Incoherent beam, HPBW $\sim 30^{\circ}$ at 150 MHz. (b) Coherent beam, HPBW $\sim 3'$ at 150 MHz.	28
2.11	Parkes 64-m single-dish radio telescope. Credit: CSIRO/Shawn Amy.	30

3.1	Dedispersed time series for the strongest giant pulse in the MWA data. The yellow (lighter) portions were used to estimate the off-pulse baseline shown by the red line. The off-pulse baseline was determined by the method of least square with a chi-square value of 3.8. The gray (darker) area is the region that was integrated over to measure the total pulse energy. The plot spans 180 ms and has a time resolution of 400μs	39
3.2	The cumulative distribution of the MP giant pulses detected with the MWA. Also shown here is MLE power-law fit to the distribution, with a power-law index of -2.35 ± 0.35 . The shaded region is a ± 0.35 error in the power-law index.	42
3.3	Distribution of the MP giant pulses detected with the Parkes radio telescope. The plotted errors of fit might be underestimated. The solid line is the MLE power-law fit to the data with a power-law index of -2.85 ± 0.05 . The shaded is region is a ± 0.05 error in the power-law index.	43
3.4	A plot showing the search for coincident giant pulses in the MWA and the Parkes arrival times. We identify a 36.000 s clock error in the timestamps of the recording machine used at Parkes at the time of this observation (see text). We used the arrival times of the Parkes giant pulses to search for coincidence in the MWA pulse arrival times. As can be seen in the figure, we found strong peak corresponding to 23 pulses at -30.248 s. Correcting for the 36 s offset yields 5.75 s which corresponds to the time delay between the arrival times of the MWA and the Parkes pulses.	44
3.5	The fluence in Jy-s of the coincident giant pulses detected with the MWA and Parkes. The error bars indicate the uncertainty in the sky temperature measurement for the MWA (which translate to ± 0.08 Jy s in this case), which is negligible at the Parkes frequency. The vertical and the horizontal dash lines are the detection thresholds for the MWA and the Parkes observations. The solid lines are spectral indices $\alpha = -3.6$ and $\alpha = -4.9$. This figure is similar to Figure 7 of Sallmen et al. (1999), in which they constrained the spectral indices within the range of $-2.2 > \alpha > -4.9$	46

3.6	The results of the Monte Carlo analysis to determine the best fit intrinsic mean spectral index of the giant pulses. The three constraints, number of coincident detections (23), observed correlation factor (50%) and distribution of observed spectral indices cannot be satisfied by the same input distribution.	49
3.7	Fine tuning the Monte Carlo analysis by incorporating an overestimate of the MWA sensitivity by 10% and a mild (5%) evolution in the spectral index as a function of frequency produces an internally consistent estimate for the mean of the spectral index distribution(−3.00 at 1382 MHz, to greater than −2.85 at 192 MHz).	52
4.1	Single-pulse search result for 165 MHz band. The top left plot is a histogram of S/N of the detected pulses. The top middle plot is the number of pulses as a function of DM. The top right plot is a scatter plot of the S/N and DM. The bottom panel is a plot of DM as a function of time.	59
4.2	A plot showing a broad band giant pulse observed simultaneously in the three observed frequency bands, 210, 165, and 120 MHz from top to the bottom, after removing the baseline. The dispersive time delay between the bands has been removed.	60
4.3	Plots of the spectra of the detected giant pulses at all three frequencies. The filled circles denote the pulses that were detected simultaneously in the three frequency bands, 120, 165, and 210 MHz. The blue colour indicates the beam-corrected fluence, while the black colour is the uncorrected fluence. The error bars reflect the relative measurement uncertainty in the fluence. We acknowledge that the fluence at the lowest frequency band may be underestimated due to the increased scattering.	61
4.4	Plots of radio spectra of the detected giant pulses at 165 and 210 MHz. Also shown here is the upper limit (inverted arrow) at 120 MHz band where the pulses were not detected. The blue colour indicates the beam corrected fluences, while the black colour indicates the uncorrected fluences. The error bars reflect the relative measurement uncertainty in the fluences.	66

Chapter 1

Introduction

1.1 Motivation

Pulsars are among the most fascinating astrophysical objects in the Universe. They offer opportunities to study a range of astrophysical phenomena. For instance, pulsar studies have confirmed the existence of extra-solar planets (Wolszczan and Frail, 1992), demonstrated the effect of gravitational waves (Hulse and Taylor, 1975), and have provided some of the most stringent tests of general relativity (e.g. Kramer et al., 2006). The timing stability of millisecond pulsars is unsurpassed, which makes them the **objects of choice for tests of general relativity in the strong-field regime and detection of ultra-low-frequency gravitational wave experiments** (e.g. the pulsar timing arrays; Manchester et al., 2013). The study of pulsars is also useful in characterising the electron density distribution in the Galaxy, helping to determine the Galactic magnetic field, and in understanding the polarisation properties of radio pulsar signals. Analysis of single pulses from some objects (e.g. the Crab pulsar) provide valuable insights into the poorly understood astrophysical plasma processes associated with the pulsar emission mechanism (e.g. Hermsen et al., 2013). Finally, the observed changes in single pulses with frequency and time are valuable tools in probing the properties of the interstellar medium via scattering, dispersion, and scintillation (Rickett, 1990; Bhat et al., 2003; Cordes et al., 2004).

Pulsars were originally discovered via radio pulsations at a low radio frequency of 81.5 MHz (Hewish et al., 1968). Subsequent observations have shown that they emit radiation across the electromagnetic spectrum from as low as 17 MHz and up to 87 GHz (e.g. Bruck and Ustimenko, 1977; Morris et al., 1997) in the radio, and at optical, X-ray, and γ -ray frequencies (e.g. Thompson, 2008; Abdo et al.,

2013; Breton et al., 2013; Bogdanov et al., 2014). Although pulsars were first discovered at low radio frequencies (<100 MHz), the challenges of observing and studying pulsars in this frequency regime (see § 2.1.6) have led to the study of the majority of them at higher frequencies. **Although the effects of scattering is still problematic, the challenges of observing and studying pulsars at low frequencies can now be fairly mitigated by modern computational capabilities and modern electronics.**

The radio astronomy community has recently deployed new radio telescopes operating below 300 MHz, using interferometers of simple dipole antenna elements. Such telescopes include the Low Frequency Array (LOFAR) in the Netherlands (van Haarlem et al., 2013), the Precision Array for Probing the Epoch of Re-ionisation (PAPER) in South Africa (Pober et al., 2011), the Long Wavelength Array (LWA) in the Southwestern United States (Taylor et al., 2012), and the Murchison Widefield Array (MWA) in Western Australia (Lonsdale et al., 2009; Tingay et al., 2013). The MWA is a low frequency interferometric phased dipole array operating within the frequency range of 80 to 300 MHz. This new generation of low frequency interferometers is now being used for a wide range of pulsar science. **For instance, Hassall et al. (2012) performed a wide-band simultaneous study of four pulsars with LOFAR to test the accuracy of the dispersion law over a broad frequency range of 40-190 MHz. Coenen et al. (2014) performed two pilot survey for pulsars and fast transients with LOFAR, in which they discovered two new pulsars and reported the first low-frequency fast-radio burst limit. Recently, Bhat et al. (2014) reported on the low-frequency characteristics of a timing array pulsar PSR J0437–4715 observed with the MWA.**

Based on these considerations, the primary motivation for this thesis is to explore the capability of the MWA for single pulse studies of radio pulsars, **taking advantage of its low frequencies where pulsars tend to be intrinsically brighter.** This thesis will focus on the observations and analysis of giant pulses from the Crab pulsar.

1.2 Scope of the Thesis

The main aim of this thesis is to perform single pulse studies of the Crab pulsar (PSR B0531+21). For this thesis, we used the MWA and the Parkes radio telescope to examine the broad band nature of giant pulses from the Crab pulsar

and attempted to determine their spectral indices. In the following section, we briefly give a general overview of the Crab pulsar’s giant pulses.

1.2.1 Giant Pulses from the Crab Pulsar

While the pulse amplitudes of most pulsars follows a normal distribution, some show bimodal distributions with a finite probability of zero flux density (see Lyne and Graham-Smith, 1998), and others display asymmetric distributions, with a long tail towards very high values of flux density (Luo and Melrose, 2001). The Crab pulsar is a classic example of the latter. It emits radiation across the electromagnetic spectrum from radio to γ -ray energies (see Figure 1.1; Moffett and Hankins, 1996), displaying the different radiation processes in the pulsar magnetosphere, such as synchrotron (radio), incoherent synchrotron (optical and X-ray), and incoherent curvature (γ -ray). The pulsar was originally discovered via its remarkably bright single pulses (Staelin and Reifenstein, 1968), subsequently dubbed “giant pulses”.

The giant pulses can exceed the average pulse flux density by factors of hundreds or thousands. Inferred brightness temperatures are of the order of 10^{30-32} K reaching up to $\sim 10^{41}$ K in observations made at 0.4 ns time resolutions (Hankins et al., 2003; Kostyuk et al., 2003; Cordes et al., 2004; Hankins and Eilek, 2007; Bhat et al., 2008). The pulsar emission mechanism is not well understood; physics **underlying giant** pulse emission is therefore complex. **The giant-pulse emission have been attributed to the spatial variations in relativistically streaming pulsar plasma, which are likely to affect the emission process and further propagate the radio waves. The observed characteristic scale of the plasma inhomogeneities for the micro- and nano-pulses are ~ 3 km and ~ 3 m (Popov et al., 2002; Hankins et al., 2003) respectively. These plasma inhomogeneities are usually associated with the soliton-like structures which may arise in the strong turbulent plasma of pulsar magnetosphere and collapse of wave packets (e.g. Asseo et al., 1990; Asseo, 1996; Weatherall, 1997, 1998; Hankins et al., 2003)**

Also, the giant pulses are believed to result from the inhomogeneity of the angular pattern of the emission cone, which manifest as the pulsar rotates. This theory is strongly supported by observations: the timescales of microstructure are proportional to the pulsar period (Hankins, 1996; Popov et al., 2002), implying the same characteristic angular scale of the emission pattern. Increased pair production

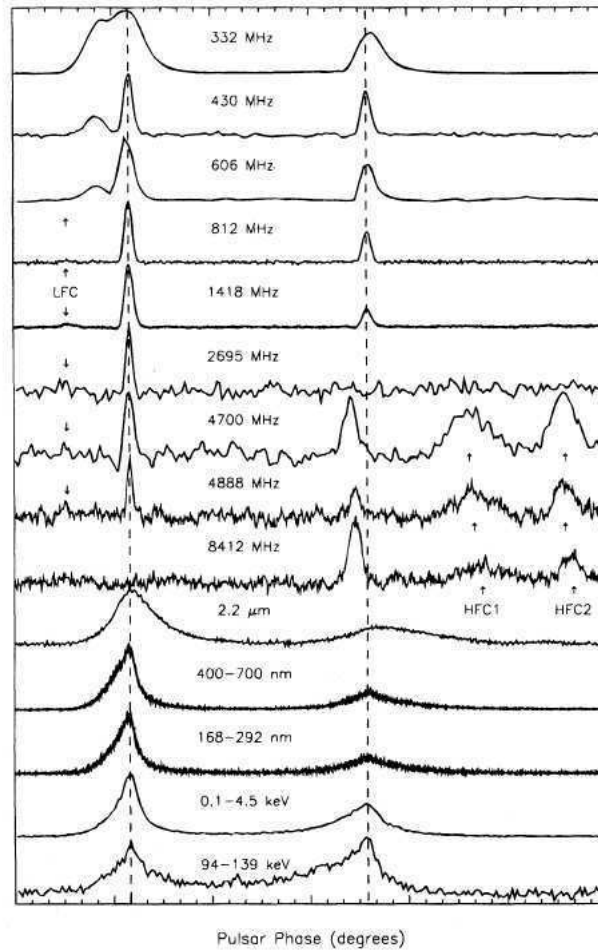


Figure 1.1: The average emission profiles of the Crab pulsar from radio to γ -ray, showing the mainpulse (left peak) and the interpulse (right peak) phase of the pulsar rotation. Source: Moffett and Hankins (1996)

in the pulsar magnetosphere is also believed to be responsible for the additional beaming of radiation. Induced Compton scattering of radio emission off the secondary particles of the ultrarelativistic highly magnetized plasma leads to substantial focusing of the radio photons, so that the resultant beam appears squeezed up to a few hundred times (see Petrova, 2004). This focusing effect is believed to be responsible for the timescales of the observed microstructure as well as its polarization properties (Petrova, 2004). Other theories of the giant pulse emission mechanism includes: (1) linear plasma instabilities such as curvature emission and beam instabilities (e.g. Melrose, 1996; Gedalin

et al., 2002), and (2) linear mode conversion (Melrose and Gedalin, 1999; Cairns et al., 2001). Although these models exist, there is no satisfactory explanation for the occurrence of the giant pulses, nor is there a complete theory of the pulsar emission mechanism in general.

Historically, the giant pulse phenomenon was thought to be a peculiar property of the Crab pulsar. However, the phenomenon has since been observed in a small number of millisecond pulsars PSR B1937+21 and PSR B1821–24 (Cognard et al., 1996; Romani and Johnston, 2001) and the LMC pulsar, **PSR B0540–69** (Johnston and Romani, 2003). For the millisecond pulsars, the highest measured pulse flux density is $\sim 10^3$ Jy at 430 MHz (Romani and Johnston, 2001), while the highest measured pulse flux density for **PSR B0540–69** is ~ 4 Jy (Johnston and Romani, 2003).

The Crab giant pulses have been **observed across a wide** range of radio frequencies. Unlike regular pulses, their temporal occurrence is random, occurring in narrow pulse phase windows within the main-pulse and inter-pulse phase windows that are often aligned with the peaks of pulses seen at X-ray and γ -ray energies (Lundgren, 1994). Giant pulses are not seen to occur in the radio precursor nor at the phases of the high radio frequency components described by Moffett and Hankins (1996), (see also Cordes et al., 2004).

Based on the Heisenberg-Gabor limit (Gabor, 1946), the short duration (ranging from a few ns to a few μ s) of the giant pulses implies broad band emission. Different experiments have been performed to determine the emission bandwidth of the Crab giant pulses. For instance, in the early days of pulsar observations, Comella et al. (1969) reported 50% correlation of giant pulses detected at 74 and 111 MHz. Although simultaneous detection of the giant pulses at two different frequencies has subsequently been reported by a number of studies, high degree of correlations has only been observed for relatively small frequency separations (Sallmen et al., 1999; Bhat et al., 2008) with low percentage correlation for widely separated observations (Popov et al., 2006; Mickaliger et al., 2012).

To further investigate this as part of this thesis, we simultaneously observed the Crab pulsar with the MWA and Parkes radio telescopes, in order to determine the emission bandwidth of the Crab pulsar giant pulses (see Chapter 3). As a follow-up project, we also performed a multi-frequency study of the Crab pulsar giant pulses with the MWA.

1.3 Thesis Outline

In Chapter 2, a theoretical background for the analysis carried out in this thesis is presented. First, a literature review of pulsars is discussed, where all relevant aspects, including propagation effects on pulsar signals and the methodology are discussed. The second part focuses on radio astronomy instrumentation.

Chapter 3 presents simultaneous observations of Crab giant pulses conducted with the MWA and the Parkes radio telescope (Oronsaye et al., 2015).

In Chapter 4, a multi-frequency study of the Crab pulsar with the MWA is presented.

Chapter 5 contains the overall conclusions of the thesis.

1.4 Statement of Originality

Studying pulsars at low frequencies (<300 MHz) is a challenging task. With the development of modern telescopes and software, these challenges can now be overcome. This thesis represents one of the first such studies in the modern era, with a new generation of low frequency radio telescopes. This thesis presents the first analysis of giant pulses with the MWA and the first coordinated pulsar study between the MWA and another radio telescope. The original results of this thesis have been published in the peer reviewed literature (Oronsaye et al., 2015).

Chapter 2

Background Theory and Instrumentation

2.1 Literature Review of Pulsars

2.1.1 Introduction

Pulsars are highly magnetised, rapidly spinning (the spin period ranging from a few milliseconds to a few seconds) neutron stars, which are the end products of the evolutionary stages of massive stars after supernova explosions. As the star collapses, the density becomes large, giving rise to an object that consists mainly of neutrons, with a mass of $\sim 1.4 M_{\odot}$ and a radius of ~ 10 km (Lattimer and Prakash, 2001); they have inferred surface magnetic fields of the order of 10^{11} - 10^{13} G (Beskin and Gurevich, 1993).

Pulsar studies began in 1967 when Jocelyn Bell and Antony Hewish serendipitously discovered strange regular flashes of energy emanating from distinct parts of the sky via pen-chart recordings taken during an interplanetary scintillation survey of the radio sky at 81.5 MHz (Hewish et al., 1968). The periodic signals observed have been remarkably linked with the electromagnetic radiation generated by a rotating neutron star (Gold, 1968; Pacini, 1968). Since then, there have been numerous searches over the past four decades, which have led to the discovery of over 2000 pulsars (e.g. Manchester et al., 2001, 2005; Cordes et al., 2006; Keith et al., 2010). The majority of pulsars are located within the Galactic plane in a layer about 1 kpc thick and within about 10 kpc from the centre of the Galaxy (Lorimer and Kramer, 2004). Only a very few pulsars have been found outside the Milky Way (Globular clusters, large and small magellanic clouds).

This is not surprising, owing to the faint nature of their radio emission (typically 0.1 - 1 mJy at 1400 MHz and 1-10 mJy at 400 MHz; for pulsars within a distance of few kpc; $1 \text{ Jy} = 1 \times 10^{26} \text{ Wm}^2 \text{ Hz}^1$), and a host of propagation effects in the interstellar medium (see § 2.1.6) which further limit the prospects of finding them, particularly the distant ones.

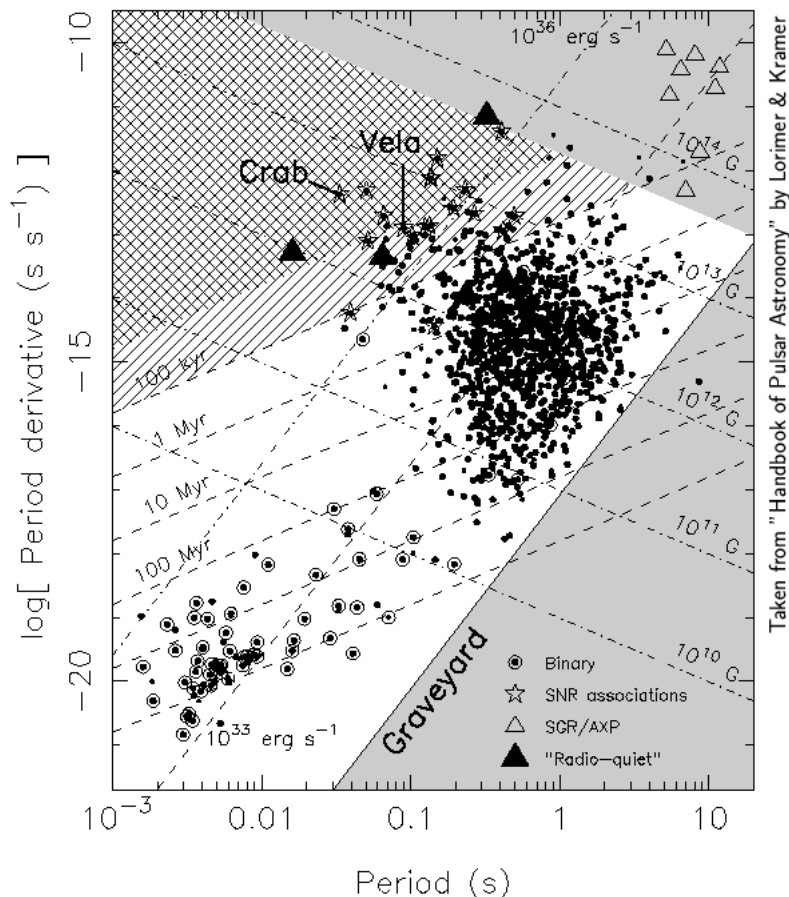


Figure 2.1: $P - \dot{P}$ diagram showing the distribution of the known pulsar population, consisting of radio pulsars, “radio-quiet” pulsars, soft-gamma repeaters and anomalous X-ray pulsars. The binary systems are circled, and pulsar-supernova remnant associations are shown by the stars. The diagonal lines show loci of constant dipole magnetic field and spin-down age. Also indicated here are the “Vela-like” and “Crab-like” (the subject of this thesis) pulsars.

2.1.2 The Pulsar Magnetosphere

The mechanism that creates pulsar emission is not well understood, but it is generally believed to occur in the pulsar’s magnetosphere. The magnetosphere is

a plasma-filled region around the star, dominated by magnetic fields co-rotating with the star. At any point within the co-rotating magnetised plasma, the force-free condition $\mathbf{E} + \frac{1}{c}(\boldsymbol{\nu} \times \mathbf{r}) \times \mathbf{B} = 0$ is satisfied (Goldreich and Julian, 1969); where c is the speed of light, ν is the rotation frequency, \mathbf{r} is the position vector relative to the centre of the star, and \mathbf{E} and \mathbf{B} are the electric and magnetic fields of the magnetised plasma, respectively. This theory implies that the magnetic field lines that extend beyond the so-called light cylinder¹ ($r = c/\nu_0$) cannot remain connected, and are therefore “open”, connecting with the ambient magnetic fields around the pulsar (see Lorimer and Kramer, 2004). The field lines within the light cylinder are “closed”. This closed region of the field lines is filled with sufficient plasma to provide the co-rotation electric field $\mathbf{E} = -(\boldsymbol{\nu} \times \mathbf{r}) \times \mathbf{B}$. The open field line region defines the polar cap on the surface of the pulsar which is centred on the magnetic pole. The observed beam of radiation occurs as a result of the acceleration of high-energy particles along the open magnetic field lines. The mechanism responsible for this beam of radiation is not fully understood, but the excitation of normal modes of the pair plasma in the polar-cap region by instabilities are believed to be responsible. The region of radio emission is believed to be relatively close to the inner acceleration gap near the pulsar surface, while the high-energy emission region is thought to be in the outer acceleration gap near the light cylinder (Cordes, 1992).

A simplified version of the model of a pulsar and its magnetosphere is shown in Figure 2.2, where the magnetic and rotation axes are seen to be substantially misaligned. Based on classical electrodynamics (see Jackson, 1998), a rotating magnetic dipole generates electromagnetic waves at the rotation frequency and loses energy at a rate

$$\dot{E}_{dipole} = \frac{2}{3c^3} |m|^2 \nu^4 \sin^2 \alpha, \quad (2.1)$$

where $|m|$ is the magnetic dipole moment and α is the angle between the magnetic and the rotation axes. This accounts for the main loss in rotation energy and the observed slow-down in the rotation speed of pulsars (see Kaspi et al., 1994; Espinoza et al., 2011).

Since their discovery, a variety of pulsar emission signatures have been observed (e.g. Gavriil et al., 2002). This has led to the classification of pulsars discussed in the following section.

¹The maximum distance the co-rotating speed equals the speed of light.

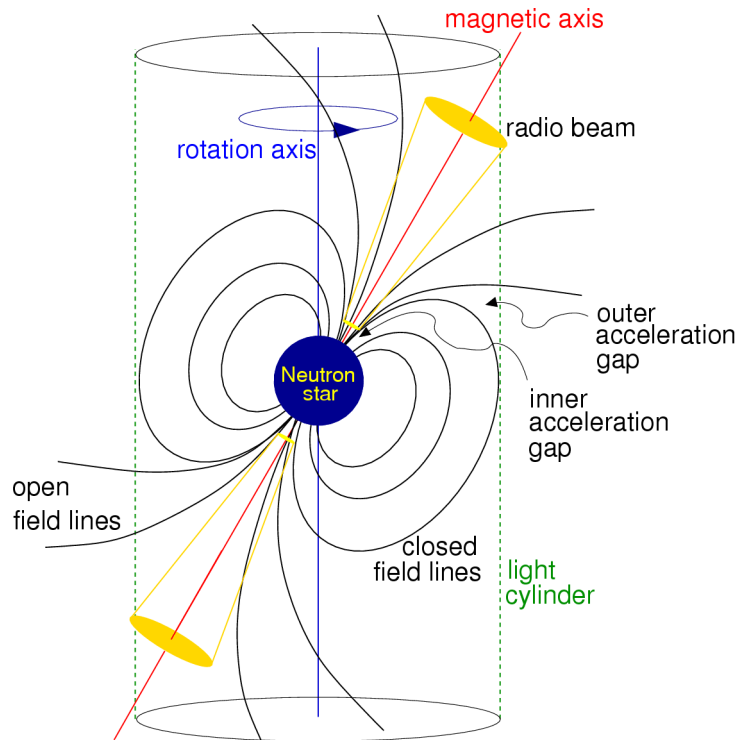


Figure 2.2: Illustration of essential features of a pulsar magnetosphere where the rotation and magnetic axis are misaligned. The electromagnetic radiation is governed by high-energy particles that are constrained to move along the open field lines over the magnetic poles. The pulses are often highly polarised, and integrated pulse profiles are formed by summing many successive pulses and polarised components appropriately (Lorimer and Kramer, 2004).

2.1.3 Classification of Pulsars

2.1.3.1 Rotation Powered Pulsars

This group of pulsars forms the most prominent class within the pulsar population and the most commonly observed (e.g. Manchester et al., 2001; Cordes et al., 2006). **They are powered by the rotational kinetic energy intrinsic to the neutron star**, and release electromagnetic radiation due to their time varying magnetic fields. The rotation powered pulsars emit radiation over a broad spectrum from radio to high energy γ -ray frequencies. The radiation is mainly observed in the radio frequency band, hence they are often called “radio pulsars”. A number of them have also been observed in the optical, infrared, X-

ray and γ -ray energy spectrum (e.g. Archibald et al., 2009; Papitto et al., 2013). The emitted radiation is at the expense of the rotational kinetic energy of the pulsar, and results in the gradual slow-down of pulsars. Although most pulsars in globular clusters appear to be spinning up due to their acceleration in the gravitational potential of the cluster (Wolszczan et al., 1989; Biggs et al., 1994), most rotation powered pulsars are observed to be slowing down steadily with a positive period derivative, \dot{P} (e.g. PSR B0531+21, PSR B0154+61; Espinoza et al., 2011) though glitches (sudden increase in rotation rate, often followed by quasi-exponential period recovery) and timing noise (continuous, erratic fluctuation in rotation behaviour) have been observed in some young pulsars (Cordes and Helfand, 1980; Lyne, 1987; Lattimer and Prakash, 2004; Hobbs et al., 2010).

2.1.3.2 Magnetic Powered Pulsars

Magnetic Powered Pulsars, generally referred to as magnetars, are thought to predominantly derive their power from the magnetic field decay of the neutron star. This class of pulsars is believed to possess surface magnetic fields that are two or three orders of magnitude greater than the surface magnetic field ($10^{14} \lesssim B \lesssim 10^{15} \text{ G}$) of rotation powered pulsars. The decay of this extreme magnetic field powers a high-luminosity burst and also a considerable fraction of the steady X-ray emission (Woods and Thompson, 2006). Two groups of pulsars, Anomalous X-ray Pulsars (AXPs) and Soft Gamma-ray Repeaters (SGRs), are believed to be magnetars (see Kouveliotou, 2003; Woods et al., 2004).

SGRs were first discovered in 1979 as bursts of gamma-rays, and were originally classified as classical Gamma-Ray Bursts (GRB) with a short duration and a soft spectrum (Mazets and Golenetskii, 1981). It was realised in 1986 that these bursts were SGRs, a class of objects different from the classical gamma-ray bursts (Atteia et al., 1987). The SGRs are high energy transient burst sources that are spinning down rapidly. They are characterised by repetitive emissions of bright bursts of soft gamma-rays of short duration, ~ 0.1 s and peak luminosities of $\sim 10^{41} \text{ ergs s}^{-1}$ which is higher than the Eddington limit for a $1.4 M_{\odot}$ pulsar (Woods and Thompson, 2006).

Much like the SGRs, the AXPs emit multiple, regular pulsations with a spectrum softer than the SGRs emissions (Camilo et al., 2006). They have long spin periods in the range of 5 to 9 s, and exhibit a slow-down in rotation speed (Woods and Thompson, 2006). They emit transient bursts similar to the SGRs. The nature of this class of pulsars was first established in 1995 (Mereghetti et al.

1995) when it was realised that a handful of X-ray pulsars share a set of common characteristics different from the accretion powered pulsars (next section).

The similarities in the observed properties of SGRs and AXPs show that they are fundamentally the same type of objects. Their X-ray emission is substantially higher than can be accounted for by their slowdown energy, the source of energy for their radiative output being magnetic decay (Harding and Lai, 2006; Woods and Thompson, 2006).

2.1.3.3 Accretion Powered Pulsars

Accretion Powered Pulsars are highly magnetized rapidly rotating neutron stars that capture matter from a binary companion either by Roche-lobe overflow or by wind accretion (Frank et al., 2002). As a result of the conservation of angular momentum, the accreting matter does not fall directly onto the star, but forms an accretion disc around it (see Figure 2.3), such that the angular momentum is transported outwards as the matter spirals in (e.g. Wijnands, 1999). First observed in the early 70's (Giacconi et al., 1971; Tananbaum et al., 1972),

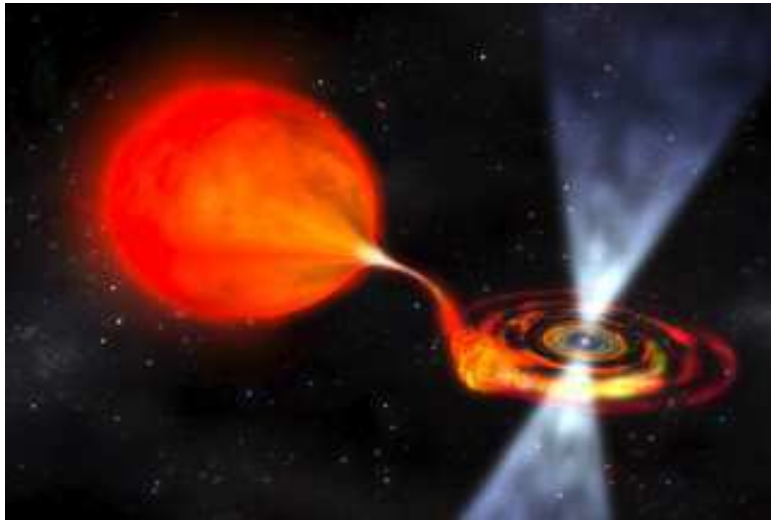


Figure 2.3: A neutron star accreting from a companion star that has reached its Roche lobe. Matter is transferred from the companion star onto the neutron star to form an accretion disc around the star. Angular momentum from the companion star is also transferred to the neutron star during this process, thereby increasing the rotation rate of the neutron star. The resulting pulsars are usually millisecond pulsars in this case (credit: ESA space images).

accretion powered pulsars are the brightest objects in the X-ray sky. Their strong

electromagnetic radiation is powered by the gravitational potential energy of the accreted matter. The accreting matter is directed by the magnetosphere onto the magnetic poles of the star, thereby increasing its energy and angular momentum in the process. The rapid slowdown of the accreting matter at the polar surface of the star releases gravitational potential energy as X-rays, and the rotation of these X-ray hot spots across our line of sight gives rise to the observed periodic emission. **Some pulsars have been observed to switch between the accretion and rotational powered states (e.g. Papitto et al., 2013).**

The subclasses of these pulsars are the high mass X-ray binaries (HMXBs) and the low mass X-ray binaries (LMXBs). In the LMXBs, the mass of the binary companion is usually $< 1M_{\odot}$, while the mass of the companion star in the HMXBs usually exceeds $10 M_{\odot}$ (Wijnands, 1999). accretion powered pulsars can display some changes in their rotation frequency as a result of accretion torque (see Frank et al., 2002). The observations of Bildsten et al. (1997) show that all accreting pulsars exhibit stochastic variations in their spin frequencies and luminosities; while some of these pulsars show secular spin-up, others display spin-down on longer timescales. These behaviours of accretion powered pulsars obscure the conventional distinction between disk-fed and wind-fed accretion powered pulsars (Bildsten et al., 1997).

2.1.4 The Internal Structure of a Neutron Star

Neutron stars consist of matter at the highest densities in the known Universe. Although their composition and properties are not well understood, observations and theoretical predictions have shown that their masses are in the range of 1.2 to $2.0 M_{\odot}$ (Thorsett and Chakrabarty, 1999; Stairs, 2004; Demorest et al., 2010; Lattimer, 2012), with a radius of approximately $10 - 15$ km. A typical pulsar with a mass of $1.4 M_{\odot}$ has a radius of ~ 10 km, and a moment of inertia, $I \sim 10^{45}$ g cm³ (Lorimer and Kramer, 2004). The internal structure of a model $1.4 M_{\odot}$ pulsar is shown in Figure 2.4.

The internal structure of a pulsar consists of the crust and the core. The crust is further subdivided into the outer and the inner crust. The outer crust is a very rigid and crystalline lattice with an approximate density, (ρ) of $10^6 \lesssim \rho \lesssim 10^{11}$ g cm⁻³. At these densities, electrons penetrate the nuclei and combine with protons to form neutron-rich nuclei, surrounded by electrons (Lattimer and Prakash, 2001). As the density increases further in the inner crust, a lattice of heavy neutron-rich nuclei is completely immersed in a neutron fluid (superfluid)

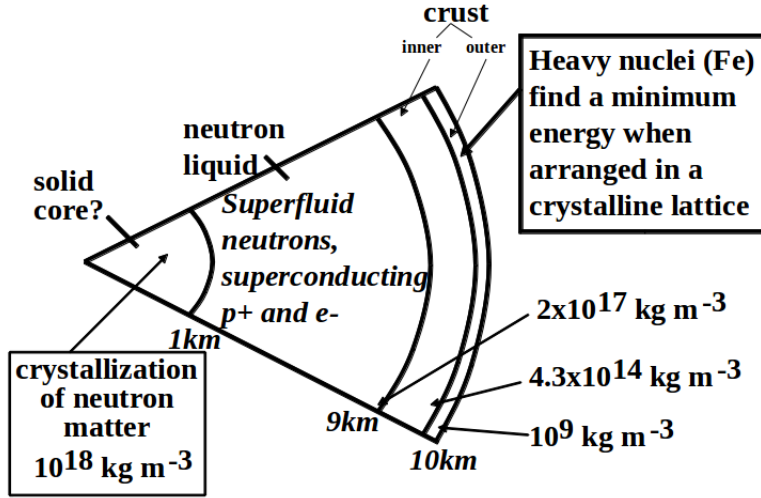


Figure 2.4: A schematic section of the internal structure of a typical pulsar of mass $1.4 M_{\odot}$ and radius 10 km. The rigid crust and the superfluid core are believed to be responsible for rotational irregularities (glitches and timing noise) observed in some pulsars. (Source: www.mssl.ucl.ac.uk/www_astro/lecturenotes/hea/pulsars/sld021.htm)

and relativistic electron gas (e.g. Pines and Alpar, 1985; Lattimer and Prakash, 2001; Newton, 2013). At the densities (up to $4.3 \times 10^{11} \text{ g cm}^{-3}$) present in this inner crust region of the star, the superfluid is isotropic; and above $2 \times 10^{14} \text{ g cm}^{-3}$, a lattice of nuclei can no longer exist. Therefore, the core of a pulsar is expected to consist mainly of **superfluid** neutrons, with an admixture of a few percent of superconducting protons and normal electrons (see Pines and Alpar, 1985; Haensel et al., 2007; Newton, 2013). The core of a pulsar is several kilometres in radius, and accounts for the largest fraction of the stellar mass. It is subdivided into the outer and the inner core. The outer core is made up of matter density in the range of $1.4 \times 10^{14} \lesssim \rho \lesssim 5.6 \times 10^{14} \text{ g cm}^{-3}$, while the inner core occupies the central part of the stellar interior with $\rho \gtrsim 5.6 \times 10^{14} \text{ g cm}^{-3}$ (Potekhin, 2010). The composition and the properties of matter in the inner core are still uncertain; however, there exist the possibilities of exotic matter such as hyperons and deconfined quark matter (see Lattimer and Prakash, 2004; Newton, 2013).

The observed rotational behaviour in pulsars is remarkably linked to the properties of their internal structure. We discuss the general overview of pulsar dynamics in the following section.

2.1.5 Pulsar Dynamics

The rotational kinetic energy of pulsars is generally lost by magnetic dipole radiation or by the outflow of energetic particles accelerated by electromagnetic induction (Lorimer and Kramer, 2004). For magnetic dipole radiation, the rate of loss of rotational kinetic energy, \dot{E} , is obtained by differentiating the rotational kinetic energy $E_{rot} = I\nu^2/2$ with respect to time as derived in Lorimer and Kramer (2004),

$$\dot{E} = -\frac{dE_{rot}}{dt} = -\frac{d(I\nu^2/2)}{dt} = -I\nu\dot{\nu} = \frac{4\pi^2 I dP/dt}{P^{-3}}, \quad (2.2)$$

where I is the moment of inertia, $\nu = 2\pi/P$ is the rotational angular frequency, $\dot{\nu}$ is the spin-down rate, and P is the rotational period. Equation 2.2 applies reasonably well even if part of the energy outflow is carried by energetic particles. \dot{E} quantifies the spin-down luminosity and it describes the total energy output of the pulsar. For a typical pulsar with the canonical moment of inertia, $I = 10^{45}$ g cm²,

$$\dot{E} \simeq 3.95 \times 10^{31} P^{-3} \left(\frac{\dot{P}}{10^{-15}} \right) \text{ ergs}^{-1}, \quad (2.3)$$

where \dot{P} is the period derivative of the pulsar. From equation 2.2, \dot{E} is directly proportional to ν , implying that the most energetic pulsars have high angular frequencies. While a large fraction of the rotational energy is converted into magnetic dipole and high energy radiations, a tiny fraction of it is converted into radio emission (Lorimer and Kramer, 2004).

The expected spin frequency is derived by equating \dot{E} with equation 2.1

$$\dot{E} = \dot{E}_{dipole}, \quad (2.4)$$

$$-I\nu\dot{\nu} = \frac{2}{3c^2} |m|^2 \nu^4 \sin\alpha, \quad (2.5)$$

$$\dot{\nu} = - \left(\frac{2|m|^2 \sin^2\alpha}{3Ic^3} \right) \nu^3, \quad (2.6)$$

$$\dot{\nu} = -k\nu^n \quad (2.7)$$

where

$$k = \frac{2|m|^2 \sin^2\alpha}{3Ic^3} \quad (2.8)$$

is a positive constant which depends on the angle between the rotation and the magnetic axes, the moment of inertia, and the magnetic dipole moment of the pulsar; n is the braking index which depend upon the physics of the braking

mechanism. From equation 2.6, $n = 3$ for pure magnetic dipole braking or particle loss from a completely aligned rotator. The value of n can be determined experimentally by differentiating equation 2.7. This yields

$$\ddot{\nu} = -kn\nu^{n-1}\dot{\nu} = n\nu^{-1}\dot{\nu}^2 \quad (2.9)$$

$$n_{obs} = \frac{\ddot{\nu}\nu}{\dot{\nu}^2}, \quad (2.10)$$

where n_{obs} is the observed value of the braking index, and $\ddot{\nu}$ is the second spin frequency derivative. Only a few young pulsars have had their braking indices measured precisely, and all have values of $n < 3$ (see Lyne et al., 2015). These departures of the observed braking indices from the predicted value had been attributed to pulsar timing irregularities which often manifest as glitches and timing noise. Glitches are almost instantaneous increases in rotation rate, often followed by a quasi-exponential period recovery and some associated temporal behaviours; they have their origin in the neutron star interior (see Espinoza et al., 2011), while timing noise is seen as slow erratic fluctuations in rotation rate and arise from magnetospheric instabilities (Lyne et al., 2010). These changes in the rotation rate occurs on a timescale of months to years, and have a significant effect on the accuracy of the frequency and period derivatives measurement, which in turn affects the observed values of the braking indices of pulsars. The departure of the observed braking indices from the predicted value is also attributed to the time variability of one or more of the parameters I , m and α in equation 2.6 (see Blandford and Romani, 1988; Allen and Horvath, 1997; Lyne et al., 2013). It is also believed that the equation is insufficient to accurately describe the spin evolution of pulsars, since angular momentum can also be lost through mechanical processes such as an outflowing jet or interaction with an external fall-back disc of supernova remnants (e.g. Menou et al., 2001). Harding et al. (1999) and Chen and Li (2006) pointed out that a combination of these processes may account for the deviation of the observed braking indices from the predicted value in young pulsars.

Assuming the pulsar has a constant dipole magnetic field with the spin-down due entirely to magnetic dipole braking, and has an angular velocity that is initially very high at birth, such that the $P_{birth} \ll P_{now}$, equation 2.7 can be integrated to give

$$\tau = -(n-1)^{-1}\nu\dot{\nu}^{-1} = (n-1)^{-1}\left(P\dot{P}\right)^{-1}. \quad (2.11)$$

This equation can also be expressed as

$$\tau_c = \frac{1}{2} (\nu/\dot{\nu}) = \frac{1}{2} \left(P/\dot{P} \right). \quad (2.12)$$

The parameter τ_c is termed the characteristic age of the pulsar. The characteristic ages of pulsars are interpreted with caution as this does not necessarily reflect the true age of the pulsar, seeing that the braking index generally deviates significantly from the predicted value. Moreover, τ_c will not reflect the true age of the pulsar if the current spin period is close to the initial spin period.

2.1.6 Propagation Effects of Radio Pulses

The radio pulsations from pulsars are the valuable clues readily available to pulsar astronomers for probing their physical nature, as well as the interstellar, galactic and intergalactic media. These signals are often distorted via dispersion, multipath scattering, and scintillation as they propagate through the interstellar medium (ISM). These phenomena often distort the time-frequency characteristics of the signals, and are briefly discussed below.

2.1.6.1 Dispersion

Dispersion is due to the frequency dependence of the refractive index of the ionised interstellar gas. This causes signals emitted at high frequencies to propagate faster than those at low frequencies, and smears out pulses in time (e.g. Lorimer and Kramer, 2004). This effect manifests as a quadratic sweep from high to low frequencies in the arrival time of the observed pulsar signal (Figure 2.5). Dispersion also leads to a broadening of the pulse and consequent weakening of pulse intensity, making it more difficult to detect. The dispersive delay Δt , between two frequencies f_1 and f_2 , both measured in GHz is

$$\Delta t \simeq 4.15 \times 10^{-3} \text{ DM} \left(\frac{1}{f_2^2} - \frac{1}{f_1^2} \right) \text{ s} \quad (2.13)$$

where the DM is the dispersion measure in units of $\text{cm}^{-3} \text{ pc}$, defined as

$$DM = \int_0^d n_e dl. \quad (2.14)$$

where n_e is the free electron density, and dl is the infinitesimal path length along the line of sight. Equation 2.13 gives the delay between the arrival time of the pulses at two separate frequencies. Although dispersion adversely affects pulsar

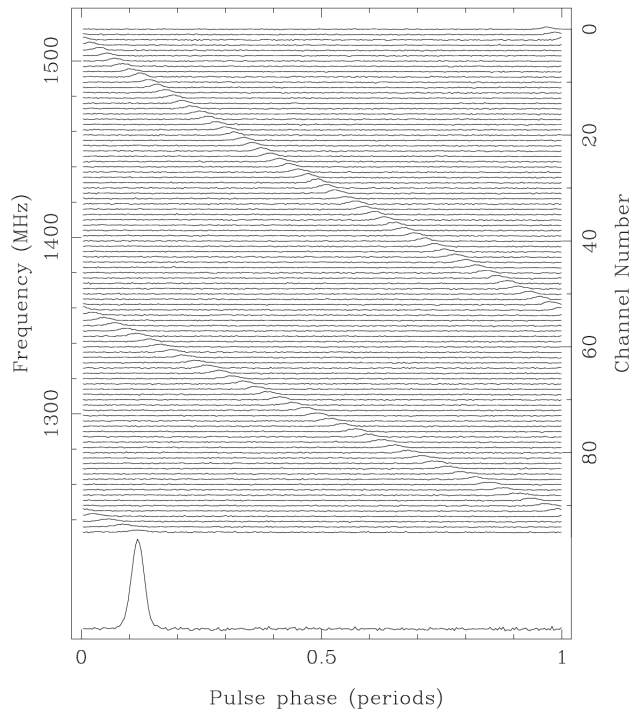


Figure 2.5: Dispersion of pulsar J1644-4559. The observing bandwidth was channelised into 96 frequency bands, 3 MHz wide each, centred at 1380 MHz. As can be seen from the figure, the signal at high frequency arrives before the signal at lower frequency (Source: Lyne and Graham-Smith, 2005). The lower panel shows the de-dispersed signal.

signals, it is a useful tool in characterising its pulses against the background of locally generated radio frequency interference.

The effects of dispersion can be corrected by a process known as de-dispersion, which can either be performed coherently or incoherently. The degree of de-dispersion depends on the technique used. Coherent de-dispersion is an exact de-chirping of the received signal using all available phase information (Hankins and Rickett, 1975). The received electric field has a phase introduced through dispersion. Coherent de-dispersion requires the multiplication of the Fourier amplitudes by the inverse phase function. On the other hand, incoherent de-dispersion involves splitting the observing bandwidth into a large number of frequency channels. The frequency channels can then be shifted by applying the appropriate time delay in order to correct for the quadratic sweep. **This procedure is limited by the width of the individual frequency channels which inherently retain a small fraction of the dispersion delay. This can be detrimental**

in searching for short pulses. For the Crab’s DM, the DM smearing at the 10 kHz channel of the MWA, from 165 to 165.010 MHz is $\sim 1 \mu\text{s}$. Pulses shorter than this will be detected with reduced S/N. Although coherent de-dispersion is preferable to incoherent de-dispersion, it has a high computational burden and is further complicated by the presence of RFI. For the work presented here, the incoherent de-dispersion approach was used.

2.1.6.2 Scintillation

Scintillation is due to inhomogeneities in the ionised interstellar electron density distribution. This phenomenon leads to phase perturbations of the signals passing through it and can result in constructive or destructive interference of radio pulses (Lyne and Rickett, 1968), causing the observed pulse intensity to vary (see Figure 2.6) in time and frequency ($\nu^4 \propto 1/\tau_s$) with characteristic scales of $\Delta\tau_s$ and $\Delta\nu$, respectively. **In an optimistic scenario, a pulsar that is intrinsically too weak to be detectable can become observable (and vice versa in a less favourable scenario).**

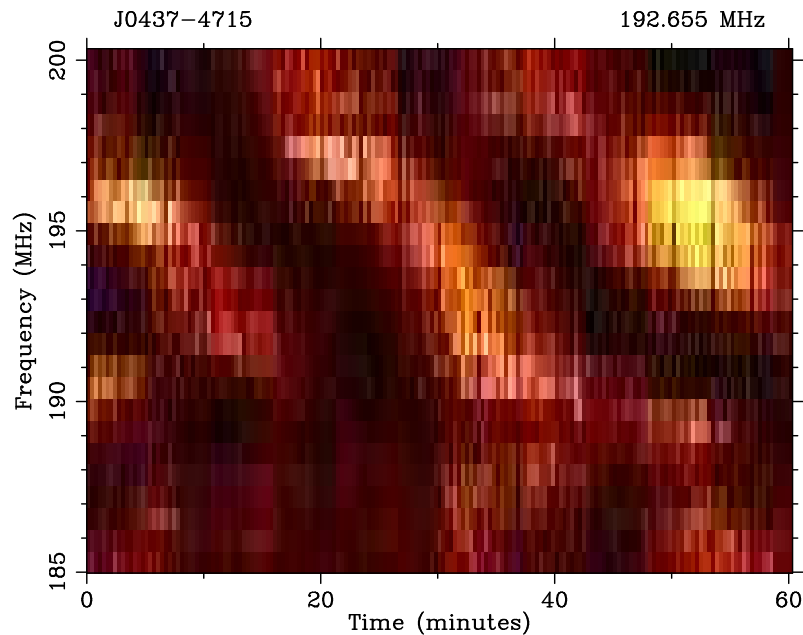


Figure 2.6: Dynamic spectrum of the radio signal from PSR J0437-4715 observed with the MWA at a centre frequency of 192.6 MHz, with a bandwidth of 15.36 MHz. The variation in intensity is a result of interstellar scintillation. The signal is a function of frequency and time. (Source: Bhat et al., 2014)

2.1.6.3 Multipath Scattering

Anisotropies in the electron density distribution of the interstellar medium **result in** refractive index fluctuations. These variations in refractive index in turn scatter the radio signals passing through it, and cause the signals to arrive via multiple paths (see Rickett, 1990), a phenomenon generally referred to as multipath scattering. This results in temporal broadening of the pulse profile of radio pulsars (Bhat et al., 2004). Scattering convolves the original pulse profile emitted by a pulsar with a one-sided exponential tail $e^{-t/\tau_{sc}}$, where τ_{sc} is the scattering time (see Lorimer and Kramer, 2004). The amount of scattering is strongly dependent on the observing frequency ($\tau_{sc} \propto f^{-\alpha}$), with the lowest frequencies showing very high degree of scattering, where $\alpha \simeq 4$. The amount of scattering is positively correlated with DM (Bhat et al., 2004).

Unlike dispersion, there is no well established technique to completely remove scattering from the signal because the phase of the radio signal is randomised along each of many propagation paths. Some authors have suggested procedures for mitigating the effect of scattering. For instance Bhat et al. (2003) applied a procedure analogous to the CLEAN algorithm to deconvolve interstellar pulse broadening from radio pulsars. Demorest (2011) demonstrates the application of cyclic spectral analysis techniques in removing interstellar scattering from the pulse profiles of radio pulsars. While pulse broadening provides valuable information for evaluating the galactic structure of electron density fluctuations, it is detrimental to observations of distant, short period pulsars in the galactic plane whose pulses can become undetectable when observing at low frequencies. This propagation effect is a major challenge when searching for pulsars at low frequencies.

2.1.6.4 Radio Frequency Interference

Pulsar signals are often contaminated with terrestrial radio frequency interference (RFI), making it difficult to identify weaker pulsar signals amidst strong background interfering signals. This effect is particularly problematic for pulsar searching, as it degrades the signal to noise ratio (S/N) of the observation, and can produce many false positives. Many sources of RFI produce periodic broadband noise analogous to that of pulsars, thereby making it difficult to extract pulsar signals. Sources of human-made RFI range from the radio emission from broadcasting stations to those from cell phones and Wi-Fi, power lines, **airplanes and satellites**. The frequencies of these signals are often within the frequency

range of radio pulsar emission.

2.2 Instrumentation

This section presents the main instrumentation employed in this thesis. We begin by introducing the basic characteristics of radio telescopes, with a brief description of the telescope subsystems relevant to the work presented in this thesis. Radio pulsar observations require a telescope with high sensitivity, wide observing bandwidth, and high time and frequency resolution. The application of low frequency dipole arrays for pulsar observations will be discussed. It should be noted that the purpose of this section is not to provide a detailed treatment of the theory behind radio telescopes, but to provide a synopsis of the instrumentation employed in this thesis. A detailed treatment of the concepts presented here can be found in Kraus (1966); and Lorimer and Kramer (2004).

2.2.1 Basic Characteristics of Radio Telescopes

A radio telescope consists of: the antenna, the sub-system that intercepts the electromagnetic waves; the receiver, which filters, amplifies and digitises the analog signal (fluctuating voltage) from the antenna; and the back-end which consists of digital recording devices and data processing elements. These subsystems are briefly described below.

2.2.1.1 Antennas

Radio telescope antennas intercept incident radio waves from astronomical sources of interest and convert them into electrical signals at the antenna terminals or feeds. This weak fluctuating voltage is fed through a transmission line to the receiver electronics, consisting of amplifiers and filters.

Radio telescope antennas range from smooth spherical or parabolic reflecting dishes to simple dipole elements. The reflecting parabolic dishes are the most versatile and powerful antennas popularly used in pulsar astronomy. The parabolic nature of the dish reflecting surface focuses incoming radio waves to the feed. The dishes are often used at short observing wavelengths ($\lambda_{obs} < 1$ m). At longer wavelengths ($\lambda_{obs} > 1$ m), dipole antennas are more practical to use. They consist of two terminals or “poles” that are symmetric about the feed points. The poles are of equal lengths and extend in opposite directions from the feed point.

In order to maintain sensitivity to the different polarisations of the radio waves, two dipoles, placed perpendicular to each other are used. When a radio wave is incident on a dipole antenna, it causes the electrons inside the antenna to oscillate along the direction of the electric field component of the wave, inducing a time-varying voltage which is transmitted to the feed. Dipole antennas are often used as feeds for reflector antennas (Cheng, 2009).

All radio telescope antennas have a characteristic property known as the antenna pattern $P(n)$. The antenna pattern is the directional dependence of radiation (or reception for receiving antennas) from the antenna. It is the geometric pattern of the relative strengths of the field received or emitted by the antenna. In practice, normalised power pattern $P_n(n)$ is used more frequently and it is obtained by dividing the power pattern by its maximum value $P_{max}(n)$. For a given direction in the sky, the normalised power pattern of an antenna in the reception mode is

$$P_n(\theta, \phi) = \frac{P(\theta, \phi)}{P_{max}}, \quad (2.15)$$

where θ and ϕ are the orthogonal direction coordinates. Figure 2.7 is a typical normalised power pattern of an antenna in rectangular coordinates. It consists of the main beam (or main lobe) and the side lobes. Two quantities frequently used as measures of the main beam width are the half power beamwidth (*HPBW*) and the beamwidth between first nulls (*BWFN*) (see Kraus, 1966). The *HPBW* is the angular separation at which the magnitude of the power pattern decreases to half the value at the peak of the main beam, while the *BWFN* is the angular separation at which the magnitude of the power pattern drops to zero between the main lobe and the first side lobe, from the main beam. For a uniformly illuminated circular aperture antenna (Kraus, 1966),

$$HPBW = 1.22 \frac{\lambda}{D} (\text{radians}) \quad (2.16)$$

$$BWFN = 2.44 \frac{\lambda}{D} (\text{radians}), \quad (2.17)$$

where λ is the observing wavelength and D is the diameter of the aperture.

In general, the electromagnetic signal at frequency ν , arriving at the aperture of any given radio antenna can be described in terms of the intensity I_ν , in units of $\text{W m}^{-2} \text{ Hz}^{-1} \text{ sr}^{-1}$, integrated over a delta function solid angle

$$S_\nu = \int I_\nu d\Omega, \quad (2.18)$$

where S_ν , in units of $\text{W m}^{-2} \text{ Hz}^{-1}$, is the flux density². Since a radio telescope

²A convenient unit of flux density is Jansky (Jy). $1 \text{ Jy} = 10^{-26} \text{ W m}^{-2} \text{ Hz}^{-1}$.

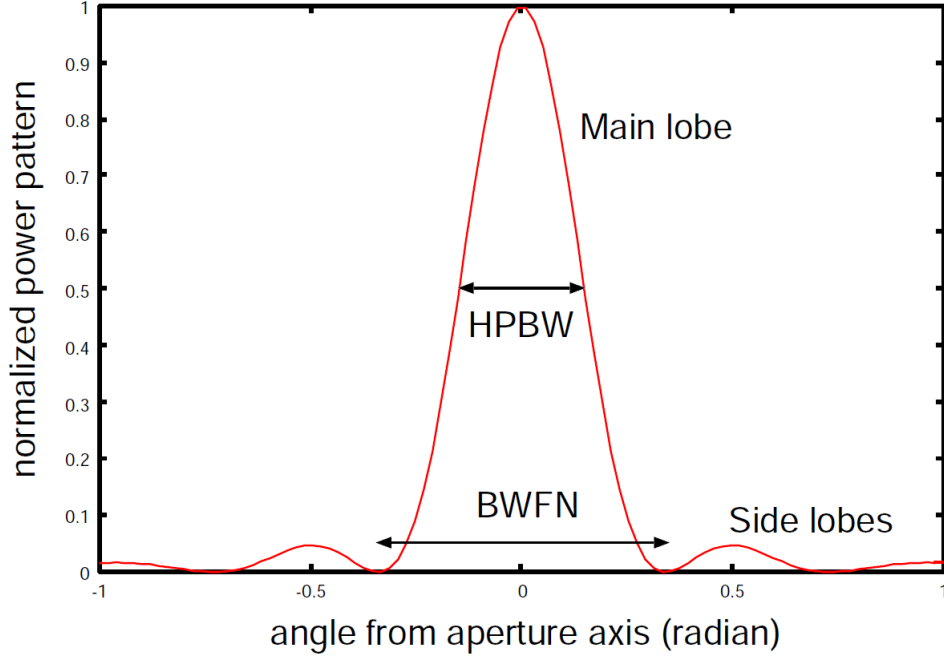


Figure 2.7: A typical normalised power pattern of an antenna in rectangular coordinates, with horizontal axis showing angle from the aperture axis in radians. The aperture axis is an axis perpendicular to the aperture plane.

antenna is used in the reception mode, it is natural to think of it as an area intercepting a power flux and yielding a received power P_{rec} . The power received by the antenna for a randomly polarised source with flux density S_ν is

$$P_{rec} = \frac{1}{2} S_\nu A_{eff} \Delta\nu, \quad (2.19)$$

where A_{eff} is the effective area of the antenna, and the factor of 1/2 accounts for the fact that any single polarisation captures half of the available signal (Goldsmith, 2002). A_{eff} is a function of direction which depends on the direction measured with respect to the main beam axis (see Burke and Graham-Smith, 2010), and it describes how much power is captured from a given EM wave. A_{eff} is related to the antenna gain, G by

$$A_{eff} = \frac{\lambda^2}{4\pi} G, \quad (2.20)$$

where λ is the observing wavelength. The sensitivity of a radio telescope ΔS_{rms} , (rms noise fluctuations in the system) is dependent on G (see Lorimer and Kramer, 2004), such that

$$\Delta S_{rms} = \frac{\beta T_{sys}}{G \sqrt{N_p t_{int} \Delta\nu}}, \quad (2.21)$$

where β is a factor that incorporates both losses due to the quantization of the signal and other systemic effects and is assumed to be unity, N_p is the number of polarisations, t_{int} is the integration time, $\Delta\nu$ is the observing bandwidth, and T_{sys} is the system temperature, the sum of the receiver and sky temperatures.

2.2.1.2 Receivers

The receivers filter and amplify the incoming signal from the antenna. After being brought to focus by the telescope antenna, the radio waves are converted to a fluctuating voltage (RF) by the antenna feed. The feed consists of two receptors sensitive to orthogonal polarisations, linear or circular (Lorimer and Kramer, 2004). The weak RF is amplified by a low-noise amplifier with a characteristic frequency response centred at a radio frequency ν_{RF} within a frequency band. Signals or harmonics of out-of-band interference are removed from the amplified RF by passing it through a bandpass filter. The filtered ν_{RF} signal can then be converted to a lower frequency with a mixer for the purpose of efficient transmission. The mixer beats the ν_{RF} signal with monochromatic signal ν_{LO} , provided by a local oscillator. This yields an intermediate frequency ν_{IF} , at the sum and difference of ν_{RF} and ν_{LO} . The difference is used for the purpose of down conversion, such that $\nu_{IF} = \nu_{RF} - \nu_{LO}$ (see Lorimer and Kramer, 2004). The ν_{LO} is usually less than the ν_{RF} , so that the resulting ν_{IF} which is the upper sideband has the frequency level as the RF. The ν_{IF} is further amplified and recorded.

2.2.1.3 Backends

Generally speaking, the telescope backends are data acquisition devices such as the filterbank spectrometers or correlators, depending on the nature of the radio observations. The analog filterbank spectrometer is commonly used as a data acquisition device for incoherent de-dispersion, where the broad band signal is divided into adjacent frequency channels. The frequency channels are then digitised separately (see Lorimer and Kramer, 2004). The **digitisation** process is achieved by using analog-to-digital converters (ADCs). The ADCs typically have quantizations levels of 8-12 bits but can accomodate only relatively narrow input bandwidths. The simplest digitisation scheme is a one-bit sampling, and can result in a positive or negative output level. This is referred to as “hard clipping”, and can result in a lower signal-to-noise ratio since only part of the information contained in the input is retained (Wilson et al., 2009). Multi-level quantization of an input will preserve more information and will thus result in an

improved signal-to-noise ratio. The digitised data can then be recorded to disk or processed in real time. For this thesis, the polyphase filter bank (PFB) was used as data acquisition device.

2.2.2 Telescopes used in this Thesis

This section presents a brief description of the main instruments used in this thesis.

2.2.2.1 The Murchison Widefield Array

A single reflecting parabolic dish is the simplest telescope popularly used in pulsar astronomy (e.g. the Parkes radio telescope), and provides an angular resolution of approximately λ/D radians. The largest radio telescope of this kind, operating at ~ 1 m wavelength, is the 305 m Arecibo telescope; it gives a resolution of ~ 15 arcmins which is far worse than the resolution achieved by ground-based optical telescopes (typical angular resolution of ~ 0.1 arcsecond, assuming the atmosphere can be ignored). To achieve a higher resolution similar to that of an optical telescope, a radio telescope has to be larger by ~ 5 orders of magnitude, i.e. a radio telescope with an aperture of several hundred kilometres. While that is practically impossible, it is possible to synthesise an equivalent aperture (for angular resolution) by building an array of receiving dishes or dipole elements. This forms the basis of aperture array synthesis. This technique was used in designing **LOFAR (van Haarlem et al., 2013)**, **LWA (Taylor et al., 2012)**, and the **MWA (Tingay et al., (2013); the primary instrument used in this thesis for pulsar observations)**. The details of the principles of interferometry and aperture array synthesis can be found in Thompson et al. (2007).

The MWA is a low frequency interferometric phased dipole array. It consists of 2048 dual-polarisation dipole antennas, arranged as 128 tiles, each of 16 (4 x 4) antennas. Each of the antenna tiles has an analog beamformer which combines the signals from the 16 dipoles to produce an electronic steerable beam on the sky, with a HPBW of approximately 25 degrees at 150 MHz for a zenith pointing (Tingay et al., 2013). The large number of receiving antennas of the MWA (see Figure 2.8) provides a significant collecting area and a wide field-of-view on the sky. It is designed to operate within the frequency range of 80 and 300 MHz, with an instantaneous bandwidth of 30.72 MHz at a spectral resolution of 40 kHz. The MWA is sited at CSIRO's Murchison Radio-astronomy Observatory (MRO) in



Figure 2.8: A photograph of the MWA antenna tiles, with analog beamformer seen as a box on each of the tiles. Each tile (a 4 x 4 dipole array mounted on a 5 x 5 m wire mesh) is laid directly on the ground, with 16 dipoles clipped onto the mesh (credit: Chris Thorne).

Western Australia. This site was chosen due to its low level of human-made RFI, especially in the FM band which is the lower end of the radio frequency range at which the MWA operates. The instrument is designed for the detection of the redshifted neutral hydrogen 21-cm signal from the Epoch of Reionization (EoR), Galactic and extragalactic surveys, Solar, heliospheric and ionospheric studies, as well as transient and pulsar studies (Lonsdale et al., 2009; Bowman et al., 2013; Tingay et al., 2013).

As earlier pointed out, the analog beamformer attached to each of the MWA antenna tiles sums all signals from the 16 antennas, producing two wideband electronic steerable beams, representing the two orthogonal X and Y linear polarisations of the dipole antennas. The beam covers up to about 1000 sq.deg at 150 MHz on the sky. All the antenna tiles are distributed across 3 km, giving an angular resolution of $\sim 3'$ at 150 MHz. The 128 tiles are split into 16 groups of 8 tiles, each with a separate receiver.

The signal path from the antenna to the data acquisition/storage device is

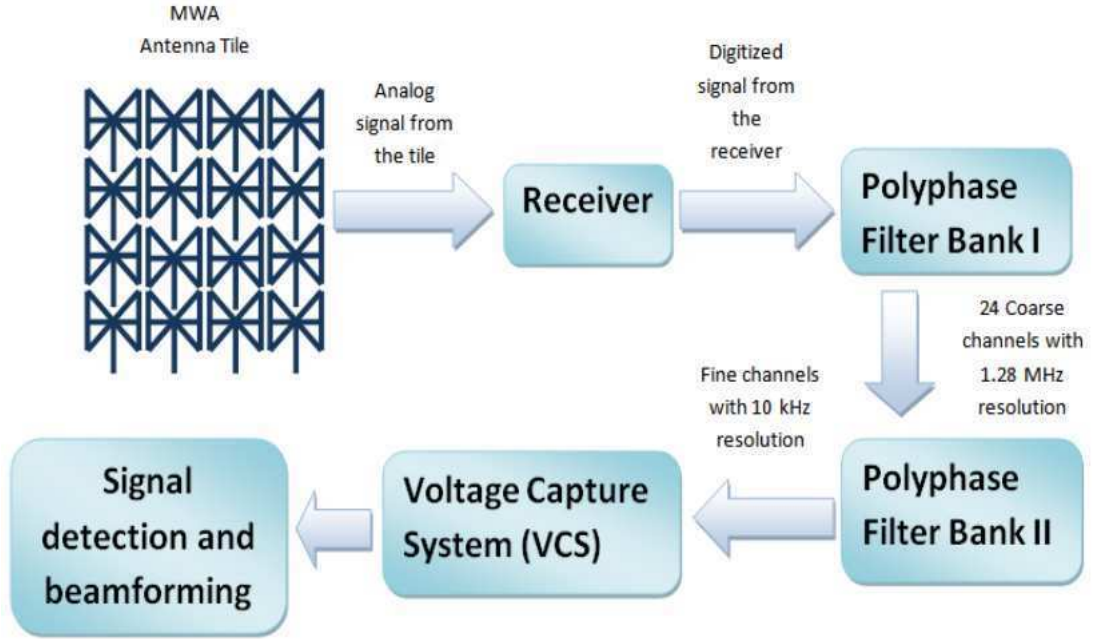


Figure 2.9: MWA signal path for pulsar observations.

such that the radio frequency signals from the antenna tiles are transmitted to the receiver via coaxial cable. The receiver digitises the signals and performs coarse frequency channelisation before transmitting the digitised signals to a central processing unit via fibre optic cable (Prabu et al., 2015). 30.72 MHz of bandwidth is processed, usually in the form of correlation, calibration, and imaging (see Ord et al., 2015; Tingay et al., 2013).

The MWA backend for pulsar observations consists of a second polyphase filter bank (PFB) and a voltage capture system (VCS; Tremblay et al., 2015). The first PFB channelises the digitised signals from the receiver into 24 coarse channels with a resolution of 1.28 MHz. Each of these coarse channels is further divided into 128 fine channels, with a frequency resolution of 10 kHz. The channelised signal is then passed to the VCS, a system which allows the raw complex voltages to be written directly to disk for signal detection and further processing (see Figure 2.9). The details of the VCS are presented in Tremblay et al. (2015).

The sensitivity for pulsar observations with the MWA depends on the mode of signal processing, either coherent combination of the signals from all the antenna tiles or the incoherent combination of the signals. In the incoherent case, the voltage signals from each antenna tiles are first detected and subsequently added to form a single incoherent beam, $B_N = \sum_{i=1}^N V_i^2$, where B_N is the total signal,

N is the number of antenna tiles, V_i is the voltage signal from the i th antenna. The incoherent beam is large on the sky (equivalent to the beamwidth of a single antenna tile) as shown in Figure 4.4a, but with sensitivity proportional to \sqrt{N} according to the equation

$$G_{inco} = \frac{\frac{\lambda^2}{2\pi} (16\sqrt{N})}{2k}, \quad (2.22)$$

where G_{inco} is the incoherent gain, λ is the wavelength of the observation, and k is Boltzmann's constant. In coherent beamforming, the signals from the an-

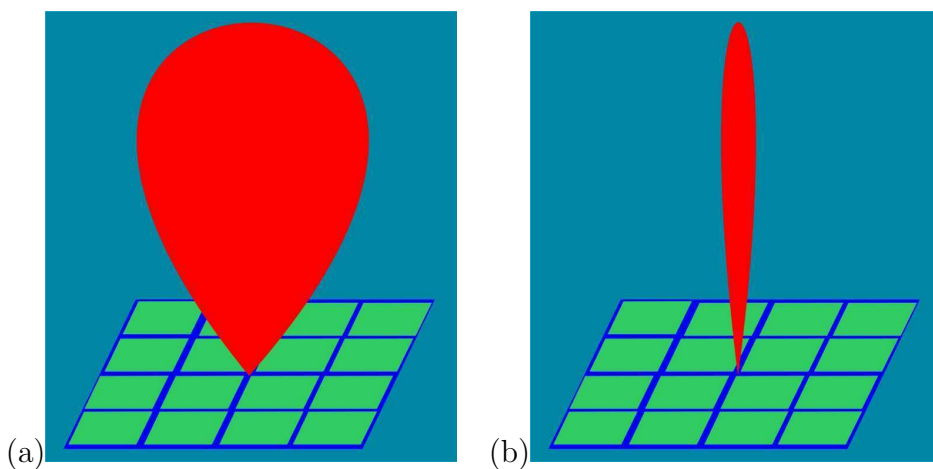


Figure 2.10: Pictorial representation of the MWA main beams. (a) Incoherent beam, HPBW $\sim 30^\circ$ at 150 MHz. (b) Coherent beam, HPBW $\sim 3'$ at 150 MHz.

tenna tiles are added before detection $B_N = (\sum_{i=1}^N V_i)^2$. While the phase of the incoming signal is retained in coherent beamforming, it cannot be recovered in the incoherent procedure. In this case, the beam is narrow on the sky (limited field-of-view) as shown in Figure 4.4b, with a higher sensitivity proportional to N (van Leeuwen and Stappers, 2010) according to the relation

$$G_{co} = \frac{\frac{\lambda^2}{2\pi} (16N)}{2k} \quad (2.23)$$

where G_{co} is the gain of the coherent beam.

2.2.2.2 The Parkes Radio Telescope

The Parkes radio telescope is operated by the Commonwealth Scientific and Industrial Research Organisation (CSIRO) as part of the Australia Telescope

National Facility (ATNF) network of radio telescopes. It is a 64-m single-dish parabolic reflector (Figure 2.11) situated near the town of Parkes in New South Wales, Australia. The Parkes Radio Telescope is a fully-steerable radio telescope, and among the largest single-dish radio telescopes in the world. The telescope was built in 1961, but only its basic structure has remained unchanged. The surface, control system, focus cabin, receivers, computers and cabling have all been upgraded to keep the telescope current (see Staveley-Smith et al., 1996; Keith et al., 2010). The telescope is equipped with a multi-beam receiver. The receiver consists of 13 feeds at the prime focus of the 64-m single-dish, organized as a central feed surrounded by two hexagonal rings (see Keith et al. (2010) for details). Although it is an altitude-azimuth mounted telescope, it is steered by following the motion of a small equatorially mounted telescope located within the structure of the main telescope. The telescope is one of very few large radio telescopes capable of seeing the extensive portion of the Galactic plane which lies at southern declinations. Since the inception of the telescope, different backends have been developed for pulsar observations; one of such backends is the Berkeley-Parkes Swinburne Recorder (BPSR; Keith et al., 2010) which was employed in this thesis.

The BPSR is a digital backend consisting of 26 digital spectrometers connected to 13 server-class workstations that format the data and write it to disk. Each spectrometer consists of two analog-to-digital converters and two polyphase filters. The polyphase filters implemented on the field-programmable gate array (FPGA) in the BPSR channelise the digitised data into 1024 channels with a spectral resolution of 390 kHz. Each of these channels is subsequently detected and integrated over 25 samples to yield a time resolution of 64 μ s.

2.2.3 Considerations in single pulse studies

Although pulsars are well known for their precise periodicity, some pulsars have been found to occasionally emit strong individual pulses, often $\gg 10$ times stronger than their average pulse, called the giant pulses. A single pulse search procedure is applied to detect these pulses rather than periodicity search methods (not described here). In this section, we briefly discuss aspects of single pulse search studies relevant to this thesis. Descriptions specific to the research done in this thesis are given in more detail in chapters 3 and 4. The discussion here closely follows the procedures described in Cordes and McLaughlin (2003).

The intrinsic widths and temporal shapes of detected radio pulses are influ-

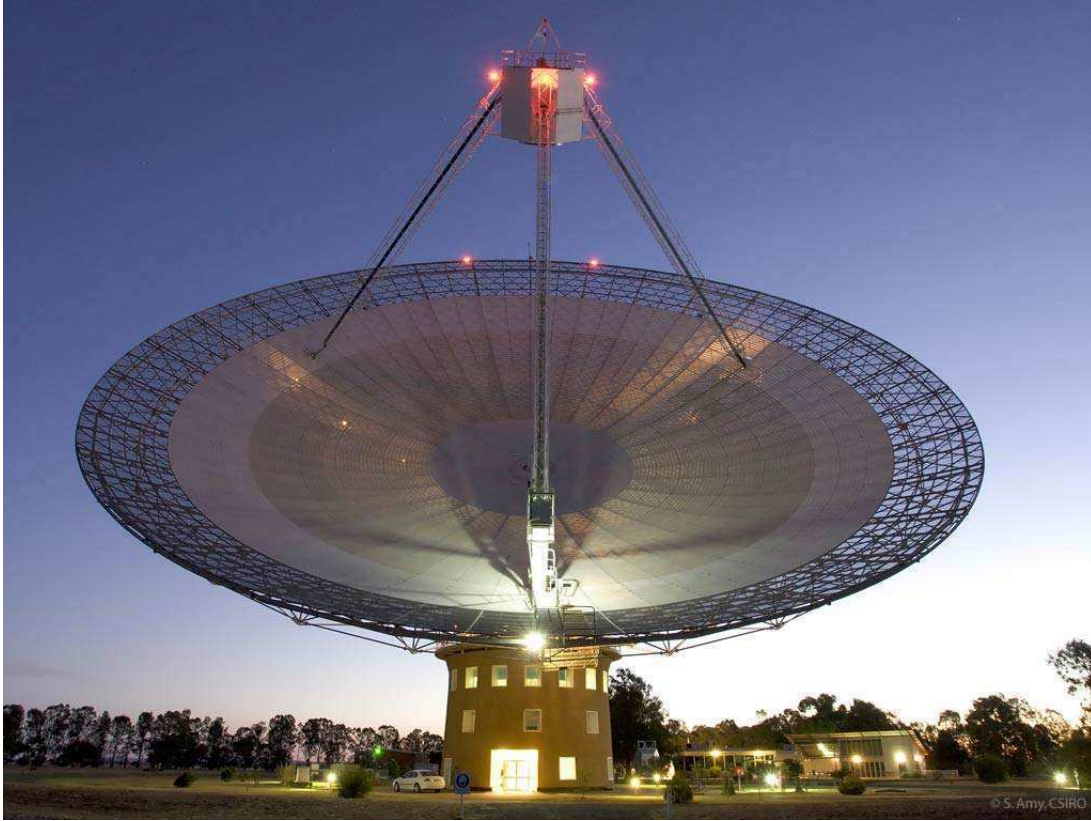


Figure 2.11: Parkes 64-m single-dish radio telescope. Credit: CSIRO/Shawn Amy.

enced by a combination of propagation effects and signal-processing. The factors influencing the temporal shape, width, and intensity of a radio pulse are the frequency dependent broadening due to dispersion, interstellar scattering, de-dispersion error broadening, and broadening resulting from the use of finite-sized frequency channel widths. The effective time resolution of a pulse is a quadratic sum of these effects (Cordes and McLaughlin, 2003), such that the observed effective width of a pulse is

$$\Delta t_{obs} = \sqrt{\Delta t_{DM}^2 + \Delta t_{\delta DM}^2 + \Delta t_{\Delta\nu}^2 + \tau_s^2}. \quad (2.24)$$

The first term in equation 2.24 is the amount of DM smearing across a finite bandwidth $\Delta\nu$ at a centre frequency of ν GHz, and it is given by

$$\Delta t_{DM} = 8.3 \Delta\nu \text{ DM } \nu^{-3} \mu s. \quad (2.25)$$

For optimal detection, the DM smearing across the observing bandwidth needs to be removed from the measured signal by compensating time delays. This was

achieved in this thesis by shifting the signal from each frequency channel by the predicted dispersive delay, $t_{\text{delay}} = 4.15 \text{ DM } \nu_{\text{GHz}}^{-2}$ for a particular DM, a procedure generally referred to as incoherent de-dispersion (see § 2.1.6). In a blind search for single pulses, the DM is not known beforehand. As a result, a range of DM trials is generally used to de-disperse the data. In this procedure, if the trial DM is in error by δDM , the pulse will be smeared by the second term in equation 2.24 given by

$$t_{\delta\text{DM}} = \Delta t_{\text{DM}}(\delta\text{DM}/\text{DM}). \quad (2.26)$$

While searching for pulses over a large DM step can significantly broaden the pulses and hence cause loss of sensitivity, a very small DM search step can result in waste of computational power in generating and searching de-dispersed timeseries that are effectively identical (see Lorimer and Kramer, 2004). As a result, it is imperative to make a choice of DM step that is not too large or too small. The best choice of DM step is one in which the time delay between the high and low frequency sub-bands equals the data sampling interval. The i^{th} value of the DM, in terms of the $\Delta\nu$ and ν can then be written as

$$\text{DM}_i = 1.205 \times 10^{-7} \text{ cm}^{-3} \text{ pc}(i-1)t_{\text{samp}}(\nu^3/\Delta\nu), \quad (2.27)$$

where t_{samp} is the sampling interval. The de-dispersed timeseries for each DM is obtained by averaging in frequency at each particular time (i.e. “down” all frequency rows at a particular time). For a “zero DM” timeseries, $i = 1$, and it is often used to identify RFI in pulsar data.

Each of the de-dispersed timeseries are then searched for pulses with amplitudes above a signal-to-noise (S/N) threshold. The mean, variance, and standard deviation of the timeseries are first computed. For a timeseries $x(t) = x_1, x_2, \dots, x_N$, where N is the number of samples in the timeseries, the mean is

$$\mu = \frac{1}{N} \sum_{i=1}^N x_i \quad (2.28)$$

and the variance is

$$\sigma^2 = \frac{1}{N} \sum_{i=1}^N (x_i - \mu)^2. \quad (2.29)$$

The standard deviation is simply the square root of the variance. The signal-to-noise ratio for a sample in the timeseries is then given by

$$\left(\frac{S}{N}\right)_i = \frac{(x_i - \mu)}{\sigma}. \quad (2.30)$$

The term, $\Delta t_{\Delta\nu}$, in equation 2.24 is as a result of the Fourier relation between time resolution and frequency sampling. The use of finite sized frequency channels yields a temporal smearing given by Cordes and McLaughlin (2003) as

$$\Delta t_{\Delta\nu} \sim (\Delta\nu)^{-1} = (\Delta\nu_{\text{MHz}})^{-1} \mu s. \quad (2.31)$$

The last term, τ_s , in equation 2.24 is the broadening of the pulse due to multipath scattering in the interstellar medium discussed in § 2.1.6. This effect is highly dependent on direction, distance as well as the frequency of observation, and may be estimated as a statistical function of DM as given by Cordes and Lazio (2002)

$$\log\tau_s = -3.72 + 0.411 \log\text{DM} + 0.937 (\log\text{DM})^2 - 4.4 \log\nu_{\text{GHz}} \mu s. \quad (2.32)$$

Chapter 3

Simultaneous Observations of Giant Pulses from the Crab Pulsar, with the MWA and the Parkes Radio Telescope

This Chapter has been published in *The Astrophysical Journal*, 809 (1), 51, as an article entitled ‘Simultaneous Observations of Giant Pulses from the Crab Pulsar, with the Murchison Widefield Array and Parkes Radio Telescope: Implications for the Giant Pulse Emission Mechanism’ by Oronsaye, S. I., S. M. Ord, N. D. R. Bhat, et al. (2015).

3.1 Introduction

The Crab pulsar (PSR B0531+21) was first revealed by its exceptionally bright pulses (Staelin and Reifenstein, 1968). These so-called “giant pulses” are short duration (ranging from a few ns to a few μ s) radio bursts, occurring only at the main-pulse (MP) or the inter-pulse (IP) phases of the pulsar rotation (Hankins et al., 2003; Hankins and Eilek, 2007; Bhat et al., 2008; Karuppusamy et al., 2012). The giant pulse amplitudes and energies typically exceed those of regular pulses by two to four orders of magnitude. While the pulse energy distribution of normal pulses follows an exponential or log-normal distribution (Burke-Spolaor et al., 2012), giant pulses instead were originally observed to obey a power-law (Argyle and Gower, 1972; Hesse and Wielebinski, 1974; Ritchings, 1976) suggesting that they are created by a different mechanism. However, subsequent

observations (Cordes et al., 2004) indicate that this power-law interpretation is an oversimplification only valid over small separations in radio frequency.

The intrinsic properties of giant pulses are often obfuscated by interstellar scintillation and scattering. For instance, observations at low frequencies are significantly affected by pulse broadening that arises from multi-path scattering in the interstellar medium (ISM; Bhat et al., 2007; Stappers et al., 2011; Ellingson et al., 2013). Other than the well-known Crab, giant pulse emission has also been observed from the LMC pulsar PSR B0540-69 (J0540-6919), and a number of millisecond pulsars including PSR B1937+21 (J1939+2134) (Wolszczan et al., 1984; Romani and Johnston, 2001; Knight et al., 2006). Large amplitude pulses of millisecond widths have also been observed in some long-period pulsars (Ershov and Kuzmin, 2005).

In the case of the Crab, giant-pulse emission is seen over a broad range of radio frequencies, from a few MHz to a few GHz. However, the physics governing the emission mechanism is still not well understood (Cordes et al., 2004; Bilous et al., 2011). Inferred brightness temperatures are of the order of 10^{30-32} K even when observations are affected by scattering or instrumental broadening, reaching up to $\sim 10^{41}$ K in observations made at ultra-high time resolutions (i.e. sub-ns) (Hankins et al., 2003; Kostyuk et al., 2003; Cordes et al., 2004; Hankins and Eilek, 2007; Bhat et al., 2008).

The short duration of each giant pulse implies broadband emission as inferred from **the** Heisenberg-Gabor limit (Gabor, 1946). Simultaneous observations of the Crab pulsar at widely separated frequencies have been employed to investigate the validity of this assumption. Comella et al. (1969) first reported 50% correlation of giant pulses detected at 74 and 111 MHz. Different degrees of correlation have since been observed from as low as 3% to as high as 70% (Sallmen et al., 1999; Popov et al., 2006; Bhat et al., 2008; Mickaliger et al., 2012).

In order to investigate how correlated giant pulses are across wide frequency separations, we have performed an experiment using the Murchison Widefield Array (MWA) and the Parkes radio telescope. We report observations performed simultaneously with the MWA, at a frequency of 193 MHz (15 MHz bandwidth) and the Parkes radio telescope, at a frequency of 1382 MHz (340 MHz bandwidth). The MWA is a low frequency (80-300 MHz) interferometric array of 128 aperture array tiles designed for the detection of the redshifted neutral hydrogen 21-cm signal from the Epoch of Reionization, Galactic and extragalactic surveys, Solar, heliospheric and ionospheric studies, as well as transient and pulsar studies (Lonsdale et al., 2009; Bowman et al., 2013; Tingay et al., 2013). The MWA

entered into its full operational phase in mid 2013.

In this chapter, we independently determine the time-of-arrival of pulses for each instrument. Twenty three coincident giant pulses were detected. We compare our results to those in the literature, determine an intrinsic giant pulse spectral index distribution via a Monte Carlo analysis, and discuss the constraints we can place on giant pulse emission mechanisms.

3.2 Observations

3.2.1 Parkes Observations

The observations presented here were made on 23 September 2013 with the 20-cm multibeam receiver system on the Parkes radio telescope. These data were recorded with a digital backend in use for the ongoing High Time Resolution Universe survey, the Berkeley-Parkes Swinburne Recorder (BPSR; Keith et al., 2010), from UTC 20^h12^m50^s to UTC 21^h02^m10^s, with a break of 245 s to allow for system calibration (from UTC 20^h39^m05^s to UTC 20^h43^m10^s). The data were recorded over a bandwidth of 340 MHz centered at 1382 MHz at each of the two linear polarisations. The polyphase filters implemented on the FPGA in the BPSR channelize the digitized data into 1024 channels with a spectral resolution of 390 kHz. The individual channels were subsequently detected and summed over both polarizations and 25 samples to yield a 64 μ s resolution time series. See Table 3.1 for a summary of the observation parameters.

3.2.2 MWA Observations

The MWA observations presented here were recorded from UTC 20^h11^m08^s to UTC 20^h55^m06^s, using the MWA Voltage Capture System (VCS). The details of the VCS are presented in Tremblay et al. (2015).

We used the VCS to record complex voltages in 10 kHz channels at the Nyquist-Shannon rate, resulting in one complex voltage sample every **100 μ s**. The 10 kHz channels were arranged in 12 groups of 128 channels (each group representing a 1.28 MHz sub-band in the MWA system). From each 1.28 MHz sub-band, the central 88 channels were recorded owing to a limitation in our data recording during the commissioning of this observing mode. Voltages for both linear polarizations were recorded for 15.36 MHz (half the maximum bandwidth of the MWA system) centered at 192.64 MHz for all 128 tiles. See Table 3.1 for

Table 3.1: Observation parameters.

Parameters	MWA	Parkes
T_{sys} (K)	268	23
Gain (K Jy ⁻¹)	0.012 ^a	0.74
HPBW	24°	14'
Center Frequency (MHz)	192.64	1382.00
Bandwidth (MHz)	15.36	340.00
^b Time resolution (μs)	400	128
Number of detected pulses	55	2075
Average pulse rate (pulses/minute)	1.25	42.35

^aThe net Gain is ~ 0.042 K Jy⁻¹ for zenith pointing.

^bResolution of the timeseries giant pulse search was performed on.

a summary of the observation parameters.

3.3 Data Analysis and Results

3.3.1 Parkes Data Analysis

The data were searched in real-time for giant pulses using the HEIMDALL single pulse processing software¹, following procedures similar to those described in Burke-Spolaor et al. (2011). The giant pulse topocentric arrival times were recorded, along with other properties including signal to noise ratio, dispersion measure (DM), and matched filter width (**128** μs). A total of 2075 giant pulses above a signal to noise ratio (S/N) of 6.5 were detected. This detection threshold is a default setting by the instrument’s hardware due to the RFI environment.

Assuming the noise is Gaussian, we can estimate the number of false positives above the detection threshold using the Gaussian distribution function. The probability, P_n that we obtain an event above a threshold of $n\sigma$ is

$$P_n(x > n\sigma) = \int_{\mu+n\sigma}^{\infty} P(x)dx = \frac{1}{2}\text{erfc}\left[\frac{n}{\sqrt{2}}\right], \quad (3.1)$$

where σ is the rms fluctuations in the noise, μ is the mean noise level, and erfc

¹<http://sourceforge.net/projects/heimdall-astro>

is the complementary error function. The number of false positives N , above a threshold of $n\sigma$ is the product of the probability P_n , of obtaining a false positive above this threshold from one sample, and the total number of samples. Above 6.5σ , we estimated the number of false positives to be significantly less than one. Throughout the Parkes observations, we detected 3 events above 6.5σ in the off-pulse region. Which is higher than predicted, and probably indicative of radio frequency interference. However the on-pulse region, to which we restrict our detections, is less than 1 percent of this extent. We therefore do not expect any false positive detections in our data set.

The flux density, S of each giant pulse was calculated using the radiometer equation

$$S = \frac{(S/N)S_{sys}}{\sqrt{n_p t_{int} \Delta\nu}}, \quad (3.2)$$

where S_{sys} is the system equivalent flux density, $n_p = 2$ is the number of polarisations, $t_{int} = 128 \mu\text{s}$ is integration time, and $\Delta\nu = 340 \text{ MHz}$ is the observing bandwidth. Given that the size of the radio telescope beam (See Table 3.1) is only about three times larger than the characteristic size of the Crab Nebula ($\sim 5.5'$), the S_{sys} is dominated by the flux contribution from the Nebula. Following Bietenholz et al. (1997), the flux contribution is $S_{CN} = 955\nu^{-0.27} \text{ Jy}$. The total system equivalent flux density is therefore

$$S_{sys} = S_{syso} + S_{CN}, \quad (3.3)$$

where $S_{syso} = T_{syso}/G$ is the system equivalent flux density in the absence of the Crab Nebula, T_{syso} is the system temperature in the absence of the Nebula, and G is the gain of the telescope. This translates to a S_{sys} of 906 Jy.

Although pulsars are in general stable rotators, the Crab pulsar is not. It is a young pulsar and subject to abrupt changes in rotation rate (Lyne et al., 1993). Therefore a precise ephemeris, valid for the day of observation, had to be obtained in order to measure the rotation rate of the pulsar. In this case we used the time of arrival of the giant pulses at Parkes, all of which are unresolved, as markers of the pulsar rotation rate. The pulsar timing package TEMPO2 (Hobbs et al., 2006) was used to obtain a pulsar folding ephemeris for the observations.

3.3.2 MWA Data Analysis

3.3.2.1 Incoherent Beamforming and De-dispersion

Post-observation, the voltage samples for the two polarizations across the 128 tiles were squared to form powers and then summed in each 10 kHz channel for each $100 \mu\text{s}$ time step to form an incoherent beam. The sum was inverse-variance weighted to maximise the signal to noise. This incoherent summing of the MWA tiles yields a large field-of-view, 24° (each tile beam $\propto \lambda/d$, where λ is the observing wavelength, and d is the size of the tile), but a sensitivity that is \sqrt{N} times smaller than that achievable by coherent combination of the full array, where N is the number of tiles.

The incoherent beam was then converted into the PSRFITS data format (Hotan et al., 2004). The files were then processed using the pulsar exploration and search toolkit (PRESTO; Ransom 2001). We averaged in time to $400 \mu\text{s}$, de-dispersed the data, and generated a time series at the nominal DM of the Crab pulsar (56.70 pc cm^{-3}).

Figure 3.1 shows the brightest giant pulse from our observations, where the scattering tail extends to $\sim 50 \text{ ms}$, which is longer than the pulsar rotation period of 33 ms . Further analysis of scattering and comparison with the previously published observations are discussed in § 3.3.4.

3.3.2.2 Measuring the Properties of Giant Pulses

The Crab Nebula is an extended radio source, measuring about $5.5'$ in diameter, with a flux density of $\sim 955\nu^{-0.27} \text{ Jy}$ (Bietenholz et al., 1997), where ν is the frequency in GHz. In our case, the Nebula occupies only a tiny fraction ($\sim 0.2\%$) of the telescope beam. The nominal sky temperature at our observing frequency and for our pointing was evaluated from the global sky model (de Oliveira-Costa et al., 2008) to be 243 K ; this value explicitly includes the contribution from the Crab Nebula. At 200 MHz , our receiver temperature is 25 K (Tingay et al., 2013). The incoherent gain (G_{inco}) of the instrument is given by the expression

$$G_{inco} = \frac{\frac{\lambda^2}{2\pi}(16\sqrt{N})}{2k} \sin^2\theta, \quad (3.4)$$

where λ is the observing wavelength, N is the number of antenna tiles, k is the Boltzmann's constant, and θ is the elevation angle. For a nominal G_{inco} of 0.012 K Jy^{-1} at the Crab's elevation (41.42°), the system equivalent flux density ($S_{\text{sys}} = T_{\text{sys}}/G_{inco}$) of our telescope is $\sim 22000 \text{ Jy}$.

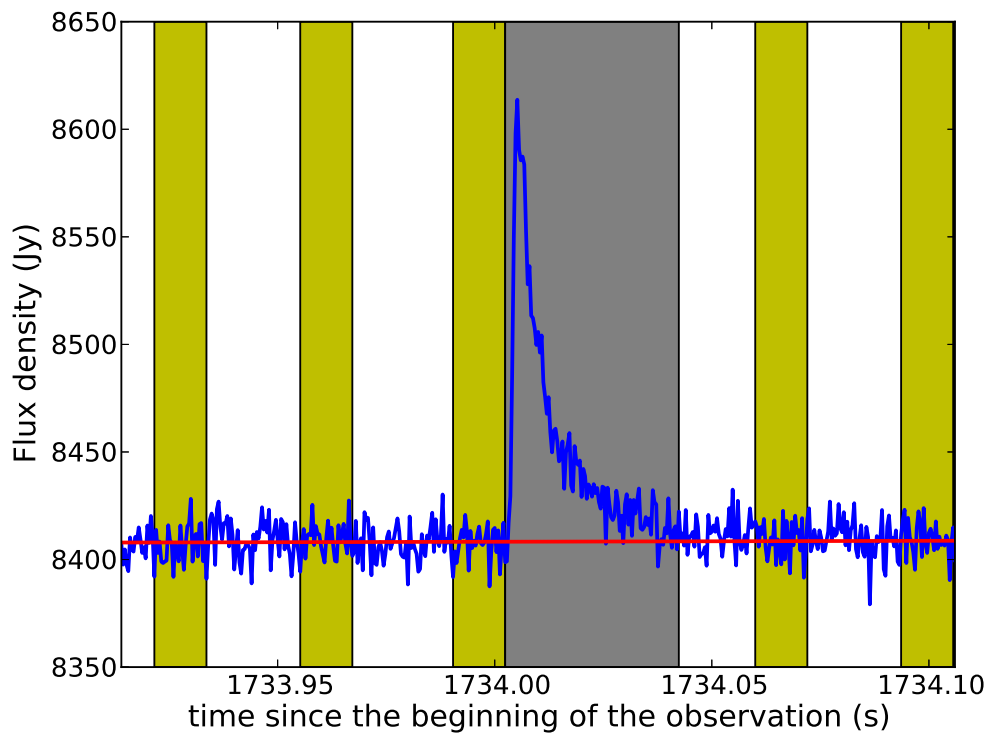


Figure 3.1: Dedispersed time series for the strongest giant pulse in the MWA data. The yellow (lighter) portions were used to estimate the off-pulse baseline shown by the red line. **The off-pulse baseline was determined by the method of least square with a chi-square value of 3.8.** The gray (darker) area is the region that was integrated over to measure the total pulse energy. The plot spans 180 ms and has a time resolution of $400\mu\text{s}$.

The phase of each giant pulse was determined from the arrival times of the giant pulses and the pulsar ephemeris derived from the Parkes data (see § 3.3.1). We find giant pulses only at the MP and IP phases of the pulsar rotation, consistent with earlier results (Lundgren et al., 1995; Cordes et al., 2004; Soglasnov et al., 2004; Popov et al., 2006; Bhat et al., 2008; Karuppusamy et al., 2012).

The total flux density was measured by integrating over a 40 ms window for every pulse period, **beginning just before the leading edge of the pulse**. The integration window was determined by estimating the timescale over which the amplitude of the brightest pulse fell below the 1σ noise level of the baseline. This corresponded to 40 ms, approximately 6 e-folds of the estimated scattering timescale (see § 3.3.4). The baseline was determined by a linear least square fit to the off-pulse power across a series of five windows, each 12 ms wide, distributed before and after every pulse period in the timeseries (see Figure 1).

The resulting distribution of integrated flux density is consistent with the noise distribution of the integrated timeseries, because the number of giant pulses are few compared to the number of the observed periods ($\sim 80,000$ periods). The root-mean-square noise variation (rms) was determined by estimating the standard deviation of the distribution, and the S/N was subsequently determined. The integrated flux density of each giant pulse was then calibrated using equation 3.2.

In order to determine the number of false positives our pipeline generated, we simulated a noise dominated timeseries using the mean, and the variance of our data. We then subjected the simulated timeseries to the same analysis described. The number of false positives generated by this experiment above 3.5σ was two, a false positive rate we deemed acceptable where σ is the rms of the distribution. At this threshold, our minimum detectable flux density is ~ 70 Jy.

In the actual analysis of the observed data-set, above a threshold of 3.5σ , 45 giant pulses were recovered from the MP phases and 10 giant pulses were recovered from the IP phase. The majority of giant pulses, 84%, occur at the phase of the MP and the remaining 16% occur at the IP phase. This is in agreement with previous results published in the literature (Popov and Stappers, 2007; Bhat et al., 2008; Mickaliger et al., 2012).

3.3.3 The Giant Pulse Fluence Distribution

We now make the assumption, common in the literature, that the measured giant pulse energy is drawn from a power-law distribution, and attempt to determine the power-law index. We are in fact measuring the time integrated flux

density, or *fluence*, which is a quantity directly proportional to pulse energy received by a given collecting area and will use this quantity in our analysis.

A power-law index is often determined geometrically by a least squares fit of a straight line to logarithmically binned data (Bhat et al., 2008). This is not the most reliable method of estimating this parameter and is generally considered to generate biased values of the power-law index (Goldstein et al., 2004). In order to remove subjectivity and to limit bias we have chosen to use Hill’s estimator as a maximum likelihood estimator (MLE) of the index of the underlying fluence distribution. With n measurements of fluence, x_i , we determine the index, $\hat{\beta}$, of the underlying power-law distribution via:

$$\hat{\beta} = 1 + n \left(\sum_{i=1}^n \ln \frac{x_i}{x_{\min}} \right)^{-1}. \quad (3.5)$$

Hill’s estimator is sensitive to the determination of the power-law cut-off (x_{\min}), but geometric methods are also very sensitive to this and often the power-law cut-off is chosen somewhat subjectively. To limit this subjectivity we have chosen to follow a method of minimising the Kolmogorov-Smirnov distance between the fitted distribution and the measured distribution, as a function of the power-law cut-off, in order to determine the optimum value of x_{\min} . The standard error in the power-law index estimate, $\hat{\sigma} = (\hat{\beta} - 1)/\sqrt{n}$, was also determined analytically. Using this method we determined the power-law index of fluence distribution detected at the MWA to be -3.35 ± 0.35 .

The cumulative distribution (CDF) of the main-pulse phase giant pulses detected with the MWA is shown in Figure 3.2. The slope of the CDF of giant pulse fluences can also be used to determine the index of the underlying power-law distribution, although error prone, this method is often used in the pulsar literature (Popov and Stappers, 2007; Karuppusamy et al., 2010). The gradient is equal to $1 + \hat{\beta}$, but as the index is formed from a least squares fit of a straight line to logarithmic bins that are not independent, the error in the index is difficult to determine. In this case we find a gradient of -2.22 which would predict a $\hat{\beta}$ of -3.22 , consistent with our MLE analysis.

We applied the MLE method to our observations of the Parkes pulses (at 1382 MHz) and obtained an index of -2.85 ± 0.05 , which is consistent with that obtained by Karuppusamy et al. (2010); it is slightly steeper than the -2.33 ± 0.14 and 2.20 ± 0.18 at 1300 and 1470 MHz reported by Bhat et al. (2008), but is within the range of -2.1 ± 0.3 to -3.1 ± 0.2 as given by Mickaliger et al. (2012).

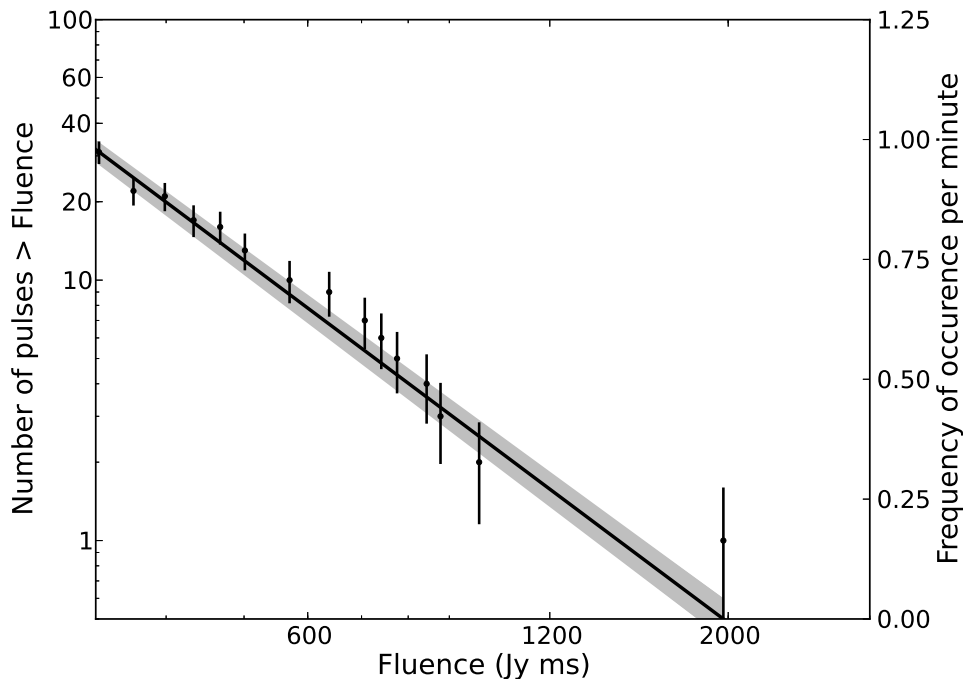


Figure 3.2: The cumulative distribution of the MP giant pulses detected with the MWA. Also shown here is MLE power-law fit to the distribution, with a power-law index of -2.35 ± 0.35 . The shaded region is a ± 0.35 error in the power-law index.

3.3.4 Pulse Shape and Scattering

Scattered pulse shapes are typically modelled as convolutions of intrinsic pulse shapes with the broadening functions characterising multi-path scattering through the ISM and the instrumental response. By applying a deconvolution method as described in Bhat et al. (2003) to the pulse shown in Figure 3.1, we estimate a pulse broadening time, $\tau_d \sim 6.1 \pm 1.5$ ms, which can be compared to $\sim 0.67 \pm 0.10$ ms reported previously by Bhat et al. (2007) from observations made with an early prototype built for the MWA. Our estimated τ_d is thus nearly $10 \times$ larger than that measured earlier with the 3-tile prototype MWA and $5 \times$ larger than the extrapolated value from the observations of Karuppusamy et al. (2012) at a nearby frequency of 174 MHz. However, it is a factor of two less than that expected based on recent observations by Ellingson et al. (2013) with the LWA and their re-derived frequency scaling index, $\tau_d \propto \nu^{-3.7}$. As highlighted by Bhat et al. (2007) and Ellingson et al. (2013), the Crab pulsar is well known for

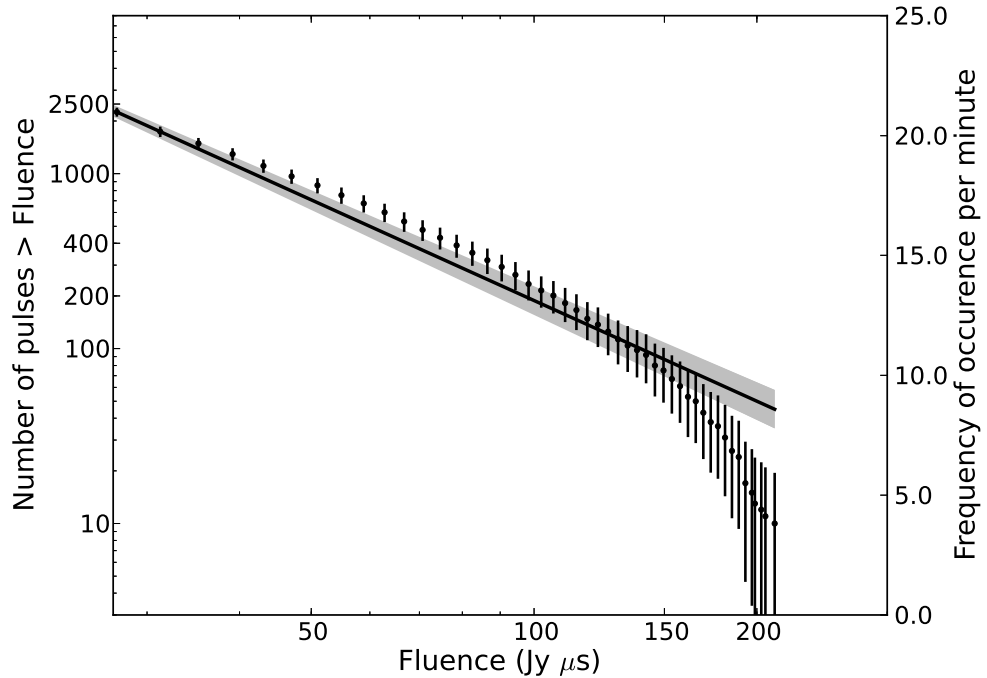


Figure 3.3: Distribution of the MP giant pulses detected with the Parkes radio telescope. The plotted errors of fit might be underestimated. The solid line is the MLE power-law fit to the data with a power-law index of -2.85 ± 0.05 . The shaded region is a ± 0.05 error in the power-law index.

highly variable scattering, on timescales of the order of months to years, which can be attributed to ionised clouds or filaments within the nebula crossing the line of sight.

3.3.5 Coincidences in the MWA and Parkes Giant Pulse Arrival Times

A search for coincident giant pulse arrival times was performed. Of the 55 giant pulses that were detected with the MWA, 45 were detected during the period of simultaneous observations with the Parkes radio telescope, and 1681 giant pulses were detected at Parkes. Due to the dispersive nature of the interstellar medium, the high frequency component of broadband giant pulses will arrive at the Parkes observing frequency earlier than at the MWA frequency. **The MWA data is dominated by scattering (see § 3.3.4), determining a precise DM will be difficult and may be biased, as a result, we used the Jodrell**

Bank monthly ephemeris² (Lyne et al., 1993) which provides a DM of $56.774 \pm 0.005 \text{ pc cm}^{-3}$. The relative delay in pulse arrival time for this DM is therefore $5.746 \pm 0.008 \text{ s}$ between 1382.00 and 200.32 MHz (upper band edge for the MWA).

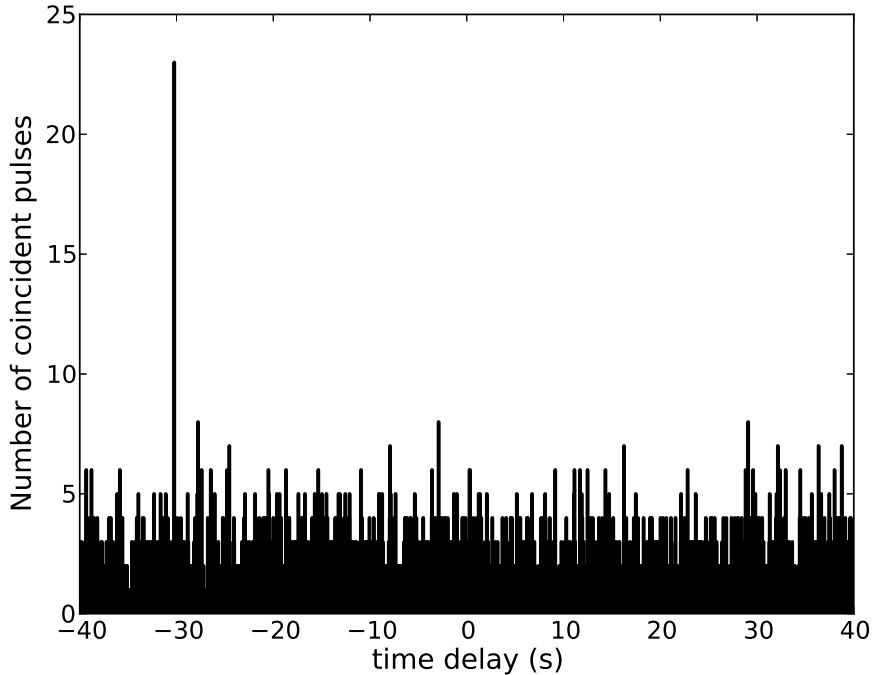


Figure 3.4: A plot showing the search for coincident giant pulses in the MWA and the Parkes arrival times. We identify a 36.000 s clock error in the timestamps of the recording machine used at Parkes at the time of this observation (see text). We used the arrival times of the Parkes giant pulses to search for coincidence in the MWA pulse arrival times. As can be seen in the figure, we found strong peak corresponding to 23 pulses at -30.248 s . Correcting for the 36 s offset yields 5.75 s which corresponds to the time delay between the arrival times of the MWA and the Parkes pulses.

In order to search for coincident giant pulses observed at the MWA and the Parkes radio telescope, we performed a correlation analysis between the arrival times of the MWA and the Parkes giant pulses. This analysis revealed that the backend used for data recording at Parkes had a clock error of 36.000 s in the timestamps at the time of this observation³. As a result, the timestamps for the

²<http://www.jb.man.ac.uk/pulsar/crab.html>

³The server that was time-stamping BPSR observations had a problem with it's

Parkes pulses are ahead of UTC by 36.000 s. We found 23 coincident giant pulses at -30.248 s (see Figure 3.4). Correcting for the 36.000 s error yields 5.752 s delay (MWA trailing Parkes), consistent with the dispersive time delay between the arrival times of the MWA and the Parkes giant pulses.

The 23 coincident giant pulses detected at the MWA and Parkes implies 51% correlation, since 45 giant pulses were detected with the MWA during the common observing period. Our observations are therefore consistent with previous observations (e. g. Comella et al. (1969); Sallmen et al. (1999)), see § 3.4.2 for comparison.

3.3.6 Spectral Indices of Coincident Giant Pulses

The spectral indices of the giant pulses detected simultaneously at the MWA and the Parkes radio telescope were estimated using $S_\nu \propto \nu^\alpha$, where S_ν is the fluence of the giant pulse at frequency ν and α is the spectral index. The values derived here are presented in Figure 3.5, and display a range between -3.6 and -4.9 , which are steeper than the limits obtained by Karuppusamy et al. (2010), -1.44 ± 3.3 and -0.6 ± 3.5 for the MP and IP, respectively. Our limits are consistent with Sallmen et al. (1999), based on their simultaneous detections of 29 giant pulses at 610 and 1400 MHz. Sallmen et al. (1999) constrain the spectral index spread to be within the range $-2.2 > \alpha > -4.9$. The difference in the lower limit is discussed in §3.4.2.

3.4 Discussion

3.4.1 The Fluence Distribution

3.4.1.1 Comparison with the Literature

We detected a total of 55 giant pulses at the MWA, and estimate a power-law index of $\beta = -3.35 \pm 0.35$ for their pulse fluence distribution, using the maximum likelihood estimator method. For the Parkes data, in which we detected a total of 2075 pulses, application of this method yields $\beta = -2.85 \pm 0.05$. In the published literature, however, the reported power-law index for the giant pulse fluence distribution covers a wide range. Different distributions have been considered, including pulse peak amplitude, average flux density, and pulse fluence, NTP service during the observing period, and because this backend is not used for pulsar timing, the error was not detected until this analysis

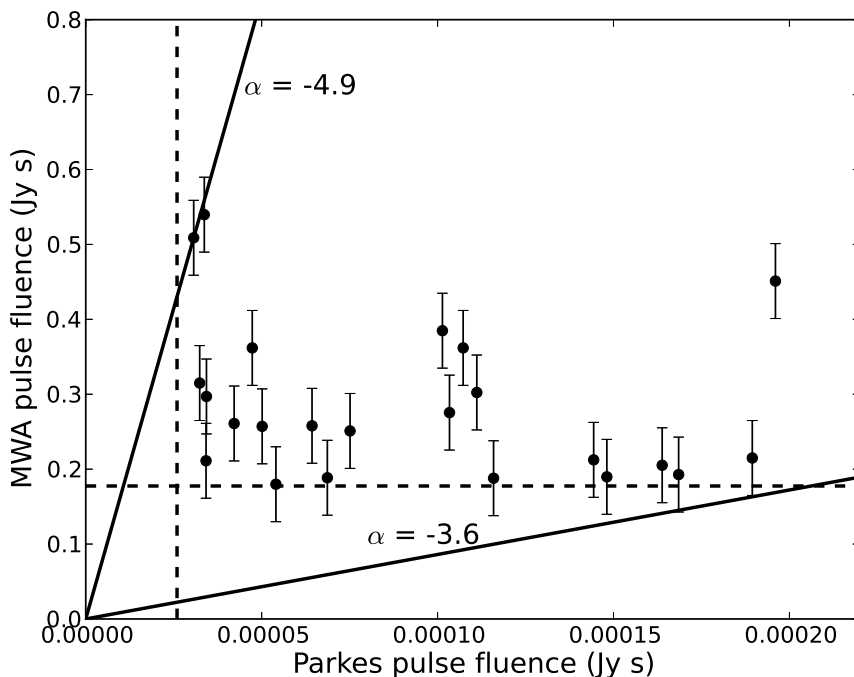


Figure 3.5: The fluence in Jy-s of the coincident giant pulses detected with the MWA and Parkes. The error bars indicate the uncertainty in the sky temperature measurement for the MWA (which translate to ± 0.08 Jy s in this case), which is negligible at the Parkes frequency. The vertical and the horizontal dash lines are the detection thresholds for the MWA and the Parkes observations. The solid lines are spectral indices $\alpha = -3.6$ and $\alpha = -4.9$. This figure is similar to Figure 7 of Sallmen et al. (1999), in which they constrained the spectral indices within the range of $-2.2 > \alpha > -4.9$.

although a degree of proportionality exists between these different measures direct comparison is difficult. Our power-law index of -3.35 ± 0.35 for the pulse fluence distribution at 193 MHz is steeper than the range from -1.51 ± 0.05 to -2.39 ± 0.12 that was reported by Karuppusamy et al. (2012) at 110-180 MHz. **This can be attributed to the increased scattering measure between the two observing epochs, resulting in less sensitivity to weak pulses, and steep power-law index. However, within a 2σ error, the power-law indices for both observations are consistent.** Cordes et al. (2004) estimate -2.3 for the index of giant pulse peak amplitude distribution at the main-pulse phase; their observation was made at 430 MHz and they note that the distribution only obeys a power-law for a limited range of pulse flux density. However

our estimated β is in good agreement with a value of -3.46 ± 0.04 determined by Lundgren et al. (1995) for the average flux density distribution from their extensive observations at 800 MHz.

We propose that the majority of the published variation in power-law indices arises from the underlying distribution not following a simple power law over a large range of fluences and also from inconsistencies in the subjective determination of the power-law cut-off. The MLE based method that we used here has the virtue of removing some subjectivity from this analysis.

3.4.1.2 Effects of Scintillation

Observed radio pulses are often influenced by interstellar scintillation (Lyne and Rickett, 1968; Cordes et al., 2004). Under unfavorable conditions, this effect can strongly modulate the observed fluence of giant pulses. In our case, this effect may arise from refractive modulation since short-term diffractive modulations will be highly quenched over our observing duration and bandwidth, at both MWA and Parkes frequencies. Cordes et al. (2004) report $\Delta\nu_d < 0.8$ MHz and $\Delta t_d = 25 \pm 5$ secs at 1.48 GHz; where $\Delta\nu_d$ and Δt_d are the diffractive scintillation bandwidth and timescale respectively. At the MWA frequency these will be orders of magnitude smaller and are therefore no longer relevant. As for refractive modulation, Rickett (1990) report a time scale of $\sim 83 \pm 50$ days at 196 MHz and $\sim 6 - 12$ days at their highest frequency of 610 MHz. Even if we consider a factor of two variability as a possible worst case scenario at our frequencies, it may not still significantly alter our spectral index analysis and conclusions.

3.4.2 Correlated Detections and Intrinsic Giant Pulse Spectral Index Distribution

Simultaneous observations of the Crab pulsar at multiple frequencies have been reported in the literature. This includes the work of Comella et al. (1969) from early pulsar observations, at 74 and 111 MHz, to observations that reach frequencies as high as 8.9 GHz (Mickaliger et al., 2012). The level of correlation presented does vary. Observations by Ellingson et al. (2013) using the LWA with 4 x 16 MHz observing bands spread from 28 MHz to 76 MHz contain 33 giant pulse detections, only one of which was observed in all 4 bands, but almost all were observed in at least 2. Based on observations with the Green Bank 25-metre telescope and the Very Large Array, Sallmen et al. (1999) reported the detection

of 70% of giant pulses seen simultaneously at both 600 and 1400 MHz. Popov et al. (2006) report 27% simultaneous detections at their observing frequencies of 23 and 600 MHz but only 16% at 111 and 600 MHz. Bhat et al. (2008) found 70% correlation between the the giant pulses observed at 1300 MHz and 1470 MHz, similar to the result obtained by Sallmen et al. (1999). The observations of Mickaliger et al. (2012) at larger frequency separations show a significantly smaller fraction, 3% to 5% between 1.2 GHz and 8.9 GHz for the MP and IP giant pulses, respectively.

Our observations display a correlation of 51% between the pulses detected at Parkes and at the MWA, but the range of spectral indices displayed by the detected pulses (-3.6 to -4.9) is considerably narrower than reported by **Sallmen et al. (1999)**. It is likely that the paucity of pulses with spectral indices shallower than -3.6 is due to the sensitivity limit of the MWA telescope and consequently that the intrinsic degree of correlation is likely to be much higher than 50%. We hypothesise that the apparent reduction of correlation is due to the wide range of spectral index displayed by the giant pulses, coupled with the sensitivity limits of the two telescopes.

In order to investigate this further, a Monte Carlo simulation was conducted using the Parkes data as the known distribution of giant pulse fluence. Attempts were made to predict the number of pulses detected coincidentally at the MWA and their spectral index distribution using a two sample Komolgorov-Smirnov (KS) test.

We first determined the most likely intrinsic distribution of giant pulse spectral indices. As reported by both Sallmen et al. (1999) and Karuppusamy et al. (2010), the scatter in individual giant pulse spectral indices is large. The hypothesis that the intrinsic giant pulse spectral indices could have been drawn from a uniform distribution between -2.2 and -4.9 was immediately discounted; it reproduced the range of detected spectral indices (-3.6 to -4.9) however it over-estimated the number of coincident detections by a factor of 20. The broad distributions favoured by Karuppusamy et al. (2010) were also discounted by this analysis, as although they could reproduce the number of coincident detections, the distribution of predicted spectral indices were not compatible with the observations. A normal distribution of spectral indices was a much more successful hypothesis. It simultaneously satisfied the constraints of the detected spectral indices and the number of detections. We chose to investigate this further and determine the parameters of such a distribution that would best fit our data. We allowed the mean of the distribution to vary between -2.0 and -3.6 , but held

the standard deviation to 0.6, consistent with the observations of Sallmen et al. (1999), and investigated the predicted number of coincident detections and their spectral indices.

For each of the Parkes giant-pulse detections we randomly drew a spectral index from the distribution under test and predicted the fluence of the pulse at the MWA. If the predicted fluence was above the MWA detection threshold we registered a detection and the spectral index that was associated with it. This was repeated for every pulse. Each trial distribution was tested 1000 times and the results combined.

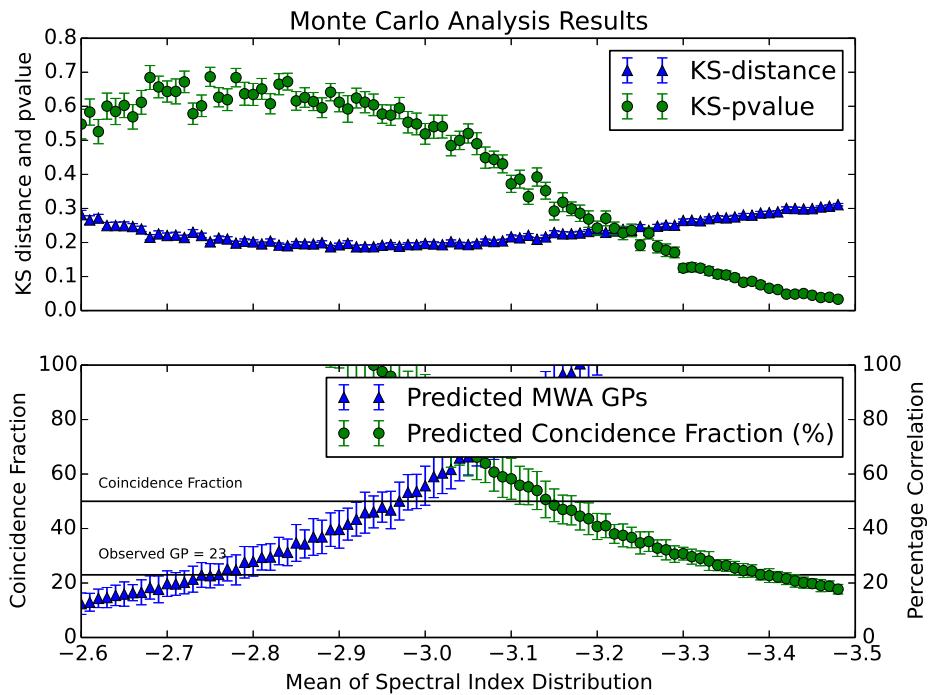


Figure 3.6: The results of the Monte Carlo analysis to determine the best fit intrinsic mean spectral index of the giant pulses. The three constraints, number of coincident detections (23), observed correlation factor (50%) and distribution of observed spectral indices cannot be satisfied by the same input distribution.

As we have recorded observations at both telescopes we can reverse this analysis and use the MWA detected pulse and spectral index distribution to predict the coincident pulses at Parkes, and thereby determine the percentage of correlated pulses. We are only observing the steep spectrum end of the giant pulse distribution at the MWA, as evidenced by inspecting the measured spectral index distribution. We can infer that some pulses detected at the MWA will have a

combination of fluence and steep spectral index that would bring them below the detection threshold at Parkes. This feature would be the reason for the less than 100% correlation in pulse detections.

In Figure 3.6, the lower panel shows the predicted number of GPs detected at the MWA for each trial spectral index distribution as triangles and the percentage of coincident GPs between the MWA and Parkes. There are also two lines representing the observed number of GPs and the observed coincidence fraction. To satisfy the observations, a trial spectral index distribution should simultaneously satisfy both these constraints. The error bar is the standard deviation about this average prediction. The upper panel shows the results, both distance and p-value, for the two-sample KS test between the predicted spectral index distribution of the coincident pulses and the measured distribution; the error bar is the standard error. The p-value can be interpreted as the probability that the distance is as large as observed, if the null hypothesis is true (being that both populations are drawn from the same distribution). The null hypothesis is typically not rejected if the distance is below a critical value for the two distributions under test. These results show that, for those distributions with a significant p-value, we cannot reject the null hypothesis and that the observed and simulated spectral index distributions are consistent with same parent distribution.

Without any fine tuning, the simulations predict the following:

- The detected spectral index distribution at the MWA is best replicated by an input spectral index distribution of -2.85 with a standard deviation of 0.6
- The observed 50% correlation is best replicated by a spectral index distribution closer to -3.15
- Both these input distributions over-estimate the number of coincident pulses by a factor of 2 to 3

3.4.2.1 Fine Tuning the Analysis

The simplest, and most reasonable fine tuning is to reflect the lack of flux density calibration and assume some less-than-theoretical detection sensitivity. We can align the number of MWA detections with the best fit spectral index distribution, using the MWA detection threshold as a fit parameter. Raising the MWA detection threshold by 10% generates a best fit mean spectral index distribution of -2.8, and correctly predicts the number of MWA detections. However it cannot

simultaneously replicate the correlation percentage, which is now reproduced by invoking a source spectral index distribution with a mean of -3.2.

Altering the width of the model spectral index distribution does not provide the required fine tuning. The width of 1.2 is wide enough that it produces features similar to that generated by a uniform distribution of spectral indices. In that we can reproduce the number of detections at the MWA but the distribution of observed spectral indices differs too greatly. In the case of the narrow distribution, it is difficult to reproduce the number of detections unless we adjust the relative sensitivity of the telescopes beyond what would be considered reasonable.

A distribution that satisfies the constraints in predicting the Parkes pulse survival to the MWA observing frequency is therefore still inconsistent with the distribution that satisfies the degree of correlation. A more sophisticated fine-tuning would be to invoke some evolution in the distribution as a function of frequency. We have found that this evolution does not have to be extreme in order to remove the inconsistency. A 5% flattening in the spectral index, on average, between the two frequencies is all that is required to match the observed pulse coincidence rate, while maintaining a spectral index distribution consistent with that observed. We obtained this estimate using the previous Monte Carlo analysis, but including an average reduction factor in the randomly drawn individual pulse spectral index when predicting the observed fluence at the MWA. We incorporated the same factor in the inverse experiment.

Incorporating this fine tuning, our observations are consistent with the hypothesis that the spectral index of giant pulses is drawn from normal distribution of standard deviation 0.6, but with a mean that displays an evolution with frequency from -3.00 at 1382 MHz, to -2.85 at 192 MHz. Note this estimation only includes the integrated effect of the evolution in spectral index, and therefore does not incorporate curvature. It would be consistent with these results if the low frequency spectral index were considerably flatter, or the high frequency steeper, than that estimated here, but that would require a rapid evolution, such as a turn-over, to be present. Figure 3.7 shows the results of the analysis including the fine tuning and we summarise the results here:

- The MWA detection threshold is 10% less sensitive than our theoretical prediction
- There is a 5% flattening in the mean of the spectral index distribution from -3.00 to -2.85 between 1382 MHz and 192 MHz, the spectral index distribution in this analysis has width of 0.6, but this has not been constrained

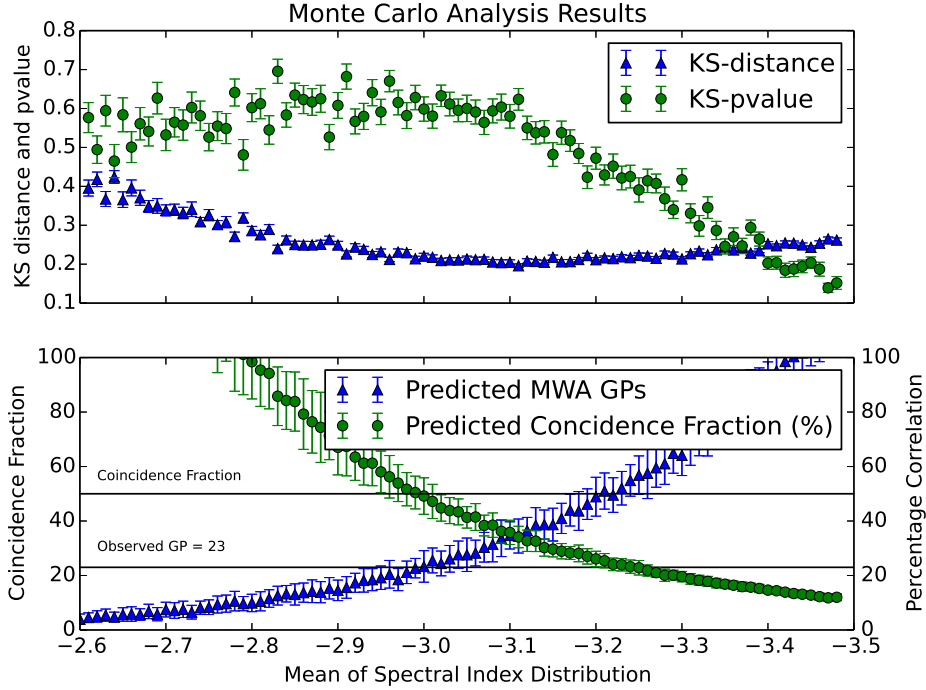


Figure 3.7: Fine tuning the Monte Carlo analysis by incorporating an overestimate of the MWA sensitivity by 10% and a mild (5%) evolution in the spectral index as a function of frequency produces an internally consistent estimate for the mean of the spectral index distribution (-3.00 at 1382 MHz, to greater than -2.85 at 192 MHz).

by the fits

- This distribution correctly predicts the number of coincident detections and the 50% correlation between the two observations

The *average* emission from pulsars typically obeys a simple power-law with a mean index of -1.4 (Bates et al., 2013). However, the MP and IP components of the Crab pulsar have much steeper spectral indices of -2.8 and -3.7 when measured between 410 and 1660 MHz (Manchester et al., 1971). A flattening in the spectra of normal pulsar emission is commonly observed and many young pulsars have been found to display complex spectra and low frequency (~ 100 MHz) spectral turn-overs (Malofeev et al., 1994; Kijak et al., 2007). The phase averaged emission from the Crab pulsar is complicated due to the multi-component structure. We are unaware of any observed flattening of MP component at lower frequencies but suspect that this is confused by the rapid

evolution of precursor. The cause of the spectral turnover in these objects is not known and experiments are complicated by the difficulty of observing complex pulse profiles at low frequencies.

3.4.3 Propagation Effects within the Nebula

Our measurements of the scattering timescale (§3.3.4) indicate that the environment of the nebula continues to affect the observations of the pulsar, as already observed by Rankin and Counselman (1973), Isaacman and Rankin (1977), Bhat et al. (2008), Kuz'min et al. (2008) and Ellingson et al. (2013). Free-free absorption within the filamentary structures, evident in observations of the Crab nebula, has already been reported by Bridle (1970) and Bietenholz et al. (1997). We now investigate whether this effect could be responsible for the modest flattening in spectral index that has been indicated by our analysis. The free-free absorption coefficient (α_ν^{ff}) in the Rayleigh-Jeans regime can be numerically approximated (in cgs units) to be:

$$\alpha_\nu^{\text{ff}} = 0.018T^{-3/2}Z^2n_en_i\nu^{-2}\bar{g}_{\text{ff}} \quad (3.6)$$

where Z is the atomic number of the absorber, n_e and n_i , are the number density per cm^{-3} of the electrons and ions respectively, and T is the temperature in K (Rybicki and Lightman, 1979). \bar{g}_{ff} is the Gaunt factor, which in this regime (the high temperature or *quantum limit*) is approximated by Gayet (1970):

$$\bar{g}_{\text{ff}} = \frac{\sqrt{3}}{\pi} \ln \left(\frac{4kT}{h\nu e^\gamma} \right), \quad (3.7)$$

where k is Boltzmann's constant, h is Planck's constant, and γ is Euler's constant. At these temperatures and frequencies the Gaunt factor is approximately 10. The optical depth τ_{ff} is given by:

$$\tau_\nu^{\text{ff}} = \int_0^{z(\text{pc})} \alpha_\nu^{\text{ff}} dz, \quad (3.8)$$

where z is the path length, and the absorption factor is subsequently calculated as $e^{-\tau^{\text{ff}}}$.

The nebula has an approximate radius of 1.7 pc and if all the observed DM ($56.70 \text{ cm}^{-3}\text{pc}$) were due to the nebula, then n_e would be $56.7/1.7$ or 33.4 cm^{-3} . Assuming the nebula is predominantly Hydrogen, $Z = 1$, $n_e = n_i = 33.4 \text{ cm}^{-3}$ at a temperature 10^4K , then at our observing frequency ($192 \times 10^6 \text{ Hz}$) the free-free absorption coefficient is $\sim 5.4 \times 10^{-23} \text{ cm}^{-1}$. This is insufficient to account for any absorption even at these very high Gaunt factors.

The ionised material is not evenly distributed, and this inhomogeneity will strongly influence the level of free-free absorption. The filamentary structures of the nebula that have been observed to display free-free absorption in spectral index maps by Bietenholz et al. (1997), have been estimated to have an electron density in excess of 200 cm^{-3} . These are arcsecond size structures, implying a size scale of 0.02 pc . Each of these filaments would contribute 1.2×10^{-4} to the optical depth and attenuate the intensity by a factor of 0.9998 , which also cannot supply the necessary absorption even if several hundred filaments intercept the line of sight. Davidson and Tucker (1970) use line intensities to estimate the filamentary n_e to be $\sim 1000 \text{ cm}^{-3}$, however each filament now contributes $\sim 10 \text{ cm}^{-3} \text{ pc}$ to the dispersion measure so only a small number of crossings are permitted, therefore these structures cannot provide the level of absorption required.

There is also evidence of very small (AU) scale filamentary structures with electron densities in excess of 10^4 cm^{-3} (Smith and Terry, 2011). If many tens of these small filaments are intercepted, they are capable of generating the few percent level absorption required. They would also not contribute more than $10 \text{ cm}^{-3} \text{ pc}$ to the pulsar dispersion measure. However it is unlikely that these structures exist in sufficient numbers to contribute at this level (Smith and Terry, 2011).

In summary it is unlikely that free-free absorption within the filamentary nebula is capable of attenuating the pulse intensity sufficiently to explain our predictions, and therefore any variation in the spectra of the giant pulses is unlikely to be propagative in nature.

3.5 Conclusion

In this chapter, we report observations performed simultaneously with the MWA, at a frequency of 193 MHz (15 MHz bandwidth) and the Parkes radio telescope, at a frequency of 1382 MHz (340 MHz bandwidth). We detected a total of 55 giant pulses at the MWA, and estimate a power-law index of $\beta = -3.35 \pm 0.35$ for their pulse fluence distribution. 23 of the pulses were detected at both the MWA and at Parkes radio telescope. These results are consistent with the spectral index of the giant pulses being drawn from normal distribution, the parameters of which are frequency dependent. The mean of the spectral index distribution varies from -3.00 to -2.85 between 1382 MHz and 192 MHz . It is unlikely that this flattening can be caused by any propagative effects within the nebula.

In this work we have proposed that the less than total correlation observed is simply a function of the spread in giant pulse spectral indices and the relative sensitivities of the two instruments, but have not proposed a mechanism by which this large range of spectral indices may be generated. Giant pulses are thought to comprise complex temporal substructures on nano-second to micro-second timescales (Hankins et al., 2003). Eilek et al. (2002) have noted that these substructures are strongly correlated at two observing frequencies with a small fractional bandwidth, and less correlated as the fractional bandwidth increases, suggesting a complex behaviour as a function of frequency, cannot be ruled out by the behaviour we see in this experiment.

The MWA's large frequency coverage and flexible system design offer unique opportunities to further investigate the wide-band properties of giant pulses. With the full-bandwidth VCS recording now feasible (Tremblay et al., 2015), it is possible to perform sensitive observations simultaneously at multiple frequencies within the 80 - 300 MHz range, by suitably spreading out the 30.72 MHz observing band across a large range in frequency. This will allow us to conduct observations that span large fractional bandwidths, with the prospects of determining the emission bandwidth and spectral nature of giant pulses at low frequencies.

Combining all the MWA tiles coherently, we will realise a factor of ~ 11 improvement in sensitivity over this experiment. With an increase in gain by this factor, as well as increase in bandwidth by a factor of 2, the instrument is expected to detect about 10,000 pulses in a one hour observation. This also implies that about 600 pulses are expected to be detectable in a 1.28 MHz subband of the MWA. This increase in sensitivity means that a higher percentage of coincident pulses will be detectable when observing in the coherent mode with the MWA full bandwidth.

Chapter 4

Multifrequency Study of Crab Giant Pulses with the MWA

4.1 Introduction

Single-pulse studies has proven to be excellent way of investigating the emission properties and the radiation mechanism of radio pulsars (e.g. Weatherall, 1997; Eilek et al., 2002; Hankins et al., 2003; Petrova, 2004). While the properties of the average profiles of most pulsars are often determined by geometrical factors (Manchester, 2009), the intrinsic properties of the single pulses are often obfuscated by propagation effects (Cordes et al., 2004). Analysis of data obtained at several frequencies simultaneously offers a possibility of distinguishing between propagation effects and the intrinsic properties of the radiation process (Popov et al., 2006; Karuppusamy et al., 2010), and also provides the opportunity of studying their spectral behaviour.

Although knowledge of the spectral behaviour of the Crab pulsar provides useful constraints on the emission mechanism (Malofeev and Malov, 1980), only the spectral behaviour of the average profile is well known (Maron et al., 2000; Kijak et al., 2007), but information about the dynamical processes is lost during averaging. Therefore studying the radio spectrum of the giant pulses via multi-frequency simultaneous observations provides an in-depth understanding of the dynamical process of their emission mechanism. Also, a better understanding of the spectral behaviour of the giant pulses can assist in putting constraints on theoretical models for the emitting particles.

In the previous chapter, a dual-frequency observations of the Crab pulsar with the MWA and the Parkes radio telescope was presented. We concentrated

on the broad band nature of Crab giant pulses, and determined the spectral indices of those detected simultaneously at the MWA and Parkes. In that work, some evidence for a spectral flattening at low frequencies was found. In this chapter, we present a multi-frequency observation of the Crab giant pulses with the MWA, and attempt to determine the spectral indices of the giant pulses detected simultaneously across the MWA frequency range.

4.2 Observation

We observed the Crab pulsar with the MWA on November 7, 2014, from UTC 17^h14^m00^s to UTC 18^h14^m38^s. The data were recorded with the MWA Voltage Capture System (Tremblay et al. 2015), from three frequency bands, centred at 120, 165, and 210 MHz. Each band consisted of 6×1.28 MHz coarse channels. The coarse channels were divided into 128 fine channels, resulting in a frequency and time resolution of 10 kHz and 100 μ s respectively. The voltages for the two linear polarisations were recorded for each frequency band. The observational parameters are summarised in Table 4.1.

Table 4.1: Observation parameters.

Parameters	Subbands		
	120 MHz	165 MHz	210 MHz
T_{sys} (K)	570	310	170
Centre frequency (MHz)	120.96	165.76	210.56
Bandwidth (MHz)	7.68	7.68	7.68
Number of giant pulses detected	2	18	13

The voltage samples in each 10-kHz channel for both polarisations were detected and summed incoherently. This incoherent summation resulted in a large field-of-view on the sky. The size of the beam depends strongly on the frequency of observation, and it is largest at the lowest observing frequency band. Although the beam is large on the sky, the sensitivity is a factor of \sqrt{N} less than the achievable sensitivity by the coherent addition of all the MWA antenna tiles, where N is the number of tiles. The incoherent summation was written out in the PSRFITS data format (Hotan et al., 2004).

4.3 Data Processing and Analysis

The data processing and analysis presented below closely follow those presented in detail in the previous chapter. We therefore only briefly describe the analysis, largely pointing out where the analysis differs significantly from that in Chapter 3.

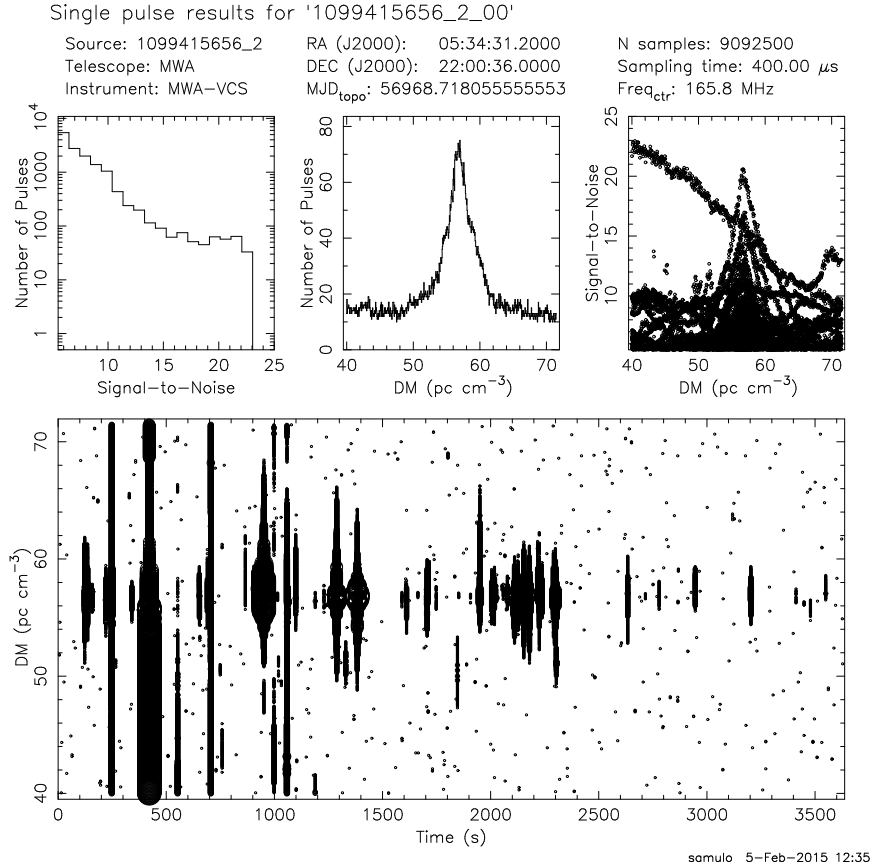


Figure 4.1: Single-pulse search result for 165 MHz band. The top left plot is a histogram of S/N of the detected pulses. The top middle plot is the number of pulses as a function of DM. The top right plot is a scatter plot of the S/N and DM. The bottom panel is a plot of DM as a function of time.

The PSRFITS files for the different bands were processed using a standard pulsar software package, PRESTO (Ransom, 2001). The data were averaged in time to 400 μ s and were then dedispersed across a range of trial DMs around the DM of the pulsar (56.7759 pc cm^{-3}) obtained from the Jodrell Bank monthly ephemeris¹ (Lyne et al., 1993). A single-pulse search was subsequently performed

¹<http://www.jb.man.ac.uk/pulsar/crab.html>

using the PRESTO software following the procedure described in Cordes and McLaughlin (2003).

Figure 4.1 is the single-pulse search result for one of our observed frequency bands. The detected giant pulses are seen clustered around the DM of the pulsar. Also visible in this plot is some broadband RFI. The top panels show the number of detected pulses as a function of DM, and the pulse signal-to-noise as a function of DM. Both plots show a strong peak at the DM of the pulsar.

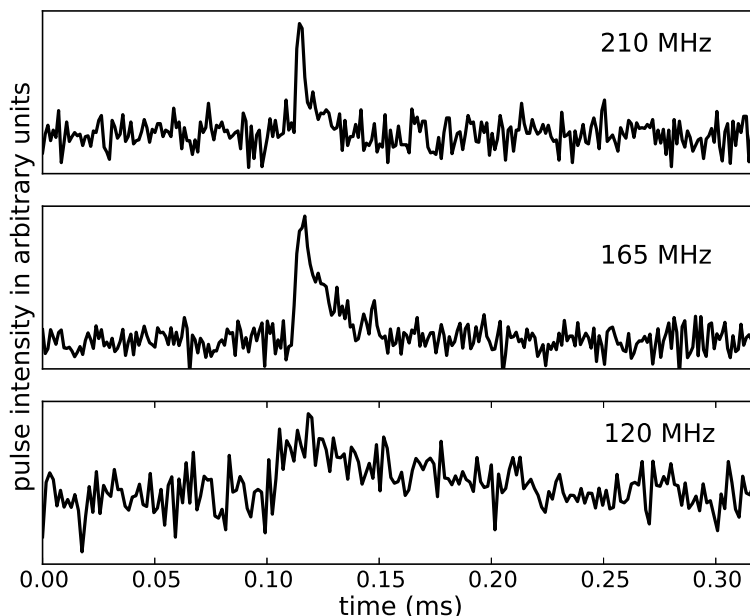


Figure 4.2: A plot showing a broad band giant pulse observed simultaneously in the three observed frequency bands, 210, 165, and 120 MHz from top to the bottom, after removing the baseline. The dispersive time delay between the bands has been removed.

The observed giant pulses at the MWA frequencies are often dominated by interstellar scattering (Ellingson et al., 2013; Oronsaye et al., 2015). As a result, the flux densities of the giant pulses are often under-estimated by the PRESTO software due to the presence of a long scattering tail (Figure 4.2). In order to accurately measure the energy of the giant pulses, the on-pulse regions in our timeseries were integrated. The calibration procedure described in Chapter 3 was employed here, with the following details changed: integration windows of 205, 72, and 28 ms were used at 120, 165, and 210 MHz, respectively; T_{sky} at 120, 165, and 210 MHz of 520, 260, and 120 K were used.

A search for simultaneous giant pulses was performed on the three observed frequency bands. As a result of the dispersive effect of the ISM, the high frequency giant pulses will arrive earlier than in the low frequency band. We estimated the time delay between 210 and 165 MHz, 210 and 120 MHz, and 165 and 120 MHz to be 3.067 s, 10.012 s, and 6.945 s, respectively. Of the thirteen giant pulses that were detected in the 210 MHz band, eight of them were also detected at 165 MHz band, while the two detected giant pulses in the 120 MHz band were also found in the 210 and 165 MHz bands. Thus, only two giant pulses were detected simultaneously across all bands. The spectral indices of the simultaneous detections were evaluated and are described in the following section.

4.4 Giant Pulse Spectral Indices

The spectral indices of the giant pulses detected simultaneously across the bands were evaluated after correcting for the primary beam at the various frequency bands.

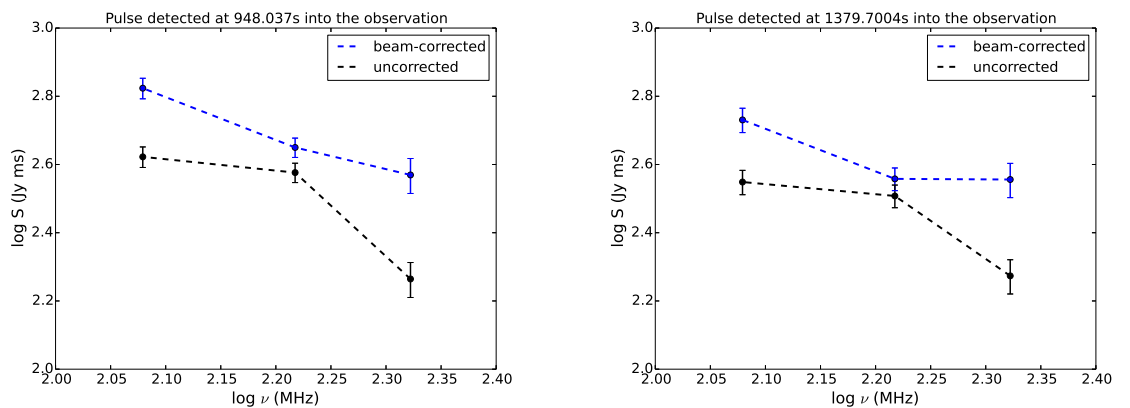


Figure 4.3: Plots of the spectra of the detected giant pulses at all three frequencies. The filled circles denote the pulses that were detected simultaneously in the three frequency bands, 120, 165, and 210 MHz. The blue colour indicates the beam-corrected fluence, while the black colour is the uncorrected fluence. The error bars reflect the relative measurement uncertainty in the fluence. **We acknowledge that the fluence at the lowest frequency band may be underestimated due to the increased scattering.**

The beam characteristics of a dipole array telescope is a function of the observing frequency and the pointing direction relative to the zenith. This dependency has

significant influence on the relative gain and therefore as well as the measured flux density of the observed pulses.

In order to account for this effect and accurately determine the flux density of each giant pulse in our data, we used the MWA beam model to correct for the primary beam at the various frequency bands, and subsequently evaluate the relative gains throughout the observing epoch. The relative gains were then used to estimate the flux density of the detected giant pulses at the various frequency bands.

Table 4.2: Spectral indices of the giant pulses detected across the bands.

Pulse toa (s)	Giant pulse spectral indices		
	210 & 165 MHz	210 & 120 MHz	165 & 120 MHz
948.0370	-0.78 ± 0.21	-1.06 ± 0.09	-1.27 ± 0.14
1379.7004	-0.02 ± 0.22	-0.73 ± 0.09	-1.26 ± 0.15
1702.5156	-0.15 ± 0.32	-----	-----
2014.3073	0.84 ± 0.30	-----	-----
2107.3197	1.09 ± 0.26	-----	-----
2149.8497	0.81 ± 0.28	-----	-----
2176.1997	1.34 ± 0.24	-----	-----
2296.5793	1.08 ± 0.24	-----	-----

The radio spectrum of the giant pulses observed simultaneously across the three bands are displayed in Figure 4.3. We performed a linear regression and obtained gradients of -1.09 ± 0.09 and -0.81 ± 0.10 . Figure 4.4 shows the spectrum of the giant pulses observed simultaneously in two frequency bands (165 and 210 MHz). Although the six pulses observed simultaneously at 165 and 210 MHz were not observed at 120 MHz, the upper limits of detection are indicated in the plots. The non-detection of these pulses at 120 MHz can be attributed to the effect of scattering and intrinsic spectral index.

The spectral index, α , describes the frequency dependence of flux measurements. The derived spectral indices are presented in Table 4.2, and show a range of -0.02 and $+1.34$ for the pulses detected in the 165 and 210 MHz bands. The table also shows a range of -1.06 and -0.73 for the two pulses detected simultaneously at 120 and 210 MHz bands, as well as -1.27 and -1.26 for those detected simultaneously at 120 and 165 MHz bands. **The values of the spectral in-**

dices derived here are considerably flatter than the values obtained by Oronsaye et al. (2015), based on their simultaneous detections at 193 and 1382 MHz. This can be interpreted as a sign of low frequency flattening or turnover.

We investigate this further by splitting each of the original band into smaller bands and determine the spectral indices across the bands. Each of the original frequency band (120, 165 and 210 MHz) was divided into two subbands with a bandwidth of 3.84 MHz at centre frequencies of 118.40, 122.24, 163.20, 167.04, 208.00, and 211.84 MHz respectively. A single pulse search was performed in each of the band following the procedure described previously. We found six simultaneous pulses at 163.20, 167.04, 208.00, and 211.84 MHz, non were detected at 118.40 and 122.24 MHz. The spectral indices across the band were subsequently determined. The derived values are presented in Table 4.3, and display a range between +1.14 and -1.96 . This result is indicative of spectral flattening and turnover at low frequencies, consistent with the values obtained previously.

Table 4.3: Spectral indices of the giant pulses detected across the bands.

Pulse toa (s)	Giant pulse spectral indices			
	211 & 163 MHz	211 & 167 MHz	211 & 208 MHz	167 & 163 MHz
948.03640	-0.82 ± 0.15	-1.50 ± 0.10	-0.75 ± 0.55	-0.27 ± 0.82
1379.7000	-0.94 ± 0.27	-1.15 ± 0.41	0.98 ± 0.32	-0.33 ± 0.68
2107.3196	-0.35 ± 0.24	-0.67 ± 0.33	-0.63 ± 0.40	1.14 ± 0.51
2149.8492	-1.96 ± 0.34	-1.38 ± 0.10	1.11 ± 0.61	-1.10 ± 0.65
2176.2004	-0.20 ± 0.22	-0.38 ± 0.30	0.54 ± 0.42	0.80 ± 0.41
2296.5788	-0.79 ± 0.28	-1.35 ± 0.28	-1.09 ± 0.32	0.38 ± 0.54

As noted by Bates et al. (2013), the observed spectral indices may be greatly influenced by the selection effects connected to the frequency-dependent sensitivity of pulsar observations. The spectral indices derived in this analysis are remarkably shallower than the values obtained previously by Sallmen et al. (1999) and Oronsaye et al. (2015). This dif-

ference may be partially attributed to the small fractional bandwidth used in this experiment compared to their large fractional bandwidth. Nevertheless, this result is consistent with the extrapolation of Ellingson et al. (2013), in which they indicated that the dependence of flux density on frequency may be considerably less than $\nu^{+2.7}$ at low frequencies.

4.5 Summary and Conclusion

In this chapter, a multi-frequency observation of the Crab pulsar with the MWA is presented. The observation was **first** performed with three frequency bands, centred at 120, 165 and 210 MHz; with a bandwidth of 7.68 MHz each. We detected eight giant pulses simultaneously at 165 and 210 MHz bands, of which two pulses were detected in all three frequency bands. A linear regression on the two pulses observed in all the frequency bands yield index values of -1.09 ± 0.09 and -0.81 ± 0.10 . **We also observed six simultaneous giant pulses across four frequency bands, centred at 163, 167, 208 and 211 MHz, each with a bandwidth of 3.84 MHz. The spectral index of the simultaneous giant pulses are in the range of $-1.96 \pm 0.34 > \alpha > +1.14 \pm 0.51$.**

Different range of spectral indices have been reported for the Crab giant pulses (see Sallmen et al., 1999; Popov et al., 2006; Karuppusamy et al., 2012; Oronsaye et al., 2015). A comparison of previous results with the results obtained in this analysis shows a remarkable variation in the range of spectral index of the giant pulses. These variations suggests that the shape of the giant pulse radio spectrum may not be fully described by a simple power-law.

The derived spectral indices are considerably flatter than the results obtained for simultaneous detections by Sallmen et al. (1999) and Karuppusamy et al. (2012). Spectral flattening and turnovers based on the average pulse profiles are frequently observed at low frequencies (<300 MHz; see Izvekova et al., 1981; Maron et al., 2000; Bilous et al., 2015). Although we cannot make direct comparison between the spectral of the average pulse profiles and that of the individual giant pulses, the result of this analysis underscore the difficulty of detecting giant pulses at low frequencies. Our findings are consistent with the result of Ellingson et al. (2013), in which they suggested that the dependence of

flux density on frequency is possibly less than $\nu^{+2.7}$, and appears to confirm the evidence found in Oronsaye et al. (2015) that the spectral index of Crab giant pulses flattens at low frequencies, compared to high frequencies.

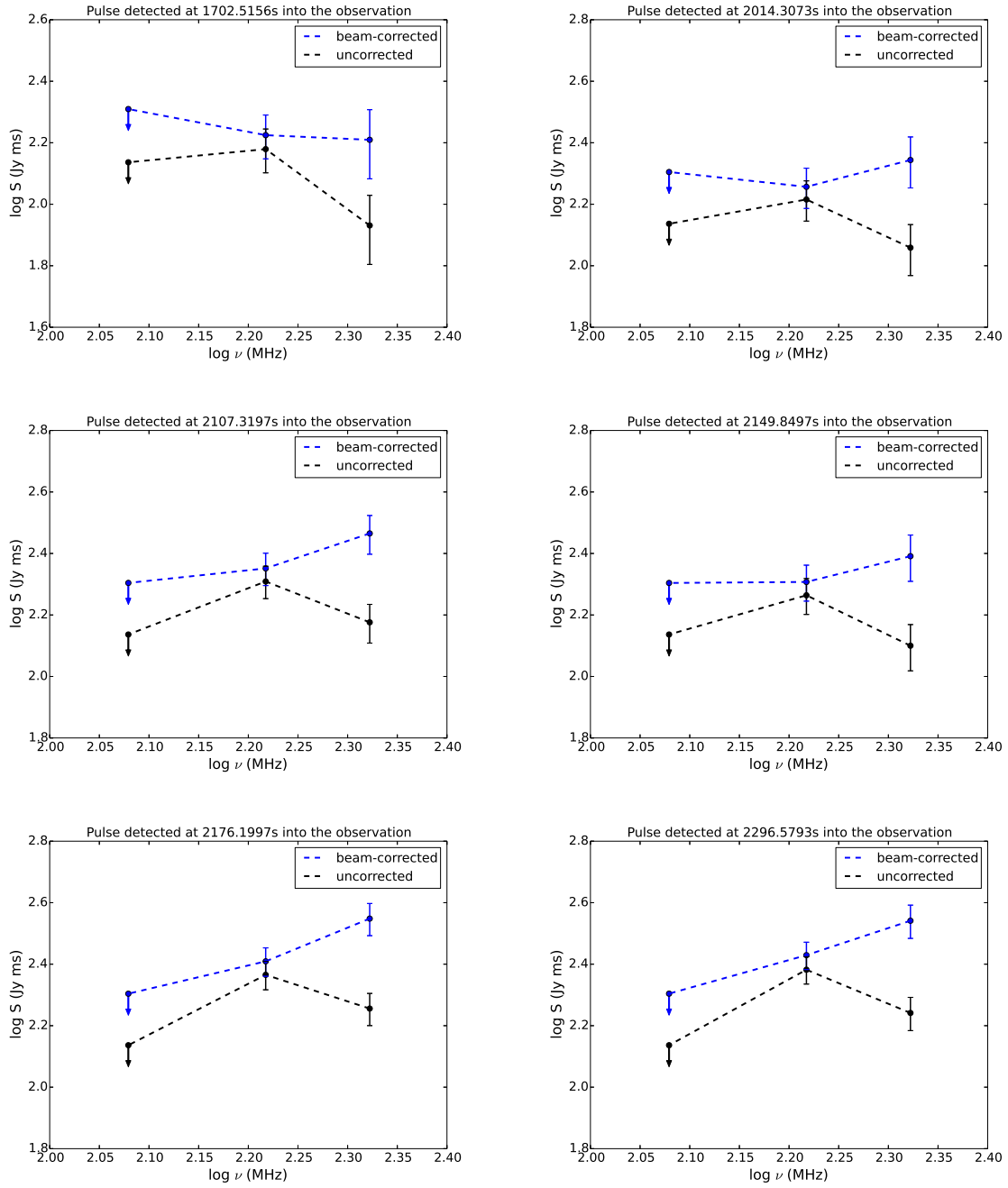


Figure 4.4: Plots of radio spectra of the detected giant pulses at 165 and 210 MHz. Also shown here is the upper limit (inverted arrow) at 120 MHz band where the pulses were not detected. The blue colour indicates the beam corrected fluences, while the black colour indicates the uncorrected fluences. The error bars reflect the relative measurement uncertainty in the fluences.

Chapter 5

Conclusions and Future Work

5.1 Conclusions

In this thesis, we have successfully observed Crab pulsar giant pulses with the MWA (a new radio telescope operating at low radio frequencies) and the Parkes radio telescope. The main focus of this thesis was to investigate the broadband nature of the Crab giant pulses and their spectral behaviour. The observations discussed in the previous chapters (chapters 3 and 4) revealed that the Crab giant pulses are intrinsically broadband and that their spectral indices are drawn from a normal distribution. Our investigation of the giant pulse spectral behaviour at low frequencies showed that their spectral indices are significantly shallower than at higher frequencies, and show evidence of frequency turnover in the radio spectrum at low frequencies.

In chapter 3, the Crab pulsar was observed with the MWA and Parkes radio telescope simultaneously. We detected 55 giant pulses at the MWA, and used the maximum likelihood estimator approach to estimate a power-law index of $\beta = -3.35 \pm 0.35$ for their fluence distribution. The same approach was used to determine a power-law index of $\beta = -2.85 \pm 0.05$ for the fluence distribution of the 2075 giant pulses detected at Parkes. The reported power-law index for the giant pulse fluence distribution covers a wide range, from -1.51 ± 0.05 to -2.39 ± 0.12 that was reported by Karuppusamy et al. (2012) at 110-180 MHz, up to -3.46 ± 0.04 that was reported by Lundgren et al. (1995) for their average flux density distribution observed at 800 MHz. This variation in the published power-law indices may be as a result of the underlying distribution not following a simple power law over a large range of fluences, coupled with the inconsistencies in the subjective determination of the power-law index. The maximum likeli-

hood estimator approach that we have employed in this thesis has the virtue of removing some subjectivity from power-law index analysis.

In probing the broad band nature of the giant pulses, a search for coincident pulses was performed on the giant pulses detected at the MWA and the Parkes radio telescope. Simultaneous observations at widely separated frequencies have been employed to investigate the broad band nature of the Crab giant pulses (e.g. Comella et al., 1969; Sallmen et al., 1999). The published simultaneous detections has varying degree of correlation, from as low as 3% to as high as 70% (Sallmen et al., 1999; Popov et al., 2006; Bhat et al., 2008; Mickaliger et al., 2012). In this thesis, we detected 51% of the MWA giant pulses at the Parkes radio telescope with spectral indices in the range of $-3.6 > \alpha > -4.9$. The spectral index range derived here is narrower than the result of Sallmen et al. (1999). We performed a Monte Carlo analysis to investigate the less than 100% correlation observed between the MWA and Parkes observations. The analysis supports the conjecture that the giant pulse emission in the Crab is intrinsically broadband, the less than 100% correlation being due to the relative sensitivities of the two instruments and the width of the spectral index distribution. Our results are therefore consistent with the hypothesis that the spectral index of giant pulses is drawn from normal distribution of standard deviation 0.6, but with a mean that displays an evolution with frequency from -3.00 at 1382 MHz, to -2.85 at 192 MHz.

In chapter 4, we investigated the spectral behaviour of the Crab giant pulses at low frequencies with the MWA. The Crab pulsar was observed simultaneously **at three frequency bands within the full bandwidth of the MWA, centred at 120, 165, and 210 MHz. Two of these bands (165 and 210 MHz) were further subdivided into two subbands each (163, 167, 208, and 211 MHz). Two giant pulses were detected simultaneously at 120, 165 and 210 MHz frequency bands, eight were detected simultaneously at 165 and 210 MHz bands (see Table 4.2), while six pulses were observed simultaneously at 163, 167, 208 and 211 MHz bands (see Table 4.3).** The estimated spectral indices of the simultaneous giant pulses are in the range of $-1.96 \pm 0.34 > \alpha > +1.34 \pm 0.24$. The observed spectral index values are considerably shallower than at higher frequencies, and show evidence of a turnover in giant pulse spectra at low frequencies. This result is in agreement with the extrapolation of Ellingson et al. (2013), in which they hypothesized that the dependence of flux density on frequency is significantly less than $\nu^{+2.7}$.

5.2 Future Work

This thesis provides an initial understanding of the broad band nature of the Crab giant pulses and their spectral behaviour at low frequencies. However, improvements can be made. Frequency turnovers in radio spectra are phenomenon in pulsar science. Some pulsars show a low-frequency turnover in their spectrum with the peak frequency occurring in the range of 100 to 400 MHz (Malofeev et al., 1994). Although this study is the first to report a spectra turnover in giant pulse spectra at low frequencies, the peak frequency is not determined. Future work should be targeted at performing more sensitive observations of the Crab pulsar with better frequency coverage in order to determine the peak frequencies and other characteristics of the giant pulse radio spectrum.

Bibliography

- Abdo, A. A., M. Ajello, A. Allafort, L. Baldini, J. Ballet, G. Barbiellini, M. G. Baring, D. Bastieri, A. Belfiore, R. Bellazzini, and et al. (2013, October). The Second Fermi Large Area Telescope Catalog of Gamma-Ray Pulsars. *ApJS* 208, 17.
- Allen, M. P. and J. E. Horvath (1997, May). Glitches, torque evolution and the dynamics of young pulsars. *MNRAS* 287, 615–621.
- Archibald, A. M., I. H. Stairs, S. M. Ransom, V. M. Kaspi, V. I. Kondratiev, D. R. Lorimer, M. A. McLaughlin, J. Boyles, J. W. T. Hessels, R. Lynch, J. van Leeuwen, M. S. E. Roberts, F. Jenet, D. J. Champion, R. Rosen, B. N. Barlow, B. H. Dunlap, and R. A. Remillard (2009, June). A Radio Pulsar/X-ray Binary Link. *Science* 324, 1411–.
- Argyle, E. and J. F. R. Gower (1972, July). The Pulse-Height Distribution for NP 0532. *ApJL* 175, L89.
- Asseo, E. (1996). Plasma Instabilities : Sources for Coherent Radio Emission. In S. Johnston, M. A. Walker, and M. Bailes (Eds.), *IAU Colloq. 160: Pulsars: Problems and Progress*, Volume 105 of *Astronomical Society of the Pacific Conference Series*, pp. 147.
- Asseo, E., G. Pelletier, and H. Sol (1990, December). A non-linear radio pulsar emission mechanism. *MNRAS* 247, 529–548.
- Atteia, J.-L., C. Barat, K. Hurley, M. Niel, G. Vedrenne, W. D. Evans, E. E. Fenimore, R. W. Klebesadel, J. G. Laros, T. Cline, U. Desai, B. Teegarden, I. V. Estulin, V. M. Zenchenko, A. V. Kusnetsov, and V. G. Kurt (1987, May). A second catalog of gamma-ray bursts - 1978-1980 localizations from the interplanetary network. *ApJS* 64, 305–317.

- Bates, S. D., D. R. Lorimer, and J. P. W. Verbiest (2013, May). The pulsar spectral index distribution. *MNRAS* 431, 1352–1358.
- Beskin, V. S. and A. V. Gurevich (1993, January). *Physics of the pulsar magnetosphere*. Cambridge University Press, Cambridge, UK.
- Bhat, N. D. R., J. M. Cordes, F. Camilo, D. J. Nice, and D. R. Lorimer (2004, April). Multifrequency Observations of Radio Pulse Broadening and Constraints on Interstellar Electron Density Microstructure. *ApJ* 605, 759–783.
- Bhat, N. D. R., J. M. Cordes, and S. Chatterjee (2003, February). A CLEAN-based Method for Deconvolving Interstellar Pulse Broadening from Radio Pulses. *ApJ* 584, 782–790.
- Bhat, N. D. R., S. M. Ord, S. E. Tremblay, S. J. Tingay, A. A. Deshpande, W. van Straten, S. Oronsaye, G. Bernardi, J. D. Bowman, F. Briggs, R. J. Cappallo, B. E. Corey, D. Emrich, R. Goetze, L. J. Greenhill, B. J. Hazelton, J. N. Hewitt, M. Johnston-Hollitt, D. L. Kaplan, J. C. Kasper, E. Kratzenberg, C. J. Lonsdale, M. J. Lynch, S. R. McWhirter, D. A. Mitchell, M. F. Morales, E. Morgan, D. Oberoi, T. Prabu, A. E. E. Rogers, D. A. Roshi, N. Udaya Shankar, K. S. Srivani, R. Subrahmanyam, M. Waterson, R. B. Wayth, R. L. Webster, A. R. Whitney, A. Williams, and C. L. Williams (2014, August). The Low-frequency Characteristics of PSR J0437-4715 Observed with the Murchison Wide-field Array. *ApJL* 791, L32.
- Bhat, N. D. R., S. J. Tingay, and H. S. Knight (2008, April). Bright Giant Pulses from the Crab Nebula Pulsar: Statistical Properties, Pulse Broadening, and Scattering Due to the Nebula. *ApJ* 676, 1200–1209.
- Bhat, N. D. R., R. B. Wayth, H. S. Knight, J. D. Bowman, D. Oberoi, D. G. Barnes, F. H. Briggs, R. J. Cappallo, D. Herne, J. Kocz, C. J. Lonsdale, M. J. Lynch, B. Stansby, J. Stevens, G. Torr, R. L. Webster, and J. S. B. Wyithe (2007, August). Detection of Crab Giant Pulses Using the Mileura Widefield Array Low Frequency Demonstrator Field Prototype System. *ApJ* 665, 618–627.
- Bietenholz, M. F., N. Kassim, D. A. Frail, R. A. Perley, W. C. Erickson, and A. R. Hajian (1997, November). The Radio Spectral Index of the Crab Nebula. *ApJ* 490, 291–301.

- Biggs, J. D., M. Bailes, A. G. Lyne, W. M. Goss, and A. S. Fruchter (1994, March). Two radio pulsars in the globular cluster NGC 6624. *MNRAS* *267*, 125.
- Bildsten, L., D. Chakrabarty, J. Chiu, M. H. Finger, D. T. Koh, R. W. Nelson, T. A. Prince, B. C. Rubin, D. M. Scott, M. Stollberg, B. A. Vaughan, C. A. Wilson, and R. B. Wilson (1997, December). Observations of Accreting Pulsars. *ApJS* *113*, 367–408.
- Bilous, A., V. Kondratiev, M. Kramer, E. Keane, J. Hessels, B. Stappers, V. Malofeev, C. Sobey, R. Breton, S. Cooper, H. Falcke, A. Karastergiou, D. Michilli, S. Osłowski, S. Sanidas, S. ter Veen, J. van Leeuwen, J. Verbiest, P. Weltevrede, P. Zarka, J.-M. Grießmeier, M. Serylak, M. Bell, J. Broderick, J. Eislöffel, S. Markoff, and A. Rowlinson (2015, November). A LOFAR census of non-recycled pulsars: average profiles, dispersion measures, flux densities, and spectra. *ArXiv e-prints*.
- Bilous, A. V., V. I. Kondratiev, M. A. McLaughlin, S. M. Ransom, M. Lyutikov, M. Mickaliger, and G. I. Langston (2011, February). Correlation of Fermi Photons with High-frequency Radio Giant Pulses from the Crab Pulsar. *ApJ* *728*, 110.
- Blandford, R. D. and R. W. Romani (1988, October). On the interpretation of pulsar braking indices. *MNRAS* *234*, 57P–60P.
- Bogdanov, S., A. M. Archibald, C. Bassa, A. T. Deller, J. P. Halpern, G. Heald, J. W. T. Hessels, G. H. Janssen, A. G. Lyne, J. Moldon, Z. Paragi, A. Patruno, B. B. P. Perera, B. W. Stappers, S. P. Tendulkar, C. R. D’Angelo, and R. Wijnands (2014, December). Coordinated X-ray, Ultraviolet, Optical, and Radio Observations of the PSR J1023+0038 System in a Low-mass X-ray Binary State. *ArXiv e-prints*.
- Bowman, J. D., I. Cairns, D. L. Kaplan, T. Murphy, D. Oberoi, L. Staveley-Smith, W. Arcus, D. G. Barnes, G. Bernardi, F. H. Briggs, S. Brown, J. D. Bunton, A. J. Burgasser, R. J. Cappallo, S. Chatterjee, B. E. Corey, A. Coster, A. Deshpande, L. deSouza, D. Emrich, P. Erickson, R. F. Goetze, B. M. Gaensler, L. J. Greenhill, L. Harvey-Smith, B. J. Hazelton, D. Herne, J. N. Hewitt, M. Johnston-Hollitt, J. C. Kasper, B. B. Kincaid, R. Koenig, E. Kratzenberg, C. J. Lonsdale, M. J. Lynch, L. D. Matthews, S. R. McWhirter, D. A. Mitchell,

- M. F. Morales, E. H. Morgan, S. M. Ord, J. Pathikulangara, T. Prabu, R. A. Remillard, T. Robishaw, A. E. E. Rogers, A. A. Roshi, J. E. Salah, R. J. Sault, N. U. Shankar, K. S. Srivani, J. B. Stevens, R. Subrahmanyam, S. J. Tingay, R. B. Wayth, M. Waterson, R. L. Webster, A. R. Whitney, A. J. Williams, C. L. Williams, and J. S. B. Wyithe (2013, April). Science with the Murchison Widefield Array. *PASA* 30, 31.
- Breton, R. P., M. H. van Kerkwijk, M. S. E. Roberts, J. W. T. Hessels, F. Camilo, M. A. McLaughlin, S. M. Ransom, P. S. Ray, and I. H. Stairs (2013, June). Discovery of the Optical Counterparts to Four Energetic Fermi Millisecond Pulsars. *ApJ* 769, 108.
- Bridle, A. H. (1970, March). Low-frequency Spectrum of the Crab Nebula. *Nature* 225, 1035–1037.
- Bruck, Y. M. and B. Y. Ustimenko (1977, September). The interpulse radio emission of the pulsar PSR 1919 + 21 at the frequencies 16.7–38 MHz. *Ap&SS* 51, 225–227.
- Burke, B. F. and F. Graham-Smith (2010, February). *An Introduction to Radio Astronomy*.
- Burke-Spolaor, S., M. Bailes, S. Johnston, S. D. Bates, N. D. R. Bhat, M. Burgay, N. D’Amico, A. Jameson, M. J. Keith, M. Kramer, L. Levin, S. Milia, A. Possenti, B. Stappers, and W. van Straten (2011, October). The High Time Resolution Universe Pulsar Survey - III. Single-pulse searches and preliminary analysis. *MNRAS* 416, 2465–2476.
- Burke-Spolaor, S., S. Johnston, M. Bailes, S. D. Bates, N. D. R. Bhat, M. Burgay, D. J. Champion, N. D’Amico, M. J. Keith, M. Kramer, L. Levin, S. Milia, A. Possenti, B. Stappers, and W. van Straten (2012, June). The High Time Resolution Universe Pulsar Survey - V. Single-pulse energetics and modulation properties of 315 pulsars. *MNRAS* 423, 1351–1367.
- Cairns, I. H., S. Johnston, and P. Das (2001, December). Intrinsic Variability of the Vela Pulsar: Lognormal Statistics and Theoretical Implications. *ApJL* 563, L65–L68.
- Camilo, F., S. M. Ransom, J. P. Halpern, J. Reynolds, D. J. Helfand, N. Zimmerman, and J. Sarkissian (2006, August). Transient pulsed radio emission from a magnetar. *Nature* 442, 892–895.

- Chen, W. C. and X. D. Li (2006, April). Why the braking indices of young pulsars are less than 3? *A&A* 450, L1–L4.
- Cheng, J. (Ed.) (2009). *The Principles of Astronomical Telescope Design*, Volume 360 of *Astrophysics and Space Science Library*.
- Coenen, T., J. van Leeuwen, J. W. T. Hessels, B. W. Stappers, V. I. Kondratiev, A. Alexov, R. P. Breton, A. Bilous, S. Cooper, H. Falcke, R. A. Fallows, V. Gajjar, J.-M. Grießmeier, T. E. Hassall, A. Karastergiou, E. F. Keane, M. Kramer, M. Kuniyoshi, A. Noutsos, S. Osłowski, M. Pilia, M. Serylak, C. Schrijvers, C. Sobey, S. ter Veen, J. Verbiest, P. Weltevrede, S. Wijnholds, K. Zagkouris, A. S. van Amesfoort, J. Anderson, A. Asgekar, I. M. Avruch, M. E. Bell, M. J. Bentum, G. Bernardi, P. Best, A. Bonafede, F. Breitling, J. Broderick, M. Brüggen, H. R. Butcher, B. Ciardi, A. Corstanje, A. Deller, S. Duscha, J. Eislöffel, R. Fender, C. Ferrari, W. Frieswijk, M. A. Garrett, F. de Gasperin, E. de Geus, A. W. Gunst, J. P. Hamaker, G. Heald, M. Hoeft, A. van der Horst, E. Jette, G. Kuper, C. Law, G. Mann, R. McFadden, D. McKay-Bukowski, J. P. McKean, H. Munk, E. Orru, H. Paas, M. Pandey-Pommier, A. G. Polatidis, W. Reich, A. Renting, H. Röttgering, A. Rowlinson, A. M. M. Scaife, D. Schwarz, J. Sluman, O. Smirnov, J. Swinbank, M. Tagger, Y. Tang, C. Tasse, S. Thoudam, C. Toribio, R. Vermeulen, C. Vocks, R. J. van Weeren, O. Wucknitz, P. Zarka, and A. Zensus (2014, October). The LOFAR pilot surveys for pulsars and fast radio transients. *A&A* 570, A60.
- Cognard, I., J. A. Shrauner, J. H. Taylor, and S. E. Thorsett (1996, February). Giant Radio Pulses from a Millisecond Pulsar. *ApJL* 457, L81.
- Comella, J. M., H. D. Craft, R. V. E. Lovelace, and J. M. Sutton (1969, February). Crab Nebula Pulsar NP 0532. *Nature* 221, 453–454.
- Cordes, J. M. (1992). Probing Magnetospheres of Rotation-Driven Neutron Stars. In T. H. Hankins, J. M. Rankin, and J. A. Gil (Eds.), *IAU Colloq. 128: Magnetospheric Structure and Emission Mechanics of Radio Pulsars*, pp. 253.
- Cordes, J. M., N. D. R. Bhat, T. H. Hankins, M. A. McLaughlin, and J. Kern (2004, September). The Brightest Pulses in the Universe: Multifrequency Observations of the Crab Pulsar’s Giant Pulses. *ApJ* 612, 375–388.
- Cordes, J. M., P. C. C. Freire, D. R. Lorimer, F. Camilo, D. J. Champion, D. J. Nice, R. Ramachandran, J. W. T. Hessels, W. Vlemmings, J. van Leeuwen,

- S. M. Ransom, N. D. R. Bhat, Z. Arzoumanian, M. A. McLaughlin, V. M. Kaspi, L. Kasian, J. S. Deneva, B. Reid, S. Chatterjee, J. L. Han, D. C. Backer, I. H. Stairs, A. A. Deshpande, and C.-A. Faucher-Giguère (2006, January). Arecibo Pulsar Survey Using ALFA. I. Survey Strategy and First Discoveries. *ApJ* 637, 446–455.
- Cordes, J. M. and D. J. Helfand (1980, July). Pulsar timing. III - Timing noise of 50 pulsars. *ApJ* 239, 640–650.
- Cordes, J. M. and T. J. W. Lazio (2002, July). NE2001.I. A New Model for the Galactic Distribution of Free Electrons and its Fluctuations. *ArXiv Astrophysics e-prints*.
- Cordes, J. M. and M. A. McLaughlin (2003, October). Searches for Fast Radio Transients. *ApJ* 596, 1142–1154.
- Davidson, K. and W. Tucker (1970, August). Radiative Ionization of the Filaments in the Crab Nebula. *ApJ* 161, 437.
- de Oliveira-Costa, A., M. Tegmark, B. M. Gaensler, J. Jonas, T. L. Landecker, and P. Reich (2008, July). A model of diffuse Galactic radio emission from 10 MHz to 100 GHz. *MNRAS* 388, 247–260.
- Demorest, P. B. (2011, October). Cyclic spectral analysis of radio pulsars. *MNRAS* 416, 2821–2826.
- Demorest, P. B., T. Pennucci, S. M. Ransom, M. S. E. Roberts, and J. W. T. Hessels (2010, October). A two-solar-mass neutron star measured using Shapiro delay. *Nature* 467, 1081–1083.
- Eilek, J. A., P. N. Arendt, Jr., T. H. Hankins, and J. C. Weatherall (2002). The Radio-Loud Plasma in Pulsars. In W. Becker, H. Lesch, and J. Trümper (Eds.), *Neutron Stars, Pulsars, and Supernova Remnants*, pp. 249.
- Ellingson, S. W., T. E. Clarke, J. Craig, B. C. Hicks, T. J. W. Lazio, G. B. Taylor, T. L. Wilson, and C. N. Wolfe (2013, May). Observations of Crab Giant Pulses in 20-84 MHz using LWA1. *ApJ* 768, 136.
- Ershov, A. A. and A. D. Kuzmin (2005, November). Detection of giant pulses in pulsar jASTROBJ_iPSR J1752+2359_i/ASTROBJ_i. *A&A* 443, 593–597.

- Espinoza, C. M., A. G. Lyne, M. Kramer, R. N. Manchester, and V. M. Kaspi (2011, November). The Braking Index of PSR J1734-3333 and the Magnetar Population. *ApJL* 741, L13.
- Espinoza, C. M., A. G. Lyne, B. W. Stappers, and M. Kramer (2011, June). A study of 315 glitches in the rotation of 102 pulsars. *MNRAS* 414, 1679–1704.
- Frank, J., A. King, and D. J. Raine (2002, January). *Accretion Power in Astrophysics: Third Edition*.
- Gabor, D. (1946). Theory of Communication. *Journal of the Institute of Electrical Engineers*, Part III 93, 429–457.
- Gavriil, F. P., V. M. Kaspi, and P. M. Woods (2002, September). Magnetar-like X-ray bursts from an anomalous X-ray pulsar. *Nature* 419, 142–144.
- Gayet, R. (1970, December). On the Average Gaunt Factor for Free-Free Emission. *A&A* 9, 312.
- Gedalin, M., E. Gruman, and D. B. Melrose (2002, December). Mechanism of pulsar radio emission. *MNRAS* 337, 422–430.
- Giacconi, R., H. Gursky, E. Kellogg, E. Schreier, and H. Tananbaum (1971, July). Discovery of Periodic X-Ray Pulsations in Centaurus X-3 from UHURU. *ApJL* 167, L67.
- Gold, T. (1968, May). Rotating Neutron Stars as the Origin of the Pulsating Radio Sources. *Nature* 218, 731–732.
- Goldreich, P. and W. H. Julian (1969, August). Pulsar Electrodynamics. *ApJ* 157, 869.
- Goldsmith, P. F. (2002, December). Radio Telescopes and Measurements at Radio Wavelengths. 278, 45–79.
- Goldstein, M. L., S. A. Morris, and G. G. Yen (2004, September). Problems with fitting to the power-law distribution. *European Physical Journal B* 41, 255–258.
- Haensel, P., A. Y. Potekhin, and D. Yakovlev (2007). *NEUTRON STARS: Equation of State and Structure*. Springer Science and Business Media, New York, USA.

- Hankins, T. H. (1996). Microstructure: A Review. In S. Johnston, M. A. Walker, and M. Bailes (Eds.), *IAU Colloq. 160: Pulsars: Problems and Progress*, Volume 105 of *Astronomical Society of the Pacific Conference Series*, pp. 197.
- Hankins, T. H. and J. A. Eilek (2007, November). Radio Emission Signatures in the Crab Pulsar. *ApJ* 670, 693–701.
- Hankins, T. H., J. S. Kern, J. C. Weatherall, and J. A. Eilek (2003, March). Nanosecond radio bursts from strong plasma turbulence in the Crab pulsar. *Nature* 422, 141–143.
- Hankins, T. H. and B. J. Rickett (1975). Pulsar signal processing. *Methods in Computational Physics* 14, 55–129.
- Harding, A. K., I. Contopoulos, and D. Kazanas (1999, November). Magnetar Spin-Down. *ApJL* 525, L125–L128.
- Harding, A. K. and D. Lai (2006, September). Physics of strongly magnetized neutron stars. *Reports on Progress in Physics* 69, 2631–2708.
- Hassall, T. E., B. W. Stappers, J. W. T. Hessels, M. Kramer, A. Alexov, K. Anderson, T. Coenen, A. Karastergiou, E. F. Keane, V. I. Kondratiev, K. Lazaridis, J. van Leeuwen, A. Noutsos, M. Serylak, C. Sobey, J. P. W. Verbiest, P. Weltevrede, K. Zagkouris, R. Fender, R. A. M. J. Wijers, L. Bähren, M. E. Bell, J. W. Broderick, S. Corbel, E. J. Daw, V. S. Dhillon, J. Eisloffel, H. Falcke, J.-M. Grießmeier, P. Jonker, C. Law, S. Markoff, J. C. A. Miller-Jones, R. Osten, E. Rol, A. M. M. Scaife, B. Scheers, P. Schellart, H. Spreeuw, J. Swinbank, S. ter Veen, M. W. Wise, R. Wijnands, O. Wucknitz, P. Zarka, A. Asgekar, M. R. Bell, M. J. Bentum, G. Bernardi, P. Best, A. Bonafede, A. J. Boonstra, M. Brentjens, W. N. Brouw, M. Brüggen, H. R. Butcher, B. Ciardi, M. A. Garrett, M. Gerbers, A. W. Gunst, M. P. van Haarlem, G. Heald, M. Hoeft, H. Holties, A. de Jong, L. V. E. Koopmans, M. Kuniyoshi, G. Kuper, G. M. Loose, P. Maat, J. Masters, J. P. McKean, H. Meulman, M. Mevius, H. Munk, J. E. Noordam, E. Orrú, H. Paas, M. Pandey-Pommier, V. N. Pandey, R. Pizzo, A. Polatidis, W. Reich, H. Röttgering, J. Sluman, M. Steinmetz, C. G. M. Sterks, M. Tagger, Y. Tang, C. Tasse, R. Vermeulen, R. J. van Weeren, S. J. Wijnholds, and S. Yatawatta (2012, July). Wide-band simultaneous observations of pulsars: disentangling dispersion measure and profile variations. *A&A* 543, A66.

Hermesen, W., J. W. T. Hessels, L. Kuiper, J. van Leeuwen, D. Mitra, J. de Plaa, J. M. Rankin, B. W. Stappers, G. A. E. Wright, R. Basu, A. Alexov, T. Coenen, J.-M. Grießmeier, T. E. Hassall, A. Karastergiou, E. Keane, V. I. Kondratiev, M. Kramer, M. Kuniyoshi, A. Noutsos, M. Serylak, M. Pilia, C. Sobey, P. Weltevrede, K. Zagkouris, A. Asgekar, I. M. Avruch, F. Batejat, M. E. Bell, M. R. Bell, M. J. Bentum, G. Bernardi, P. Best, L. Birzan, A. Bonafede, F. Breitling, J. Broderick, M. Brüggen, H. R. Butcher, B. Ciardi, S. Duscha, J. Eisloffel, H. Falcke, R. Fender, C. Ferrari, W. Frieswijk, M. A. Garrett, F. de Gasperin, E. de Geus, A. W. Gunst, G. Heald, M. Hoeft, A. Horneffer, M. Iacobelli, G. Kuper, P. Maat, G. Macario, S. Markoff, J. P. McKean, M. Mevius, J. C. A. Miller-Jones, R. Morganti, H. Munk, E. Orrú, H. Paas, M. Pandey-Pommier, V. N. Pandey, R. Pizzo, A. G. Polatidis, S. Rawlings, W. Reich, H. Röttgering, A. M. M. Scaife, A. Schoenmakers, A. Shulevski, J. Sluman, M. Steinmetz, M. Tagger, Y. Tang, C. Tasse, S. ter Veen, R. Vermeulen, R. H. van de Brink, R. J. van Weeren, R. A. M. J. Wijers, M. W. Wise, O. Wucknitz, S. Yatawatta, and P. Zarka (2013, January). Synchronous X-ray and Radio Mode Switches: A Rapid Global Transformation of the Pulsar Magnetosphere. *Science* *339*, 436–.

Hesse, K. H. and R. Wielebinski (1974, April). Pulse Intensity Histograms of Pulsars. *A&A* *31*, 409.

Hewish, A., S. J. Bell, J. D. H. Pilkington, P. F. Scott, and R. A. Collins (1968, February). Observation of a Rapidly Pulsating Radio Source. *Nature* *217*, 709–713.

Hobbs, G., A. G. Lyne, and M. Kramer (2010, February). An analysis of the timing irregularities for 366 pulsars. *MNRAS* *402*, 1027–1048.

Hobbs, G. B., R. T. Edwards, and R. N. Manchester (2006, June). TEMPO2, a new pulsar-timing package - I. An overview. *MNRAS* *369*, 655–672.

Hotan, A. W., W. van Straten, and R. N. Manchester (2004). PSRCHIVE and PSRFITS: An Open Approach to Radio Pulsar Data Storage and Analysis. *PASA* *21*, 302–309.

Hulse, R. A. and J. H. Taylor (1975, January). Discovery of a pulsar in a binary system. *ApJL* *195*, L51–L53.

- Isaacman, R. and J. M. Rankin (1977, May). The Crab Nebula pulsar - Variability of dispersion and scattering. *ApJ* 214, 214–232.
- Izvekova, V. A., A. D. Kuzmin, V. M. Malofeev, and I. P. Shitov (1981, August). Radio spectra of pulsars. I - Observations of flux densities at meter wavelengths and analysis of the spectra. *Ap&SS* 78, 45–72.
- Jackson, J. D. (1998). *Classical Electrodynamics*.
- Johnston, S. and R. W. Romani (2003, June). Giant Pulses from PSR B0540-69 in the Large Magellanic Cloud. *ApJL* 590, L95–L98.
- Karuppusamy, R., B. W. Stappers, and K. J. Lee (2012, February). Crab giant pulses at low frequencies. *A&A* 538, A7.
- Karuppusamy, R., B. W. Stappers, and W. van Straten (2010, June). Giant pulses from the Crab pulsar. A wide-band study. *A&A* 515, A36.
- Kaspi, V. M., R. N. Manchester, B. Siegman, S. Johnston, and A. G. Lyne (1994, February). On the spin-down of PSR B1509-58. *ApJL* 422, L83–L86.
- Keith, M. J., A. Jameson, W. van Straten, M. Bailes, S. Johnston, M. Kramer, A. Possenti, S. D. Bates, N. D. R. Bhat, M. Burgay, S. Burke-Spolaor, N. D’Amico, L. Levin, P. L. McMahon, S. Milia, and B. W. Stappers (2010, December). The High Time Resolution Universe Pulsar Survey - I. System configuration and initial discoveries. *MNRAS* 409, 619–627.
- Kijak, J., Y. Gupta, and K. Krzeszowski (2007, February). Turn-over in pulsar spectra around 1 GHz. *A&A* 462, 699–702.
- Knight, H. S., M. Bailes, R. N. Manchester, and S. M. Ord (2006, December). A Study of Giant Pulses from PSR J1824-2452A. *ApJ* 653, 580–586.
- Kostyuk, S. V., V. I. Kondratiev, A. D. Kuzmin, M. V. Popov, and V. A. Soglasnov (2003, June). Peculiarities of Giant Pulses from the Crab Pulsar at Frequencies of 594 and 2228 MHz. *Astronomy Letters* 29, 387–393.
- Kouveliotou, C. (2003, December). Magnetars - Observations. In *American Astronomical Society Meeting Abstracts*, Volume 35 of *Bulletin of the American Astronomical Society*, pp. 1322.

- Kramer, M., I. H. Stairs, R. N. Manchester, M. A. McLaughlin, A. G. Lyne, R. D. Ferdman, M. Burgay, D. R. Lorimer, A. Possenti, N. D’Amico, J. M. Sarkissian, G. B. Hobbs, J. E. Reynolds, P. C. C. Freire, and F. Camilo (2006, October). Tests of General Relativity from Timing the Double Pulsar. *Science* 314, 97–102.
- Kraus, J. D. (1966, October). *Radio astronomy. McGraw-Hill Education, Europe.*
- Kuz’min, A. D., B. Y. Losovskii, S. V. Logvinenko, and I. I. Litvinov (2008, November). Deviation of the arrival-time delay of pulses for the Crab pulsar from a quadratic frequency region. *Astronomy Reports* 52, 910–916.
- Lattimer, J. M. (2012, November). The Nuclear Equation of State and Neutron Star Masses. *Annual Review of Nuclear and Particle Science* 62, 485–515.
- Lattimer, J. M. and M. Prakash (2001, March). Neutron Star Structure and the Equation of State. *ApJ* 550, 426–442.
- Lattimer, J. M. and M. Prakash (2004, April). The Physics of Neutron Stars. *Science* 304, 536–542.
- Lonsdale, C. J., R. J. Cappallo, M. F. Morales, F. H. Briggs, L. Benkevitch, J. D. Bowman, J. D. Bunton, S. Burns, B. E. Corey, L. Desouza, S. S. Doeleman, M. Derome, A. Deshpande, M. R. Gopala, L. J. Greenhill, D. E. Herne, J. N. Hewitt, P. A. Kamini, J. C. Kasper, B. B. Kincaid, J. Kocz, E. Kowald, E. Kratzenberg, D. Kumar, M. J. Lynch, S. Madhavi, M. Matejek, D. A. Mitchell, E. Morgan, D. Oberoi, S. Ord, J. Pathikulangara, T. Prabu, A. Rogers, A. Roshi, J. E. Salah, R. J. Sault, N. U. Shankar, K. S. Srivani, J. Stevens, S. Tingay, A. Vaccarella, M. Waterson, R. B. Wayth, R. L. Webster, A. R. Whitney, A. Williams, and C. Williams (2009, August). The Murchison Widefield Array: Design Overview. *IEEE Proceedings* 97, 1497–1506.
- Lorimer, D. R. and M. Kramer (2004, November). *Handbook of pulsar astronomy. Cambridge University Press, Cambridge, UK.*
- Lundgren, S. C. (1994). *A multi-wavelength study of rotation-driven pulsars.* Ph. D. thesis, Cornell Univ., Ithaca, NY.
- Lundgren, S. C., J. M. Cordes, M. Ulmer, S. M. Matz, S. Lomatch, R. S. Foster, and T. Hankins (1995, November). Giant Pulses from the Crab Pulsar: A Joint Radio and Gamma-Ray Study. *ApJ* 453, 433.

- Luo, Q. and D. B. Melrose (2001, July). Cyclotron absorption of radio emission within pulsar magnetospheres. *MNRAS* *325*, 187–196.
- Lyne, A., F. Graham-Smith, P. Weltevrede, C. Jordan, B. Stappers, C. Bassa, and M. Kramer (2013, November). Evolution of the Magnetic Field Structure of the Crab Pulsar. *Science* *342*, 598–601.
- Lyne, A., G. Hobbs, M. Kramer, I. Stairs, and B. Stappers (2010, July). Switched Magnetospheric Regulation of Pulsar Spin-Down. *Science* *329*, 408–.
- Lyne, A. G. (1987, April). A massive glitch in an old pulsar. *Nature* *326*, 569–571.
- Lyne, A. G. and F. Graham-Smith (1998). *Pulsar astronomy*.
- Lyne, A. G. and F. Graham-Smith (2005, July). *Pulsar Astronomy*.
- Lyne, A. G., C. A. Jordan, F. Graham-Smith, C. M. Espinoza, B. W. Stappers, and P. Weltevrede (2015, January). 45 years of rotation of the Crab pulsar. *MNRAS* *446*, 857–864.
- Lyne, A. G., R. S. Pritchard, and F. Graham-Smith (1993, December). Twenty-Three Years of Crab Pulsar Rotational History. *MNRAS* *265*, 1003.
- Lyne, A. G. and B. J. Rickett (1968, April). Measurements of the Pulse Shape and Spectra of the Pulsating Radio Sources. *Nature* *218*, 326–330.
- Malofeev, V. M., J. A. Gil, A. Jessner, I. F. Malov, J. H. Seiradakis, W. Sieber, and R. Wielebinski (1994, May). Spectra of 45 pulsars. *A&A* *285*, 201–208.
- Malofeev, V. M. and I. F. Malov (1980, February). Average pulsar spectra and their interpretation. *24*, 54.
- Manchester, R. N. (2009). Radio Emission Properties of Pulsars. In W. Becker (Ed.), *Astrophysics and Space Science Library*, Volume 357 of *Astrophysics and Space Science Library*, pp. 19.
- Manchester, R. N., G. Hobbs, M. Bailes, W. A. Coles, W. van Straten, M. J. Keith, R. M. Shannon, N. D. R. Bhat, A. Brown, S. G. Burke-Spolaor, D. J. Champion, A. Chaudhary, R. T. Edwards, G. Hampson, A. W. Hotan, A. Jameson, F. A. Jenet, M. J. Kesteven, J. Khoo, J. Kocz, K. Maciesiak, S. Osłowski, V. Ravi, J. R. Reynolds, J. M. Sarkissian, J. P. W. Verbiest, Z. L. Wen, W. E. Wilson, D. Yardley, W. M. Yan, and X. P. You (2013, January). The Parkes Pulsar Timing Array Project. *PASA* *30*, 17.

- Manchester, R. N., G. B. Hobbs, A. Teoh, and M. Hobbs (2005, April). The Australia Telescope National Facility Pulsar Catalogue. *AJ* 129, 1993–2006.
- Manchester, R. N., A. G. Lyne, F. Camilo, J. F. Bell, V. M. Kaspi, N. D’Amico, N. P. F. McKay, F. Crawford, I. H. Stairs, A. Possenti, M. Kramer, and D. C. Sheppard (2001, November). The Parkes multi-beam pulsar survey - I. Observing and data analysis systems, discovery and timing of 100 pulsars. *MNRAS* 328, 17–35.
- Manchester, R. N., E. Tademaru, and F. G. Smith (1971, December). Crab pulsar radiation mechanism. *Nature* 234, 164–165.
- Maron, O., J. Kijak, M. Kramer, and R. Wielebinski (2000, December). Pulsar spectra of radio emission. *A&AS* 147, 195–203.
- Mazets, E. P. and S. V. Golenetskii (1981). Cosmic gamma-ray bursts. *Astrophysics and Space Physics Reviews* 1, 205–266.
- Melrose, D. B. (1996). Whence the pulses? In S. Johnston, M. A. Walker, and M. Bailes (Eds.), *IAU Colloq. 160: Pulsars: Problems and Progress*, Volume 105 of *Astronomical Society of the Pacific Conference Series*, pp. 139.
- Melrose, D. B. and M. E. Gedalin (1999, August). Relativistic Plasma Emission and Pulsar Radio Emission: A Critique. *ApJ* 521, 351–361.
- Menou, K., R. Perna, and L. Hernquist (2001, October). Stability and Evolution of Supernova Fallback Disks. *ApJ* 559, 1032–1046.
- Mickaliger, M. B., M. A. McLaughlin, D. R. Lorimer, G. I. Langston, A. V. Bilous, V. I. Kondratiev, M. Lyutikov, S. M. Ransom, and N. Palliyaguru (2012, November). A Giant Sample of Giant Pulses from the Crab Pulsar. *ApJ* 760, 64.
- Moffett, D. A. and T. H. Hankins (1996, September). Multifrequency Radio Observations of the Crab Pulsar. *ApJ* 468, 779.
- Morris, D., M. Kramer, C. Thum, R. Wielebinski, M. Grewing, J. Penalver, A. Jessner, G. Butin, and W. Brunswig (1997, June). Pulsar detection at 87GHz. *A&A* 322, L17–L20.
- Newton, W. G. (2013, July). Neutron stars: A taste of pasta? *Nature Physics* 9, 396–397.

Ord, S. M., B. Crosse, D. Emrich, D. Pallot, R. B. Wayth, M. A. Clark, S. E. Tremblay, W. Arcus, D. Barnes, M. Bell, G. Bernardi, N. D. R. Bhat, J. D. Bowman, F. Briggs, J. D. Bunton, R. J. Cappallo, B. E. Corey, A. A. Deshpande, L. deSouza, A. Ewell-Wice, L. Feng, R. Goeke, L. J. Greenhill, B. J. Hazelton, D. Herne, J. N. Hewitt, L. Hindson, N. Hurley-Walker, D. Jacobs, M. Johnston-Hollitt, D. L. Kaplan, J. C. Kasper, B. B. Kincaid, R. Koenig, E. Kratzenberg, N. Kudryavtseva, E. Lenc, C. J. Lonsdale, M. J. Lynch, B. McKinley, S. R. McWhirter, D. A. Mitchell, M. F. Morales, E. Morgan, D. Oberoi, A. Offringa, J. Pathikulangara, B. Pindor, T. Prabu, P. Procopio, R. A. Remillard, J. Riding, A. E. E. Rogers, A. Roshi, J. E. Salah, R. J. Sault, N. Udaya Shankar, K. S. Srivani, J. Stevens, R. Subrahmanyan, S. J. Tingay, M. Waterson, R. L. Webster, A. R. Whitney, A. Williams, C. L. Williams, and J. S. B. Wyithe (2015, March). The Murchison Widefield Array Correlator. *PASA* 32, 6.

Oronsaye, S. I., S. M. Ord, N. D. R. Bhat, S. E. Tremblay, S. J. McSweeney, S. J. Tingay, W. van Straten, A. Jameson, G. Bernardi, J. D. Bowman, F. Briggs, R. J. Cappallo, A. A. Deshpande, L. J. Greenhill, B. J. Hazelton, M. Johnston-Hollitt, D. L. Kaplan, C. J. Lonsdale, S. R. McWhirter, D. A. Mitchell, M. F. Morales, E. Morgan, D. Oberoi, T. Prabu, N. Udaya Shankar, K. S. Srivani, R. Subrahmanyan, R. B. Wayth, R. L. Webster, A. Williams, and C. L. Williams (2015, August). Simultaneous Observations of Giant Pulses from the Crab Pulsar, with the Murchison Widefield Array and Parkes Radio Telescope: Implications for the Giant Pulse Emission Mechanism. *ApJ* 809, 51.

Pacini, F. (1968, July). Rotating Neutron Stars, Pulsars and Supernova Remnants. *Nature* 219, 145–146.

Papitto, A., C. Ferrigno, E. Bozzo, N. Rea, L. Pavan, L. Burderi, M. Burgay, S. Campana, T. di Salvo, M. Falanga, M. D. Filipović, P. C. C. Freire, J. W. T. Hessels, A. Possenti, S. M. Ransom, A. Riggio, P. Romano, J. M. Sarkissian, I. H. Stairs, L. Stella, D. F. Torres, M. H. Wieringa, and G. F. Wong (2013, September). Swings between rotation and accretion power in a binary millisecond pulsar. *Nature* 501, 517–520.

Petrova, S. A. (2004, September). On the origin of giant pulses in radio pulsars. *A&A* 424, 227–236.

- Pines, D. and M. A. Alpar (1985, July). Superfluidity in neutron stars. *Nature* 316, 27–32.
- Pober, J., A. Parsons, D. Backer, R. Bradley, C. Parashare, N. Gugliucci, E. Benoit, J. Aguirre, D. Jacobs, D. Moore, C. Carilli, J. Manley, and C. van der Meere (2011, January). The Precision Array for Probing the Epoch of Reionization. In *American Astronomical Society Meeting Abstracts #217*, Volume 43 of *Bulletin of the American Astronomical Society*, pp. 432.06.
- Popov, M. V., N. Bartel, W. H. Cannon, A. Y. Novikov, V. I. Kondratiev, and V. I. Altunin (2002, December). Pulsar microstructure and its quasi-periodicities with the S2 VLBI system at a resolution of 62.5 nanoseconds. *A&A* 396, 171–187.
- Popov, M. V., A. D. Kuz'min, O. M. Ul'yanov, A. A. Deshpande, A. A. Ershov, V. V. Zakharenko, V. I. Kondrat'ev, S. V. Kostyuk, B. Y. Losovskiä, and V. A. Soglasnov (2006, July). Instantaneous radio spectra of giant pulses from the crab pulsar from decimeter to decameter wavelengths. *Astronomy Reports* 50, 562–568.
- Popov, M. V. and B. Stappers (2007, August). Statistical properties of giant pulses from the Crab pulsar. *A&A* 470, 1003–1007.
- Potekhin, A. Y. (2010, December). The physics of neutron stars. *Physics Uspekhi* 53, 1235–1256.
- Prabu, T., K. S. Srivani, D. A. Roshi, P. A. Kamini, S. Madhavi, D. Emrich, B. Crosse, A. J. Williams, M. Waterson, A. A. Deshpande, N. U. Shankar, R. Subrahmanyam, F. H. Briggs, R. F. Goeke, S. J. Tingay, M. Johnston-Hollitt, G. M. R. E. H. Morgan, J. Pathikulangara, J. D. Bunton, G. Hampson, C. Williams, S. M. Ord, R. B. Wayth, D. Kumar, M. F. Morales, L. deSouza, E. Kratzenberg, D. Pallot, R. McWhirter, B. J. Hazelton, W. Arcus, D. G. Barnes, G. Bernardi, T. Boller, J. D. Bowman, R. J. Cappallo, B. E. Corey, L. J. Greenhill, D. Herne, J. N. Hewitt, D. L. Kaplan, J. C. Kasper, B. B. Kincaid, R. Koenig, C. J. Lonsdale, M. J. Lynch, D. A. Mitchell, D. Oberoi, R. A. Remillard, A. E. Rogers, J. E. Salah, R. J. Sault, J. B. Stevens, S. Tremblay, R. L. Webster, A. R. Whitney, and S. B. Wyithe (2015, March). A digital-receiver for the MurchisonWidefield Array. *Experimental Astronomy* 39, 73–93.

- Rankin, J. M. and C. C. Counselman, III (1973, May). Pulsar NP 0532: Variability of Dispersion and Scattering. *ApJ* 181, 875–890.
- Ransom, S. M. (2001). *New search techniques for binary pulsars*. Ph. D. thesis, Harvard University.
- Rickett, B. J. (1990). Radio propagation through the turbulent interstellar plasma. *ARA&A* 28, 561–605.
- Ritchings, R. T. (1976, August). Pulsar single pulse intensity measurements and pulse nulling. *MNRAS* 176, 249–263.
- Romani, R. W. and S. Johnston (2001, August). Giant Pulses from the Millisecond Pulsar B1821-24. *ApJL* 557, L93–L96.
- Rybicki, G. B. and A. P. Lightman (1979, January). Book-Review - Radiative Processes in Astrophysics. *Astronomy Quarterly* 3, 199.
- Sallmen, S., D. C. Backer, T. H. Hankins, D. Moffett, and S. Lundgren (1999, May). Simultaneous Dual-Frequency Observations of Giant Pulses from the Crab Pulsar. *ApJ* 517, 460–471.
- Smith, K. W. and P. W. Terry (2011, April). Damping of Electron Density Structures and Implications for Interstellar Scintillation. *ApJ* 730, 133.
- Soglasnov, V. A., M. V. Popov, N. Bartel, W. Cannon, A. Y. Novikov, V. I. Kondratiev, and V. I. Altunin (2004, November). Giant Pulses from PSR B1937+21 with Widths =15 Nanoseconds and $T_b=5\times 10^{39}$ K, the Highest Brightness Temperature Observed in the Universe. *ApJ* 616, 439–451.
- Staelin, D. H. and E. C. Reifstein, III (1968, December). Pulsating Radio Sources near the Crab Nebula. *Science* 162, 1481–1483.
- Stairs, I. H. (2004, April). Pulsars in Binary Systems: Probing Binary Stellar Evolution and General Relativity. *Science* 304, 547–552.
- Stappers, B. W., J. W. T. Hessels, A. Alexov, K. Anderson, T. Coenen, T. Hassall, A. Karastergiou, V. I. Kondratiev, M. Kramer, J. van Leeuwen, J. D. Mol, A. Noutsos, J. W. Romein, P. Weltevrede, R. Fender, R. A. M. J. Wijers, L. Bähren, M. E. Bell, J. Broderick, E. J. Daw, V. S. Dhillon, J. Eislöffel, H. Falcke, J. Griessmeier, C. Law, S. Markoff, J. C. A. Miller-Jones, B. Scheers, H. Spreuw, J. Swinbank, S. Ter Veen, M. W. Wise, O. Wucknitz, P. Zarka,

- J. Anderson, A. Asgekar, I. M. Avruch, R. Beck, P. Bennema, M. J. Bentum, P. Best, J. Bregman, M. Brentjens, R. H. van de Brink, P. C. Broekema, W. N. Brouw, M. Brüggen, A. G. de Bruyn, H. R. Butcher, B. Ciardi, J. Conway, R.-J. Dettmar, A. van Duin, J. van Enst, M. Garrett, M. Gerbers, T. Grit, A. Gunst, M. P. van Haarlem, J. P. Hamaker, G. Heald, M. Hoeft, H. Holties, A. Horneffer, L. V. E. Koopmans, G. Kuper, M. Loose, P. Maat, D. McKay-Bukowski, J. P. McKean, G. Miley, R. Morganti, R. Nijboer, J. E. Noordam, M. Norden, H. Olofsson, M. Pandey-Pommier, A. Polatidis, W. Reich, H. Röttgering, A. Schoenmakers, J. Sluman, O. Smirnov, M. Steinmetz, C. G. M. Sterks, M. Tagger, Y. Tang, R. Vermeulen, N. Vermaas, C. Vogt, M. de Vos, S. J. Wijnholds, S. Yatawatta, and A. Zensus (2011, June). Observing pulsars and fast transients with LOFAR. *A&A* 530, A80.
- Staveley-Smith, L., W. E. Wilson, T. S. Bird, M. J. Disney, R. D. Ekers, K. C. Freeman, R. F. Haynes, M. W. Sinclair, R. A. Vaile, R. L. Webster, and A. E. Wright (1996, November). The Parkes 21 CM multibeam receiver. *PASA* 13, 243–248.
- Tananbaum, H., H. Gursky, E. M. Kellogg, R. Levinson, E. Schreier, and R. Giacconi (1972, June). Discovery of a Periodic Pulsating Binary X-Ray Source in Hercules from UHURU. *ApJL* 174, L143.
- Taylor, G. B., S. W. Ellingson, N. E. Kassim, J. Craig, J. Dowell, C. N. Wolfe, J. Hartman, G. Bernardi, T. Clarke, A. Cohen, N. P. Dalal, W. C. Erickson, B. Hicks, L. J. Greenhill, B. Jacoby, W. Lane, J. Lazio, D. Mitchell, R. Navarro, S. M. Ord, Y. Pihlström, E. Polisensky, P. S. Ray, L. J. Rickard, F. K. Schinzel, H. Schmitt, E. Sigman, M. Soriano, K. P. Stewart, K. Stovall, S. Tremblay, D. Wang, K. W. Weiler, S. White, and D. L. Wood (2012, December). First Light for the First Station of the Long Wavelength Array. *Journal of Astronomical Instrumentation* 1, 50004.
- Thompson, A. R., J. M. Moran, and G. W. Swenson (2007). *Interferometry and Synthesis in Radio Astronomy*, John Wiley Sons, 2007.
- Thompson, D. J. (2008, November). Gamma ray astrophysics: the EGRET results. *Reports on Progress in Physics* 71(11), 116901.
- Thorsett, S. E. and D. Chakrabarty (1999, February). Neutron Star Mass Measurements. I. Radio Pulsars. *ApJ* 512, 288–299.

Tingay, S. J., R. Goeke, J. D. Bowman, D. Emrich, S. M. Ord, D. A. Mitchell, M. F. Morales, T. Booler, B. Crosse, R. B. Wayth, C. J. Lonsdale, S. Tremblay, D. Pallot, T. Colegate, A. Wicenc, N. Kudryavtseva, W. Arcus, D. Barnes, G. Bernardi, F. Briggs, S. Burns, J. D. Bunton, R. J. Cappallo, B. E. Corey, A. Deshpande, L. Desouza, B. M. Gaensler, L. J. Greenhill, P. J. Hall, B. J. Hazelton, D. Herne, J. N. Hewitt, M. Johnston-Hollitt, D. L. Kaplan, J. C. Kasper, B. B. Kincaid, R. Koenig, E. Kratzenberg, M. J. Lynch, B. Mckinley, S. R. McWhirter, E. Morgan, D. Oberoi, J. Pathikulangara, T. Prabu, R. A. Remillard, A. E. E. Rogers, A. Rosh, J. E. Salah, R. J. Sault, N. Udaya-Shankar, F. Schlagenhauer, K. S. Srivani, J. Stevens, R. Subrahmanyam, M. Waterson, R. L. Webster, A. R. Whitney, A. Williams, C. L. Williams, and J. S. B. Wyithe (2013, January). The Murchison Widefield Array: The Square Kilometre Array Precursor at Low Radio Frequencies. *PASA* 30, 7.

Tremblay, S. E., S. M. Ord, N. D. R. Bhat, S. J. Tingay, B. Crosse, D. Pallot, S. I. Oronsaye, G. Bernardi, J. D. Bowman, F. Briggs, R. J. Cappallo, B. E. Corey, A. A. Deshpande, D. Emrich, R. Goeke, L. J. Greenhill, B. J. Hazelton, M. Johnston-Hollitt, D. L. Kaplan, J. C. Kasper, E. Kratzenberg, C. J. Lonsdale, M. J. Lynch, S. R. McWhirter, D. A. Mitchell, M. F. Morales, E. Morgan, D. Oberoi, T. Prabu, A. E. E. Rogers, A. Rosh, N. Udaya Shankar, K. S. Srivani, R. Subrahmanyam, M. Waterson, R. B. Wayth, R. L. Webster, A. R. Whitney, A. Williams, and C. L. Williams (2015, February). The High Time and Frequency Resolution Capabilities of the Murchison Widefield Array. *PASA* 32, 5.

van Haarlem, M. P., M. W. Wise, and A. W. G. et al. (2013, August). LOFAR: The LOw-Frequency ARray. *A&A* 556, A2.

van Leeuwen, J. and B. W. Stappers (2010, January). Finding pulsars with LOFAR. *A&A* 509, A7.

Weatherall, J. C. (1997, July). Modulational Instability, Mode Conversion, and Radio Emission in the Magnetized Pair Plasma of Pulsars. *ApJ* 483, 402–413.

Weatherall, J. C. (1998, October). Pulsar Radio Emission by Conversion of Plasma Wave Turbulence: Nanosecond Time Structure. *ApJ* 506, 341–346.

Wijnands, R. (1999). *Millisecond phenomena in X-ray binaries*. Ph. D. thesis, , Univ. Amsterdam, (1999). Advisor: M. van der Klis.

- Wilson, T. L., K. Rohlfs, and S. Hüttemeister (2009). *Tools of Radio Astronomy*. Springer-Verlag.
- Wolszczan, A., J. Cordes, and D. Stinebring (1984). a Single Pulse Study of the Millisecond Pulsar 1937+214 (Poster). In S. P. Reynolds and D. R. Stinebring (Eds.), *Birth and Evolution of Neutron Stars: Issues Raised by Millisecond Pulsars*, pp. 63.
- Wolszczan, A. and D. A. Frail (1992, January). A planetary system around the millisecond pulsar PSR1257 + 12. *Nature* 355, 145–147.
- Wolszczan, A., S. R. Kulkarni, J. Middleditch, D. C. Backer, A. S. Fruchter, and R. J. Dewey (1989, February). A 110-ms pulsar, with negative period derivative, in the globular cluster M15. *Nature* 337, 531–533.
- Woods, P. M., V. M. Kaspi, C. Thompson, F. P. Gavriil, H. L. Marshall, D. Chakrabarty, K. Flanagan, J. Heyl, and L. Hernquist (2004, July). Changes in the X-ray Emission from the Magnetar Candidate 1E 2259+586 during its 2002 Outburst. In P. Kaaret, F. K. Lamb, and J. H. Swank (Eds.), *X-ray Timing 2003: Rossi and Beyond*, Volume 714 of *American Institute of Physics Conference Series*, pp. 298–301.
- Woods, P. M. and C. Thompson (2006, April). *Soft gamma repeaters and anomalous X-ray pulsars: magnetar candidates*, pp. 547–586.

Every reasonable effort has been made to acknowledge the owners of copyright material. I would be pleased to hear from any copyright owner who has been omitted or incorrectly acknowledged.

Publications

Publications directly resulting from the work done in this thesis:

- **S. I. Oronsaye**, S. M. Ord, N. D. R. Bhat, S. E. Tremblay, S. J. McSweeney, S. J. Tingay, W. van Straten, A. Jameson, G. Bernardi, J. D. Bowman, F. Briggs, R. J. Cappallo, A. A. Deshpande, L. J. Greenhill, B. J. Hazelton, M. Johnston-Hollitt, D. L. Kaplan, C. J. Lonsdale, S. R. McWhirter, D. A. Mitchell, M. F. Morales, E. Morgan, D. Oberoi, T. Prabu, N. Udaya Shankar, K. S. Sri-vani, R. Subrahmanyam, R. B. Wayth, R. L. Webster, A. Williams, and C. L. Williams (2015, August). Simultaneous Observations of Giant Pulses from the Crab Pulsar, with the Murchison Widefield Array and Parkes Radio Telescope: Implications for the Giant Pulse Emission Mechanism. *ApJ* 809, 51.
- S. E. Tremblay, S. M. Ord, N. D. R. Bhat, S. J. Tingay, B. Crosse, D. Palot, **S. I. Oronsaye**, G. Bernardi, J. D. Bowman, F. Briggs, R. J. Cappallo, B. E. Corey, A. A. Deshpande, D. Emrich, R. Goeke, L. J. Greenhill, B. J. Hazelton, M. Johnston-Hollitt, D. L. Kaplan, J. C. Kasper, E. Kratzenberg, C. J. Lonsdale, M. J. Lynch, S. R. McWhirter, D. A. Mitchell, M. F. Morales, E. Morgan, D. Oberoi, T. Prabu, A. E. E. Rogers, A. Roshi, N. Udaya Shankar, K. S. Srivani, R. Subrahmanyam, M. Waterson, R. B. Wayth, R. L. Webster, A. R. Whitney, A. Williams, and C. L. Williams (2015, February). The High Time and Frequency Resolution Capabilities of the Murchison Widefield Array. *PASA* 32, 5.
- N. D. R. Bhat, S. M. Ord, S. E. Tremblay, S. J. Tingay, A. A. Deshpande, W. van Straten, **S. Oronsaye**, G. Bernardi, J. D. Bowman, F. Briggs, R. J. Cappallo, B. E. Corey, D. Emrich, R. Goeke, L. J. Greenhill, B. J.

Hazelton, J. N. Hewitt, M. Johnston-Hollitt, D. L. Kaplan, J. C. Kasper, E. Kratzenberg, C. J. Lonsdale, M. J. Lynch, S. R. McWhirter, D. A. Mitchell, M. F. Morales, E. Morgan, D. Oberoi, T. Prabu, A. E. E. Rogers, D. A. Roshi, N. Udaya Shankar, K. S. Srivani, R. Subrahmanyam, M. Waterson, R. B. Wayth, R. L. Webster, A. R. Whitney, A. Williams, and C. L. Williams (2014, August). The Low-frequency Characteristics of PSR J0437-4715 Observed with the Murchison Wide-field Array. *ApJL* 791, L32.